UNIVERSITY OF CALIFORNIA, SAN DIEGO

Indirect excitons in GaAs coupled quantum wells: Development of optoelectronic logic devices and trapping potentials, and studies of low temperature phenomena in a bosonic condensed matter system

A dissertation submitted in partial satisfaction of the
requirements for the degree
Doctor of Philosophy

in

Phyics

by

Alexander Arthur High

Committee in charge:

Professor Leonid Butov, Chair
Professor Sadik Esener
Professor Michael Fogler
Professor Brian Maple
Professor Shayan Mookherjea

2012

The dissertation of Alexander Arthur High is approved, and it is acceptable in quality and form for publication on microfilm and electronically:

_____

_____

_____

_____

_____
Chair

University of California, San Diego

2012

DEDICATION

To my wife, Rachel, and to my loving and supportive family.

TABLE OF CONTENTS

LIST OF FIGURES

ACKNOWLEDGEMENTS

First and foremost, I would like to thank my advisor, Professor Leonid Butov. Leonid has guided me with a steady hand through seven years of fascinating and difficult research. From the first day I joined his group I could always count on having an interesting project to work on. Leonid has instilled in me many important values relating to life in science: to be scientifically rigorous, to always look forward with a positive outlook, and to simply allow facts to speak for themselves. Leonid is an admirable scientist and I am grateful to have learned from him.

Over the years, I have been fortunate to work with many talented and interesting people. In particular, I would like to thank my co-worker Aaron Hammack, who initiated me into the laboratory environment and taught me many of the experimental techniques utilized in my research. Aaron also had the pleasure of receiving untold numbers of 2:00am phone calls from a panicked graduate student (myself) who was convinced that he had broken a cryostat, CCD, dilution fridge, vacuum pump, TiSaph, Lock-In, or PMT.

I would also like to thank my long-time lab mates Jason Leonard, Yuliya Kuznetsova, Sen Yang, Alex Winbow, and Mikas Remeika. Working with them has not only been productive but also has been a great joy. Jason has been helpful to me in all aspects of my research, from setting up polarization resolved measurements to teaching me the basics of matlab. Yuliya has done an exceptional job pushing exciton device research forward. Alex has always had a keen eye for the intricacies of engineering and was always available to discuss experimental details in-depth. Sen built a body of exceptional research on the macroscopically ordered exciton state which laid the groundwork for much of my work as well as more work to come. Furthermore, he left behind a fully functional interferometer. Mikas has done beautiful work in the clean room, and has helped craft many of the nanoscale devices presented in this dissertation. I would also like to thank Averi Thomas, Gabriele Grosso, and Ekaterina Novitskaya for assisting me in my experiments.

I would like to thank Misha Fogler, Alexei Ivanov, Alexey Kavokin,

Leonidas Mouchliadis, Tomas Ostatnicky and Andrew Meyertholen for their rigorous and interesting theoretical work. Their contributions have consistently aided us in understanding our complex and sometimes mysterious experimental results.

I would like to thank Arthur Gossard, Micah Hanson, and Kenneth Campman for their fabrication of high quality GaAs quantum wells. Their samples have been the backbone of my research.

I consider graduate school as seven years well spent, in large part due to the people with whom I have spent my time here. I would like to thank my friends for making my life more interesting and worthwhile. I would like to specifically thank my seven-year roommate, Matt LeBourgeois, for never saying no to a glass of scotch or a round of golf, and for being someone I can count on in a pinch.

I would like to thank my entire family for supporting and inspiring me. I am fortunate to descend from a long line of curious and bright people, and a love and respect for science has been part of my upbringing from day one. In particular, I would like to thank my parents Steve and Viki. Mom has always challenged me to strive for my fullest potential. Dad inspired a love of physics in me from an early age, and continues to foster my curiosity to this day.

Finally, I would like to thank Rachel for sticking by my side all my years in graduate school. She has brightened my days, and I am excited to see what our future holds.

The text of chapter 2, in part, is a reprint of the material as it appears in A.A. High, A.T. Hammack, L.V. Butov, M, Hanson & A.C. Gossard, *Exciton optoelectronic transistor*, Optics Letters 32, 2466 (2007), ©Optical Society of America, where the dissertation author was the first author. The co-authors in this publication directed, supervised, and co-worked on the research which forms the basis of this chapter.

The text of chapter 2, in part, is a reprint of the material as it appears in A.A. High, E.E. Novitskaya, L.V. Butov, M. Hanson & A.C. Gossard, *Control of*

exciton fluxes in an excitonic integrated circuit, Science 321, 229 (2008); published online 19 June 2008, ©American Academy for the Advancement of Science, where the dissertation author was the first author. The co-authors in this publication directed, supervised, and co-worked on the research which forms the basis of this chapter.

The text of chapter 3, in part, is a reprint of the material as it appears in A.A. High, A.T. Hammack, L.V. Butov, L. Mouchliadis, A.L. Ivanov, M. Hanson & A.C. Gossard, *Indirect excitons in elevated traps*, Nano Letters 9, 2094 (2009), ©American Chemical Society, where the dissertation author was the first author. The co-authors in this publication directed, supervised, and co-worked on the research which forms the basis of this chapter.

The text of chapter 3, in part, is a reprint of the material as it appears in A.A. High, A.K. Thomas, G. Grosso, M. Remeika, A.T. Hammack, A.D. Meyertholen, M.M. Fogler, L.V. Butov, M. Hanson & A.C. Gossard, *Trapping indirect excitons in a GaAs quantum-well structure with a diamond-shaped electrostatic trap*, Physical Review Letters 103, 087403 (2009), ©American Physical Society, where the dissertation author was the first author. The co-authors in this publication directed, supervised, and co-worked on the research which forms the basis of this chapter.

The text of chapter 4, in part, is a reprint of the material as it appears in A.A. High, J.R. Leonard, A.T. Hammack, M.M. Fogler, L.V. Butov, A.V. Kavokin, K.L. Campman & A.C. Gossard, *Spontaneous coherence in a cold exciton gas*, Nature 483, 584 (2012), ©Nature Publishing Group, where the dissertation author was the first author. The co-authors in this publication directed, supervised, and co-worked on the research which forms the basis of this chapter.

The text of chapter 4, in part, is a reprint of the material as it appears in A.A. High, A.T. Hammack, J.R. Leonard, Sen Yang, L.V. Butov, T. Ostatnicky, A.V. Kavokin & A.C. Gossard, *Spin texture in a cold exciton gas*, arXiv:1103.0321, where the dissertation author was the first author. The co-authors in this publication directed, supervised, and co-worked on the research which forms the basis of this chapter.

The text of chapter 5, in part, is a reprint of the material as it appears in A.A. High, J.R. Leonard, M. Remeika, L.V. Butov, M. Hanson & A.C. Gossard, *Condensation of excitons in a trap*, Nano Letters 12, 2605 (2012), ©American Chemical Society, where the dissertation author was the first author. The co-authors in this publication directed, supervised, and co-worked on the research which forms the basis of this chapter.

The text of appendix C, in part, is a reprint of the material as it appears in A.A. High, J.R. Leonard, A.T. Hammack, M.M. Fogler, L.V. Butov, A.V. Kavokin, K.L. Campman & A.C. Gossard, *Spontaneous coherence in a cold exciton gas*, Nature 483, 584 (2012), ©Nature Publishing Group, where the dissertation author was the first author. The co-authors in this publication directed, supervised, and co-worked on the research which forms the basis of this appendix.

The text of appendix D, in part, is a reprint of the material as it appears in A.A. High, A.T. Hammack, J.R. Leonard, Sen Yang, L.V. Butov, T. Ostatnicky, A.V. Kavokin & A.C. Gossard, *Spin texture in a cold exciton gas*, arXiv:1103.0321, where the dissertation author was the first author. The co-authors in this publication directed, supervised, and co-worked on the research which forms the basis of this appendix.

VITA

2004	B. S. in Physics University of Pennsylvania
2005-2012	Graduate Research Assistant Advisor: Professor Leonid V. Butov University of California, San Diego
2012	Ph. D. in Physics University of California, San Diego

PUBLICATIONS

A.A. High, A.T. Hammack, L.V. Butov, M. Hanson & A.C. Gossard, *Exciton optoelectronic transistor*, Optics Letters 32, 2466 (2007)

A.A. High, E.E. Novitskaya, L.V. Butov, M. Hanson & A.C. Gossard, *Control of exciton fluxes in an excitonic integrated circuit*, Science 321, 229 (2008); published online 19 June 2008

A.A. High, A.T. Hammack, L.V. Butov, L. Mouchliadis, A.L. Ivanov, M. Hanson & A.C. Gossard, *Indirect excitons in elevated traps*, Nano Letters 9, 2094 (2009)

A.A. High, A.K. Thomas, G. Grosso, M. Remeika, A.T. Hammack, A.D. Meyertholen, M.M. Fogler, L.V. Butov, M. Hanson & A.C. Gossard, *Trapping indirect excitons in a GaAs quantum-well structure with a diamond-shaped electrostatic trap*, Physical Review Letters 103, 087403 (2009)

G. Grosso, J.C. Graves, A.T. Hammack, A.A. High, L.V. Butov, M. Hanson & A.C. Gossard, *Excitonic switches operating at around 100K*, Nature Photonics 3, 577 (2009)

Y.Y. Kuznetsova, M. Remeika, A.A. High, A.T. Hammack, L.V. Butov, M. Hanson & A.C. Gossard, *All-optical excitonic transistor*, Optics Letters 35, 1587 (2010)

Y.Y Kuznetsova, A.A. High & L.V. Butov, *Control of excitons by laterally modulated electrode density*, Applied Physics Letters 97, 201106 (2010)

A. G. Winbow, J. R. Leonard, M. Remeika, Y. Y. Kuznetsova, A. A. High, A. T. Hammack, L. V. Butov, J. Wilkes, A. A. Guenther, A. L. Ivanov, M. Hanson, & A. C. Gossard, *Electrostatic conveyer for excitons*, Physical Review Letters 106, 196806 (2011)

A.A. High, A.T. Hammack, J.R. Leonard, Sen Yang, L.V. Butov, T. Ostatnicky, A.V. Kavokin & A.C. Gossard, *Spin texture in a cold exciton gas*, arXiv:1103.0321

A.A. High, J.R. Leonard, A.T. Hammack, M.M. Fogler, L.V. Butov, A.V. Kavokin, K.L. Campman & A.C. Gossard, *Spontaneous coherence in a cold exciton gas*, Nature 483, 584 (2012)

A.A. High, J.R. Leonard, M. Remeika, L.V. Butov, M. Hanson & A.C. Gossard, *Condensation of excitons in a trap*, Nano Letters 12, 2605 (2012)

J.R. Leonard, M. Remeika, Y.Y. Kuznetsova, A.A. High, L.V. Butov, J. Wilkes, M. Hanson, A.C. Gossard, *Transport of indirect excitons in a potential energy gradient*, Applied Physics Letters 100, 231106 (2012)

ABSTRACT OF THE DISSERTATION

Indirect excitons in GaAs coupled quantum wells: Development of optoelectronic logic devices and trapping potentials, and studies of low temperature phenomena in a bosonic condensed matter system

by

Alexander Arthur High

Doctor of Philosophy in Phyics

University of California, San Diego, 2012

Professor Leonid Butov, Chair

Indirect excitons in coupled quantum wells form a unique system for both development of novel optoelectronic devices as well as studies of the low temperature physics of bosons in condensed matter systems. An exciton is a quasiparticle which is a bound state of an electron and hole. Excitons can be created by light, and when they recombine they can emit light. In an indirect exciton, the electron and hole are spatially separated, which results in a long exciton lifetime as well as an electronic dipole moment. The long lifetime allows excitons to travel over large distances $\sim 100\mu$m. The electronic dipole moment allows direct electronic control of the exciton energy. Therefore, as an optical

media that is also electronically controllable, indirect excitons offer promise for development of new, efficient optoelectronic devices. In this dissertation, we prototype two new optoelectronic devices based on indirect excitons: the exciton optoelectronic transistor, and the excitonic integrated circuit. In addition, the long radiative lifetime allows indirect excitons to cool to very low temperatures below the temperature of quantum degeneracy. Traps are of particular interest for studies of low temperature gases, as they facilitate creation of high density, cold gases as well as offer opportunities for *in situ* control of the gas. This dissertation presents novel, precisely engineered trapping potentials for exciton gases based on electronic control and makes a thorough examination of the physical properties of the trapped gas. Furthermore, as a bosonic quasiparticle, excitons can be expected to form a condensate under certain density and temperature conditions. A signature of condensation is the emergence of spontaneous extended coherence, where the coherence length significantly exceeds its classically expected value. We present the first evidence for extended spatial coherence in an exciton system - the system of exciton rings. A pattern of extended spontaneous coherence is correlated with a pattern of spontaneous polarization, revealing the properties of a multicomponent coherent state. We also observed phase singularities in the coherent exciton gas. Lastly, we probe the spatial coherence of excitons in an electrostatic trap and present direct evidence for Bose-Einstein condensation of excitons therein.

Chapter 1

Introduction

An exciton is a quasiparticle composed of an electron and hole. Excitons can be created by light, and when they decay they can release light. In an indirect exciton system, the electrons and holes are spatially separated. Similar to electrons, indirect excitons can be controlled electronically. Therefore, as an optically active, electronically controllable particle they are attractive media for the development of optoelectronic devices. Furthermore, since an exciton is composed of two fermions, it is a boson. The low temperature behavior of fermions in crystals have been explored for more than a century; the study of excitons provides an opportunity to study the comparatively unexplored physics of ultra cold bosons in condensed matter materials. Bosons can be expected to form condensates under certain experimental conditions, and a main thrust of exciton research is to directly measure condensation.

This chapter will introduce the indirect exciton system, as well as discuss the properties of GaAs that make it a favorable material for studies of indirect excitons. We will describe the most significant characteristics of indirect excitons, and discuss condensation in a two-dimensional exciton system. Furthermore, we will provide a description of experimental methods for researching indirect excitons, and provide a historical background on prior achievements in the field. Finally, we will provide a brief outline of the dissertation.

1.1 Indirect excitons in GaAs

The presence of a crystal and hence a lattice potential has dramatic consequences on the behavior of electrons. For a free, non-relativistic electron, the relationship between the energy ϵ and wavenumber k of the electron - the band diagram - is simply a quadratic curve $\epsilon = (\hbar k)^2/(2m_e)$. In a crystal, electrons interact with a periodic lattice potential. In general, the presence of a lattice potential leads to allowed regions of electron energy in which multiple energy-momentum bands can exist as well as forbidden regions of electron energy known as band gaps. See appendix A for an introductory-level discussion of band structure.

In a semiconductor, in the limit $T \to 0$, the Fermi energy resides within the band gap, meaning the bands are either completely occupied (valence bands) or completely empty (conduction bands). Under certain circumstances, an electron in the valence band can absorb a photon and be promoted to the conduction band. It will leave behind a vacancy in the valence band - a hole - which carries positive charge. Then, the electron and hole will be attracted to each other and can form a hydrogen-like bound state called an exciton.

GaAs has many properties which make it advantageous for studies of excitons. GaAs has a band gap that is direct in momentum space; this means that excitonic absorption and emission will be an efficient process. Furthermore, the exciton emission is at wavelengths in the near infrared, $\approx$ 790nm, which is convenient for optical studies with standard lasers, lenses, and CCDs. In comparison, studies at $\approx$ 400nm, the wavelength of the band gap in ZnO, requires specialized equipment such as ultraviolet lasers. Furthermore, GaAs heterostructures have a long history of development, and they can be grown with extremely high quality. The heterostructures studied in this dissertation have very low concentrations of impurities; this reduces undesirable effects such as non-radiative recombination and leakage currents. Furthermore, GaAs quantum wells can be grown with very small well-width fluctuations, with energy broadening due to disorder of $<$ 1meV. See appendix B for a more thorough description of the optical properties of GaAs.

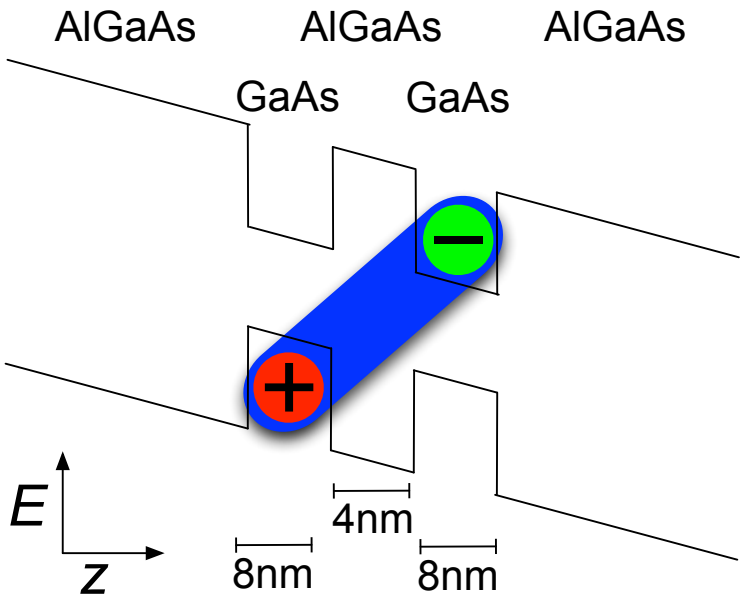

Figure 1.1: An electric field along the z-axis pulls the electron and hole into spatially separated quantum wells, forming an indirect exciton.

With epitaxial techniques, it is possible to combine materials with different band structures to form *heterostructures*. This thesis mainly concerns GaAs/AlGaAs coupled quantum well heterostructures, in which two 8nm layers of GaAs separated by 4nm are embedded in $Al_{0.33}Ga_{0.67}As$, see Fig. 1.1. In this band structure, it is energetically favorable for the electrons and holes to reside in the quantum wells, and within the quantum wells their behavior becomes effectively two-dimensional. If an electric field is applied along the z-direction, due to their opposite charge the electrons and holes will be pulled into different quantum wells, and form spatially *indirect* excitons, see Fig. 1.1.

1.1.1 Properties of indirect excitons

The spatial separation of the electron and hole leads to numerous differences between indirect excitons in quantum wells and bulk direct excitons in GaAs. Indirect excitons (1) have a dramatically increased lifetime compared to direct excitons, (2) have a higher cooling rate than direct excitons, (3) have a repulsive dipole interaction which can screen disorder, and (4) they are elec-

tronically controllable, whereas direct excitons are only weakly modified by electric fields. These features are discussed below and will be expanded upon in later chapters. There are further differences between indirect excitons and bulk direct excitons; for instance, the electron-hole exchange interaction is reduced, which can increase spin coherence lifetime [Leonard *et al.*, 2009], and the dipole-repulsive nature of indirect excitons prevents exciton molecule formation, which can be a source of instability for Bose-Einstein condensation of excitons [Keldysh & Kozlov, 1968].

(1) Long lifetime:

Due to the spatial separation between the electron and hole layers, the lifetime of an indirect exciton exceeds by orders of magnitude the lifetime of regular excitons and varies typically from ten nanoseconds to ten microseconds. This is the main advantage of utilizing indirect excitons as opposed to direct excitons. As a result, indirect excitons can travel over large distances of tens and hundreds of micrometers within their lifetime.

(2) Increased cooling rate:

Indirect excitons exist in a two-dimensional heterostructure. The emission of bulk longitudinal acoustic (LA) phonons is more efficient in quantum wells versus bulk. This is due to the relaxation of momentum conservation along the z-axis. This can increase the cooling rate by two to three orders of magnitude compared to bulk GaAs [Butov *et al.*, 2001]. The long lifetime combined with increased cooling rate allows excitons to readily cool to temperatures close to the bath temperature, permitting studies of low-temperature, equilibrium gases of indirect excitons.

(3) Screening of disorder:

Even in the highest quality GaAs samples, the quantum well disorder due to well-width fluctuation is on the order of 1meV. For the temperature range explored in this dissertation, $T < 10$K, the thermal energy is lower than the

disorder and localization effects could become dominant. This is undesirable, as we are interested in exploring systems where excitons can travel over large distances and exhibit two-dimensional behavior. To realize this system, the effects of disorder must be minimized. Indirect excitons, as aligned dipoles, are repulsive to eachother. Hence, if there is a minima in the disorder potential, a small number of excitons can in effect fill in the minima. Any further excitons added to the system will no longer see a potential minima; rather, they will see a smooth potential. This screening of disorder allows indirect excitons to propagate over large distances.

(4) Electronic control:

If an exciton is placed in an external electric field, the electron and hole will be pulled in opposite directions and it will acquire a electronic dipole moment. As a result, its energy will decrease. This is known as the Stark effect, and the same process can also be seen in atomic spectra under applied electric field. In bulk semiconductors, the maximum energy shift is limited to by ionization of the exciton, in which the electron and hole are pulled apart by the electric field. In these systems, the energy shift is limited to $\approx$ 10% of the exciton binding energy, discussed in [Miller *et al.*, 1985], which limits the usefulness of the effect. In quantum wells, where barriers strongly confine the exciton along the z-axis, a significantly larger z-axis electric field is required to pull the electron or hole out of the quantum well and hence ionize the exciton. This built in resistance to ionization allows for significantly larger exciton energy shifts. This effect known as the quantum-confined Stark effect [Miller *et al.*, 1985].

The electric field dependence of the exciton energy is dependent on the quantum well geometry, which along with the electric field determines the electronic dipole moment of the exciton. For a single quantum well geometry, the electron-hole separation - the dipole moment - is variable and depends on the electric field strength. In this dissertation we utilize a coupled quantum well geometry in which the exciton dipole moment is essentially fixed as the separation between the quantum well centers. Since the dipole moment is fixed,

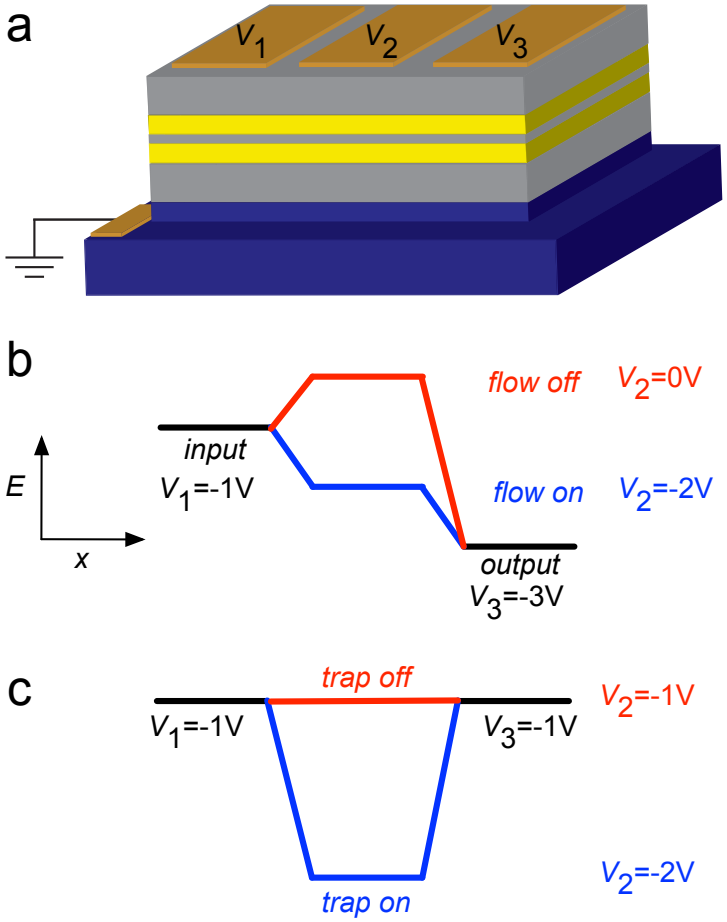

Figure 1.2: Schematic of electronic control of indirect excitons. (a) Model of CQW structure: $Al_{0.33}Ga_{0.67}As$ (grey), GaAs quantum well (yellow), n^+-doped GaAs (blue). Electrodes are deposited at the surface of the heterostructure (gold). (b) Electrode voltages V_1, V_2, V_3 configured in transistor operation. Excitons are created at the input; flux of excitons to output is controlled by V_2. (c) Electrodes configured as a trapping potential. When $|V_2| > |V_1, V_3|$, a trapping potential is created.

the exciton energy is linearly dependent on the strength of the applied electric field. Correct patterning of electrodes at the surface of the heterostructure allows creation of almost any desired potential landscape for indirect excitons, see Fig. 1.2.

1.1.2 Bose-Einstein condensation and superfluidity of indirect excitons

Particles that are indistinguishable and can allow degenerate occupation of the same state (i.e. bosons) obey Bose-Einstein statistics. Then, the number of particles N in a state with given energy ϵ is given by

$$N(\epsilon) = \frac{g(\epsilon)}{e^{(\epsilon-\mu)/k_BT} - 1} \tag{1.1}$$

where μ is the chemical potential and $g(\epsilon)$ is the density of states (for a full derivation see for instance [Pathria, 1996]). Depending on $g(\epsilon)$, for a given temperature T, there can be a maximum occupation of the excited states given by

$$N_{exc} = N_{total} - N_{ground} = \int_{\epsilon(n=1)}^{\infty} \frac{g(\epsilon)}{e^{\epsilon/k_BT} - 1} d\epsilon, \tag{1.2}$$

where $\epsilon(n = 1)$ is the energy of the first excited state. If this number is exceed, every further particle added to the system must reside in the ground state. Macroscopic occupation of the ground state, with N_{ground} on the order of N_{total}, is known as Bose-Einstein condensation.

The density of states plays a crucial role in determining the transition density (or alternatively transition temperature). For an infinite three dimensional system, $g(\epsilon) \propto \epsilon^{1/2}$ and N_{exc} gives a finite number. However, for an infinite two dimensional system, $g(\epsilon)$ is constant and hence the integral diverges and there is no limit on the number of particles in the excited states. Therefore, in an infinite two-dimensional system Bose-Einstein condensation cannot occur at finite temperature. Many of the experiments in this dissertation probe condensation in a two dimensional system; therefore we must note why the reasons why condensation should be possible.

For one, we do not observe excitons in an infinite system; rather, they exist in a finite area. Therefore, the density of states is not continuous; rather, it is discrete and the minimum energy in the integral will not be 0. Hence, the integral will not diverge and for N particles in an area S there will be a transition temperature

$$T_c \sim \frac{T_{dB}}{ln(N)} \sim \frac{T_{dB}}{ln(nS)} \tag{1.3}$$

where the degeneracy temperature T_{dB} is defined as the temperature where the thermal de Broglie wavelength is equal to the inter particle spacing:

$$\lambda_{dB} = n^{-1/2} \rightarrow T_{dB} = \frac{2\pi\hbar^2}{m\mathrm{k}_B} n. \tag{1.4}$$

The excitons studied in this dissertation have mass $m_{ex} = 0.22m_0$, where m_0 is the electron mass in vacuum. For an experimentally accessible density $n \sim 10^{10} cm^{-2}$, $T_{dB} \sim 3$K. Therefore, $T \ll T_{dB}$ can be readily achieved in a liquid helium cryostat or dilution refrigerator.

Futhermore, although Bose-Einstein condensation in its most strict definition can not occur in an infinite 2-dimensional system, superfluidity can occur with a transition temperature on the order of the degeneracy temperature [Popov, 1972]. The presence of dipolar interaction, as in an indirect exciton system, can increase the critical temperature [Filinov *et al.*, 2010]. Similar to Bose-Einstein condensation, superfluidity is characterized by spontaneous extended coherence $\xi \gg \xi_{classical}$, where $\xi_{classical}$ is close to the thermal de Broglie wavelength $\lambda_{dB} = (2\pi\hbar^2/mk_BT)^{1/2}$. Phenomena such as topological defects and coherent spin transport can manifest themselves in a system characterized by spontaneous extended coherence. Such phenomena are explored in chapter 4.

Finally, we can modify the density of states through the addition of a trapping potential. For instance, in an isotropic 2-D harmonic trap $g(\epsilon)$ the eigenstates have energy $\hbar\omega_0 n, n \in \{1, 2, 3...\}$ and degeneracy n. In such a system the critical temperature of Bose-Einstein condensation at fixed particle number scales with ω_0 [Ketterle & van Druten, 1996]. We explore condensation of excitons in a trap in chapter 5.

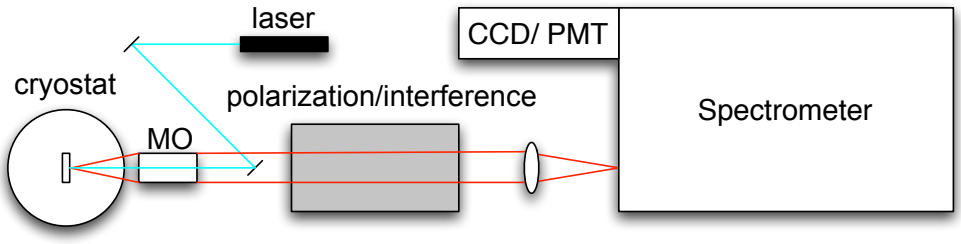

Figure 1.3: Basic experimental schematic for optical measurements. A laser excitation (cyan) creates excitons in the sample (rectangle in the cryostat). Exciton emission (red) is collected and made parallel by a microscope objective (MO). The emission is focused onto the slit of the spectrometer, which also corresponds to the focal plane of the charged-coupled device (CCD) or photo-multiplier tube (PMT) at the output of the spectrometer. The spectrometer provides energy resolution. Optics for polarization and interference measurements are placed in the grey area.

1.2 Measuring the physical properties of excitons

Experimenting with indirect excitons is relatively straightforward, see figure 1.3. To achieve low temperatures, the sample is placed in either a liquid-helium cryostat to achieve lattice temperature $T_{lattice}$ = 1.4K or a dilution refrigerator to achieve $T_{lattice}$ = 50mK. A helium-neon laser is used for excitation of carriers in the bulk AlGaAs. These bulk carriers can be captured by the quantum wells and form excitons; a surplus of holes can also be created as discussed in chapter 4. A titanium-sapphire laser is used for resonant excitation of direct excitons. Then, we use various optical techniques to measure the exciton property in question. In this dissertation, along with basic imaging measurements, we present coherence- , energy-, polarization-, and time-resolved measurements. From the exciton emission, we can learn about the exciton energy, spin and coherence length, all of which can be spatially resolved.

1.3 Historical Background

Research into indirect excitons has a long and fascinating history. The research presented in this dissertation would not exist without an enormous

preexisting theoretical and experimental base. Rather than provide a complete history of the field, this section will provide an overview of significant historical developments relevant to this dissertation.

Development of the Bose-Einstein statistical model:

In two seminal papers, [Einstein, 1924, 1925] Einstein extended Bose's derivation of Plank's law [Bose, 1924] into a description of ideal gases. The derivation relies on the principle of indistinguishability of the component particles. In his second treatise, [Einstein, 1925], Einstein describes a spectacular property of a gas of indistinguishable particles; at any given temperature T, there exists a density n beyond which all excited states in the system are saturated and any additional particles added to the system must reside in the ground state of the system. This is known as Bose-Einstein condensation, and should be a general property of any system of bosons in thermal equilibrium. An exciton is a boson; hence, an exciton could potentially undergo Bose-Einstein condensation.

First theoretical description of excitons:

In 1931, Frenkel considered what happens when a crystal absorbs a photon [Frenkel, 1931]. From the abstract:

> Starting from the analogy between a crystal and molecule, it is shown that the electronic excitation, forming the first step in the process of light absorption, is not confined to a particular atom, but is diluted between all of them in the form of "excitation waves,"...

In other words, when an electron absorbs a photon, it will enter an excited state. This excited state can travel around the crystal without conducting charge. This is the first description of an exciton.

Prediction of Bose-Einstein condensation of excitons:

An exciton is a bound state composed of two fermions. Simply because an exciton has integer spin does not imply that it can be regarded as a structureless boson, such as a photon; rather, the statistical behavior of excitons must be influenced by the fermionic nature of its components. In 1968, Keldysh and

Kozlov, working within the framework of electrons and holes, made a theoretical study of exciton statistics and predicted that in the dilute limit excitons could indeed behave like a weakly non-ideal Bose gas and hence could undergo Bose-Einstein condensation under reasonable experimental conditions [Keldysh & Kozlov, 1968]. The prediction that excitons could undergo Bose-Einstein condensation has been the driving force behind decades of exciton-based research and spurred development of the high-quality GaAs quantum well structures utilized in this thesis.

Suggestion of a spatially-indirect exciton system and prediction of Bose-Einstein condensation therein:

In [Lozovik & Yudson, 1976], the researchers considered a system of paired electrons and holes confined in two spatially separated layers, i.e. the system studied in this dissertation. They suggest that superfluidity and Bose-Einstein condensation could occur in an indirect exciton system, and note some inherent advantages. For instance, In the paper of Keldysh and Koslov, a main point of concern is that excitons could form molecules, which would make an exciton condensate unstable. This is a reasonable concern; in bulk, excitons are attracted to each other by Van der Waals interaction and hence could form molecules. In [Lozovik & Yudson, 1976], the authors observed that in this system the excitons are aligned dipoles and are repulsive to each other; therefore, instability due to molecule formation would no longer be a concern.

Development of high-quality GaAs/AlGaAs quantum well heterostructures and observation of excitons therein:

An ideal quantum well should have a box-like band structure along the z-direction. To achieve this structure, not only do the composite crystal have to be of the highest purity, but the transition from barrier material to well material should be immediate, on the order of the lattice constant, and uniform. If a quantum-well structure is of high enough quality, the electronic energy levels should take well defined values that depend only on the width and depth of the

potential well. In [Chang *et al.*, 1974; Dingle *et al.*, 1974], researchers made the first observation of these well defined energy levels in a GaAs/AlGaAs quantum well heterostructure and showed that energy levels could be well described theoretically. This demonstrated that fabrication of high quality, low disorder quantum wells was indeed possible. In [Chang *et al.*, 1974], researchers demonstrated quantized energy levels through electronic tunneling experiments. In [Dingle *et al.*, 1974], researches performed optical measurements and observed exciton states in a GaAs/AlGaAs quantum well heterostructures. They further observed that the absorption specta was strongly well-width dependent.

First observation of the quantum-confined Stark effect:

In [Wood *et al.*, 1983; Miller *et al.*, 1984, 1985], researchers demonstrated that through the Stark effect they could shift the excitonic absorption of a GaAs/AlGaAs multiple quantum well structure by $\approx 10 - 25$meV by applying an electric field along the z-axis. As discussed previously, the Stark effect is not useful for controlling the exciton energy in bulk materials; however, in quantum well heterostructures the Stark effect becomes a powerful tool for controlling the exciton energy. These papers present the first large-scale,i.e. greater than the exciton binding energy and line-width, electronic control of exciton energy.

Measured exciton lifetime >500 ns:

Perhaps the most important aspect of indirect excitons is that they have a significantly enhanced lifetime compared to direct excitons in the same structure. Without a long lifetime, they could not travel over distances $> 1\mu$m, which would severely limit potential device applications. Furthermore, a prerequisite of Bose-Einstein condensation is thermal equilibrium between the component particles; without a long lifetime, equilibrium cannot be reached. In [Zrenner, 1992], researchers show that in a AlAs/GaAs coupled-quantum well structure indirect exciton lifetimes can exceed 500ns. Within the world of semiconductors, in which physical processes such as cooling and computational processes such as switching occur on the picosecond to nanosecond timescale, this lifetime is

more than sufficient for studies of low-temperature equilibrium physics as well as development of devices.

Creation of drift potentials for indirect excitons:

Much of the work in this dissertation relies on modulating the in-plane exciton potential by modulating electrode voltage at the surface of the heterostructure. This modulation creates drift fields at the quantum well level, and these drift fields can in turn control the exciton flux. In [Hagn *et al.*, 1995], showed that by attaching wires to two ends of a resistive electrode at the surface of their heterostructure, they created a potential gradient across the electrode, which in turn created a potential gradient for the excitons at the quantum well level. This dissertation will present new techniques to modulate the electric field at the quantum well level; however, this result established the principle of in-plane modulation of the exciton potential via modulation of the electrode potential at the surface.

Early indicators of quantum degeneracy in indirect excitons:

In [Butov & Filin, 1998; Spielman *et al.*, 2000; Butov *et al.*, 2001], researchers present the first strong indicators of quantum degeneracy in an indirect exciton system.

In [Butov & Filin, 1998], researchers report a huge increase in the radiative decay rate with both decreasing temperature and increasing magnetic field. This superradiance was interpreted as a result of condensation; for excitons, their radiance increases with the extension of their wavefunction. In a classical gas, the exciton wavefunction extension is small, on the order of the localization length and scattering length [Butov & Filin, 1998]. In a condensate, the wavefunction of an exciton is equivalent to the size of the condensate and can become quite large; hence the radiance should dramatically increase.

In [Spielman *et al.*, 2000], the researchers probe a related system of quantum-hall bilayers. In the case of filling factor 1/2 for each layer in their system, one layer can be regarded as a hole layer, and indirect excitons can form.

In this system, researchers demonstrated a huge temperature dependence in the zero-bias interlayer tunneling rate, an indicator that the electron layer was aligned with the hole layer and hence in a condensed state. In many ways, this is a similar to the enhanced radiative decay rate reported in [Butov & Filin, 1998]; it is noted in this dissertation due to the different techniques utilized to achieve the coherent state.

In [Butov *et al.*, 2001], researchers studied the rise time in the exciton photoluminescence after switching off the laser excitation. The luminescence rate of excitons is strongly temperature dependent. Since the laser is a heating source, under direct laser excitation the excitons are in a high temperature state and the decay rate will be low; when the laser is switched off, they will cool and can decay quickly. This work reports that cooling into the low energy radiative states is strongly density dependent; this is a signature of bosonic stimulated scattering, in which the scattering into the ground state is proportional to the number of particles already in the ground state. Hence, the higher the exciton density, and hence the higher the degeneracy in the ground state, the faster the excitons can cool.

Observation of the MOES:

In [Butov *et al.*, 2002], researchers observed that under certain excitation and gate voltage conditions, rings of luminescence would appear in the plane of the sample, not only in the local area of the laser excitation but also in regions separated by hundreds of microns from the laser excitation. Specifically, a large ring of luminescence would appear, surrounding the region of the laser excitation. Within the larger ring, smaller rings referred to as Localized Bright Spots (LBSs) would appear. The origin of these rings is purely classical; they form on the boundaries of electron-rich and hole-rich regions. This makes them attractive for studies of low temperature excitons, since the excitons when created only release the minimum binding energy and they form far away from the laser, which is a heating source.

Furthermore, the rings exhibit a rather spectacular property when cooled

to low temperature; at some critical temperature, they will spontaneously fragment into beads. This is referred to as the Macroscopically Ordered Exciton State (MOES). This could potentially be caused by potential minima; however, it was demonstrated in [Yang *et al.*, 2007] that the centers of each bead correspond to a peak in the exciton energy, opposite to what would be expected if they were at a potential minima. The formation of beads requires positive feedback to density modulation. Indirect excitons are aligned dipoles and hence are repulsive to eachother; this repulsive interaction would provide negative feedback to density modulation and act against the formation of beads. In [Levitov *et al.*, 2005], it was proposed that the beads form due to a stimulated process in which the exciton creation rate is directly dependent on local exciton density.

Measurement of spontaneous coherence in the MOES:

In the formation of beads and the temperature dependence of the beads there were strong experimental indications that the MOES forms due to a quantum statistical process. In [Yang *et al.*, 2006], researchers using a Mach-Zehnder interferometer with a single-pinhole technique measured a strong increase in the coherence length $\xi >> \xi_{classical}$ of excitons in the MOES with decreasing temperature. Spontaneous coherence with $\xi >> \xi_{classical}$ is a direct measurement of condensation, and will be discussed in detail in later chapters. This is the first measurement of extended spontaneous exciton coherence in an exciton system.

Elimination of exciton ionization by heterostructure geometry:

The exciton based devices presented in this thesis rely on using multiple electrodes to precisely control the exciton energy. When two electrodes are in close proximity to each other and are offset in voltage, large in-plane electric fields can develop. Similar in-plane fields can occur at the edges These in-plane fields can pull the exciton apart, and can limit the usefulness of indirect exciton based devices and traps. In [Hammack *et al.*, 2006a], researchers showed theoretically that if the quantum wells are positioned close to the ground plane of a structure, the in-plane fields are significantly reduced. Hence, losses due to

field ionization can be essentially eliminated. This is a necessary requirement for the development of efficient exciton-based devices.

1.4 Outline of dissertation

This dissertation concerns the control and study of indirect excitons in gallium arsenide (GaAs) coupled quantum wells. An indirect exciton is a bound state of an negatively charged electron and a positively charged hole that are spatially separated. Indirect excitons have myriad properties which make them an exciting platform for the development of novel optoelectronic devices as well as a model system for studies of ultra cold bosons in condensed matter systems. This dissertation follows two intertwined pathways: (1) electronic control of excitons and (2) experimental studies of low temperature excitons. In chapter 2 we present electronic control of excitons and prototype novel optoelectronic devices. In chapter 3 we demonstrate how the same principles of electronic control can create precisely engineered trapping potentials for indirect excitons and present detailed observations of exciton behavior in the traps. In chapter 4 we present detailed coherence and polarization measurements of a different exciton system, the exciton rings. Finally, in chapter 5 we merge elements of chapter 3 and chapter 4 to study condensation of excitons in an electrostatic trap.

Chapter 2

Exciton-based optoelectronic devices

In this chapter, we will demonstrate proof-of-principle operation of exciton-based transistors and circuits. These devices rely on the ability to control excitons electronically and their development not only has ramifications in the development of optoelectronics but also in the studies of the fundamental physics of cold excitons. The control of exciton fluxes opens a pathway to the study of excitons in controllable potential profiles, a bosonic counterpart of electronic mesoscopics, the field which concerns electron transport in potential profiles.

2.1 Motivation

As the communications industry continues its shift into optically based systems, the demand for devices that have the capability to process optical signals in an efficient and expedient manner is steadily increasing. The development of optically based devices that can perform all necessary logic operations (i.e. switching, AND/OR operations) in a simple and compact manner are vital to increasing the speed of information processing.

The advancement of signal processing and communication has led to the development of optoelectronic and all-optical circuits which expand signal processing into an optically active media [Gibbs, 1985; Wakita, 1998]. Semiconductor based optoelectronic components are of particular interest as they can be integrated into circuits in a similar way to electronic integrated circuits. The

advances in this direction include in particular the development of an optoelectronic transistor [Aull *et al.*, 1993] and compact microring [Xu *et al.*, 2005] and Mach-Zehnder [Green *et al.*, 2007] modulators. The latter devices have achieved switching speeds exceeding several GHz with active region dimensions in the range of 10-100 micrometers [Liu *et al.*, 2004; Xu *et al.*, 2005; Green *et al.*, 2007; Jiang *et al.*, 2005; Liu *et al.*, 2008; Chen *et al.*, 2008].

Excitons have been used in the development of semiconductor based optoelectronic devices which utilize an optically active media. Optoelectronic devices operating with excitons include modulators [Miller *et al.*, 1985], storage devices [Lundstrom *et al.*, 1999; Winbow *et al.*, 2007, 2008], field-gradient devices [Hagn *et al.*, 1995; Gärtner *et al.*, 2006; Leonard *et al.*, 2012], and CCD-type devices [Winbow *et al.*, 2011].

Excitons provide a promising platform for the development of new and more efficient signal processing. The key reasons for this are the possibility of high interconnection speed and compactness. A critical challenge in optical communication is improving interconnection speeds [Miller, 2000]. Since an exciton is both optically active and electronically controllable, there is effectively no delay between optical communication and signal processing. Therefore, excitons can yield significant improvements over optical interconnections that rely on electronic signal processing.

Furthermore, conventional photonics devices are large, $\sim 100\mu$m, which limits development of compact circuits [Wakita, 1998]. In comparison, the size of exciton based devices are limited by the size of the exciton wave function, which is approximated by the exciton thermal de Broglie wavelength and is $\sim$ 10 nm at room temperature. Therefore, exciton devices offer the advantage of compactness as well. These advantages are discussed in depth in [Grosso *et al.*, 2009; Baldo & Stojanovic, 2009]. A further advantage of exciton based optoelectronics, that of scalability, will be demonstrated in this chapter.

Exploiting excitonic transport in devices requires the ability to control the exciton energy by an applied gate voltage, and also requires a sufficiently long exciton lifetime so that the excitons can travel over large distances exceeding

the device dimensions. A regular exciton is a neutral particle without a built-in dipole moment. It is therefore only weakly sensitive to an applied electric field. Furthermore, its lifetime in a direct-gap semiconductor is typically less than a nanosecond, allowing it to travel only a small distance before it recombines. It is of particular interest to study the mesoscopics of cold excitons, in analogy to the mesoscopics of electrons where interesting physics emerges at low temperatures. However, the same rapid electron-hole recombination, which does not allow regular excitons to travel over large distances, also does not allow them to reach low temperatures within their short lifetime.

Indirect excitons fulfill these criteria; due to the spatial separation of the electron and hole, indirect excitons have a dipole moment and are hence electronically controllable. Furthermore, the spatial separation between the electron and hole layers suppresses the exciton recombination rate by orders of magnitude so that lifetime of the indirect excitons can well exceed 100 ns. Long-lived indirect excitons can travel over tens and hundreds of microns as demonstrated in Refs. [Hagn *et al.*, 1995; Negoita *et al.*, 1999; Larionov *et al.*, 2000; Butov *et al.*, 2002; Vörös *et al.*, 2005; Ivanov *et al.*, 2006; Gärtner *et al.*, 2006]. For these reasons, indirect excitons for an intriguing platform for the development of novel optoelectronic devices.

In this chapter, we will present proof-of-principle operation of two new devices: the exciton optoelectronic transistor and the excitonic integrated circuit.

2.2 The exciton optoelectronic transistor

One of the critical devices of electronic logic is the transistor - a three terminal device with the current through two terminals controlled by the third terminal. There are many proposals for optoelectronic and all-optical transistors and the modulation of optical signals has been demonstrated using a variety of methods, for review see [Gibbs, 1985; Wakita, 1998].

In this chapter, we demonstrate experimental proof of principle for an exciton optoelectronic transistor (EXOT). The EXOT exploits a new media for the

transistor operation - excitons - and is based on a new physical principle - control of the exciton flux. It is a scalable, monolithically integrated optoelectronic solution that offers high-speed processing capability of optical signals. The first prototype of the EXOT, which is demonstrated here, reaches a contrast ratio of 30 between an *on* state and an *off* state with switching time below 1 ns.

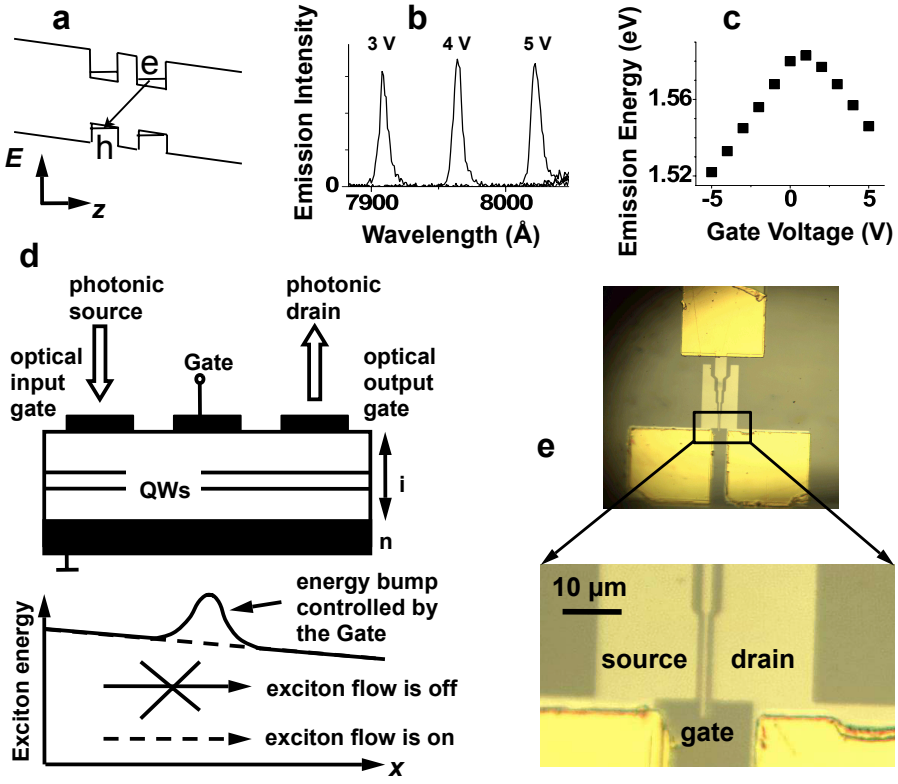

Figure 2.1: Principle of the exciton optoelectronic transistor (EXOT). (a) CQW diagram. (b) Spectrum of indirect excitons at different applied voltages. (c) Energy of indirect excitons as a function of applied voltage. (d) Design schematic for the EXOT. (e) Top view of the device.

The operation principle of the EXOT is based on controlling the flux of excitons via gate voltage. Indirect excitons are dipoles and therefore an electric field F_z perpendicular to the QW plane results in an exciton energy shift $\delta E = eF_z d$, where d is the exciton dipole moment [Miller *et al.*, 1985] (for indirect excitons in CQWs, d is close to the distance between the QW centers [Butov, 2004]). This allows control of indirect exciton energy by gates: An applied gate voltage controls F_z and in turn the indirect exciton energy, Fig. 2.1b,c. We

note that operation principles of general electronic devices are based on electron energy control by gates. A similar control of exciton energy by gates allows the use of indirect excitons in place of electrons in devices.

The operation principle of the EXOT is as follows, 2.1d. The (i) Photons are absorbed at the optical input (source) and create excitons; (ii) Excitons travel from the optical input (source) to the optical output (drain) due to the potential energy gradient $\delta E \sim e(F_{zd} - F_{zs})d \propto (V_d - V_s)d$ created by the difference in the source voltage V_s and drain voltage V_d. The exciton flux from source to drain is controlled by a gate voltage V_g which controls an energy barrier for the indirect excitons in the region of the gate electrode, Fig. 2.1d; (iii) Photons are emitted at the optical output by exciton recombination (since the exciton recombination rate is controlled by F_z, see e.g. [Butov, 2004], optical readout can be driven by applying a voltage pulse to the optical output gate; however this is not employed in the demonstration below).

The EXOT has been realized in a $Al_{0.33}Ga_{0.67}As$/GaAs CQW structure. An n^+-GaAs layer with $n_{Si} = 10^{18}$ cm^{-3} serves as a homogeneous bottom electrode. The source, gate, and drain electrodes were fabricated on the surface of the structure by depositing a thin semitransparent layer of platinum (8 nm) and gold (2 nm) via e-beam epitaxy. A CQW with 8 nm GaAs QWs separated by a 4 nm $Al_{0.33}Ga_{0.67}As$ barrier was positioned 100 nm above the n^+-GaAs layer within an undoped 1 μm thick $Al_{0.33}Ga_{0.67}As$ layer (positioning the CQW closer to the homogeneous electrode suppresses the in-plane electric field near the edges of the electrodes, which otherwise can lead to the exciton dissociation [Hammack *et al.*, 2006a]). The source and drain gate were kept at $V_s = 2$ V and $V_d = 3$ V, and the gate voltage V_g was varied within $0 - 5$ V. The bottom electrode was utilized as a common ground. The transistor gate was 1 μm wide, with 1 μm spacing between both the gate and source and the gate and drain, Fig. 2.1e.

Laser light excites excitons at the EXOT source. For the excitation, we used a beam of 632 nm HeNe laser focused to a spot $\sim 10\mu$m in diameter. The emitted light was diffracted by a single-grating spectrometer and detected by a Peltier-cooled photomultiplier tube and time correlated photon counting

system. The exciton's emission energy depends on the gate voltage, Fig. 2.1b,c, which allowed us to distinguish the exciton emission at the drain region, which occurs at 791 nm for $V_d = 3$ V. The images of the exciton emission were taken by a CCD with a 790 ± 10nm filter, which covers the spectral range of the excitons in the source, gate, and drain regions. In time resolved measurements, the gate voltage was controlled by a pulse generator. The experiments were performed in a He cryostat at $T = 1.4$ K. The profiles of the exciton energy were estimated as in Ref. [Hammack *et al.*, 2006a].

Results of the experiment are shown in Figs. 2.2 and 2.3. Figures 2.2a and 2.2b present control of the flux of indirect excitons across the gate. A contrast between the output signal in an *on* state at $V_g = 5$ V and *off* state at $V_g = 0$ is shown in Fig. 2.2c. In the experiment with pulsed gate voltage, an exponential time constant on the rising edge was $\tau_e \sim 160$ ps and a 10/90 rise time was $\tau_{10/90} \sim 400$ ps, Fig. 2.2d, which indicates that this device is functional at GHz frequencies. The "transfer characteristics" of the EXOT for V_g ranging from 0 to 5 V demonstrates on/off contrast ratio up to 30, Fig. 2.3a. The results agree with our modeling of the electric field profile, Fig. 2.3b: Our estimation suggests that the bump in potential energy between the source and drain disappears around $V_g = 3 - 4$ V, which corresponds to the region of greatest increase in output photon intensity. Our results demonstrate also that the EXOT is operational over a wide range of input powers, Fig. 2.3c (following Ref. [Buchanan, 1996] operational is defined as capable of contrast greater than 3 between *on* and *off* states).

To conclude this section, we have demonstrated experimental proof of principle for an optoelectronic transistor based on the modulation of exciton flux by gate voltage. The exciton optoelectronic transistor (EXOT) implements electronic operation on photons using excitons as intermediate media: the intensity of light emitted at optical output is proportional to intensity of light at optical input and is controlled electronically by the gate. We have demonstrated contrast ratio of 30 between an *on* state and an *off* state of the EXOT and its operation at speeds greater than 1 GHz. A fundamental result of the experiment

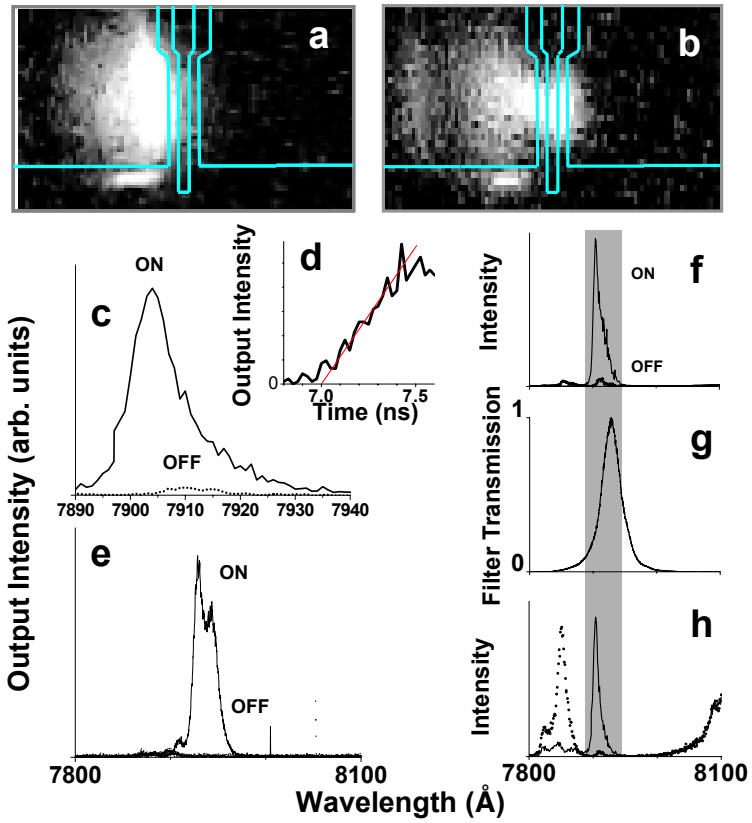

Figure 2.2: Experimental proof of principle of the exciton optoelectronic transistor (EXOT). (a) Emission image at the EXOT in *off* state, $V_g = 0$. (b) Emission image at the EXOT in *on* state, $V_g = 5$ V. Excitons travel from source to drain when the EXOT is in *on* state. Images were taken by CCD using an interference filter with transmission band 790 ± 10 nm. (c) Output spectra for the EXOT in *off* state, $V_g = 0$ (dashed), and *on* state, $V_g = 5$ V (solid), demonstrating on/off contrast. The emitted light was collected at the drain region using the spectrometer slit for the spatial filtering. (e) Similar data for device 2 with interference filtering. The interference filter was built to fit to the spectral area of the EXOT output shown by the gray box in (f-h). (f) The filtered broad range spectra of the off/on states. (g) The interference filter transmission. (h) The broad range spectra of the off/on states without the interference filter. (d) Time resolved output intensity (measured at 791 nm) demonstrating the switching speed of the EXOT. Thin line is a guide for the eye. All data except those in (e) refer to device 1. Input laser power $P_{input} = 430$ μW, $T = 1.4$ K, $V_s = 2$ V, and $V_d = 3$ V for the data.

is a demonstration of control of exciton fluxes and potential energy reliefs for excitons on a time scale much shorter than the exciton lifetime. This opens pathways for studies of excitons in *in-situ* controlled traps, trap lattices, and other

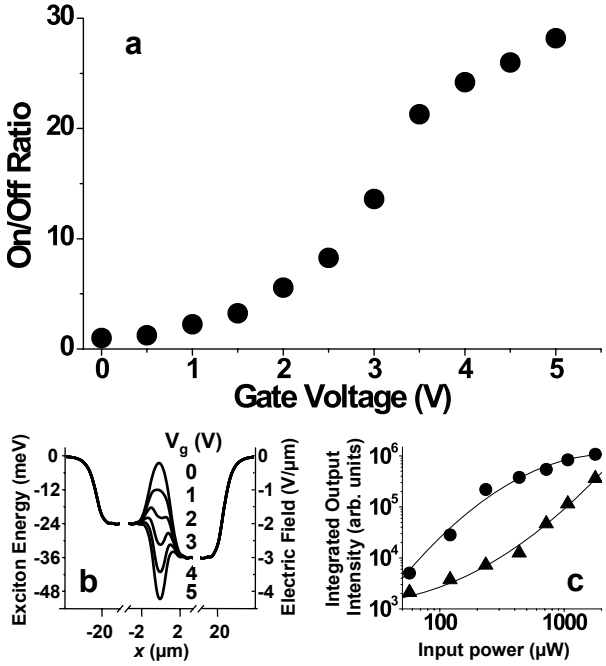

Figure 2.3: Characterization of the exciton optoelectronic transistor (EXOT). (a) Integrated output intensity of the EXOT as a function of gate voltage V_g normalized to that of the EXOT in *off* state at $V_g = 0$. Input photon power $P_{input} = 435\ \mu$W. (b) Modeled profile of potential energy of the indirect excitons (left axis) and electric field F_z (right axis) for $V_g = 0 - 5$ V. (c) Integrated output intensity for the EXOT in *off* state (triangles), $V_g = 0$, and *on* state (circles), $V_g = 5$ V, as a function of P_{input}. Thin lines are a guide for the eye. $T = 1.4$ K, $V_s = 2$ V, $V_d = 3$ V, and spectral integration range is 789-794 nm for the data.

potentials.

2.3 The excitonic integrated circuit

In the previous section, we demonstrated the development of an exciton based transistor. Considering the geometry of the device mirrors that of a FET, the EXOT has the potential to be integrated into circuits in a similar manner, thus providing an opportunity to create high speed optoelectronic integrated circuits for optical signal processing.

In this chapter, we demonstrate control of exciton fluxes in an excitonic integrated circuit (EXIC). The circuit consists of three exciton optoelectronic transistors and performs operations with exciton fluxes such as directional switching and merging. Photons transform to excitons at the circuit input and the excitons transform to photons at the circuit output. The exciton flux from the input to the output is controlled by a pattern of the electrode voltages.

We built an excitonic integrated circuit (EXIC), which consists of three exciton optoelectronic transistors (EXOTs). The sample structure and fabrication techniques are identical to that of the previous section. First, we will discuss the performance of a single EXOT in the new geometry, Fig. 2.4c. The excitons are excited in the source electrode and travel from the input (source) to the output (drain) due to the potential energy gradient $\delta E \sim e(F_{zd}-F_{zs})d \propto (V_{zd}-V_{zs})d$ created by the difference in the source voltage V_s and drain voltage V_d. The exciton flux from source to drain is controlled by a gate voltage V_g which controls an energy barrier for the indirect excitons in the region of the gate electrode. The emission image for one of the EXOTs in OFF state and ON state is shown in Fig. 2.4d and 2.4e, respectively. Figure 2.4f shows that the ON/OFF ratio of the signal integrated over the output exceeds 30. The distance between source and drain for the EXOT is 3 μm (limited by the resolution of the lithography used for the sample processing). It may be expected that the EXOT spatial dimensions can be reduced below 1 μm, thereby permitting a high packing density, one of the key advantages of electronic integrated circuits.

The device geometry allows the construction of excitonic integrated circuits. For instance, a drain of one EXOT can serve as a source of another EXOT. Fig. 2.5 presents the integrated circuit in which three EXOTs have a common

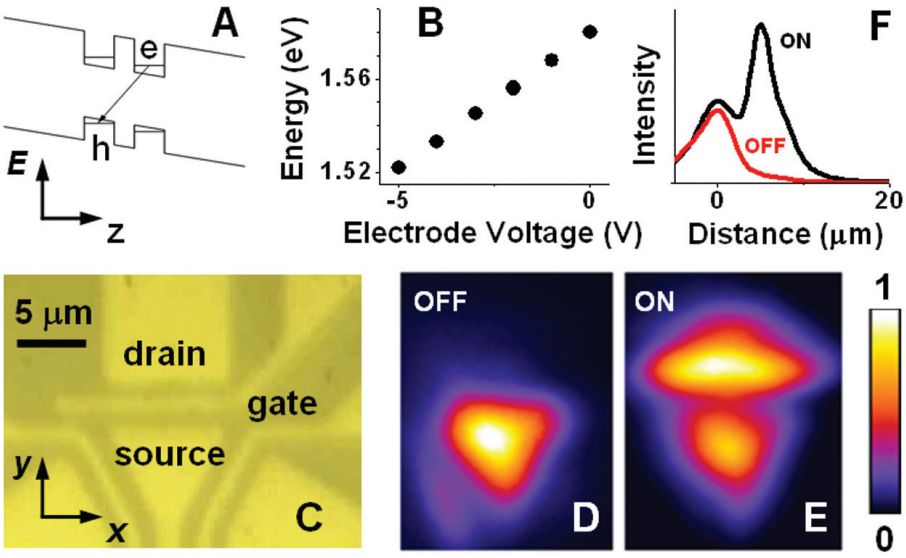

Figure 2.4: Operation of an exciton optoelectronic transistor (EXOT) within an excitonic integrated circuit. (a) Energy band diagram of the CQW structure; e, electron; h, hole. (b) Control of the energy of the indirect excitons by gate voltage. (c-e) Realization of the EXOT. (c) Electrode pattern. (d,e) Emission of the EXOT in OFF (d) and ON (e) states. The excitons are excited in the source electrode. The energy gradient for the indirect excitons from source towards drain is created by the electrode voltages $V_{source} = -1.5$ and $V_{drain} = -2.5$. The exciton flux is controlled by gate electrode; $V_{gate} = 0$ for OFF state; $V_{gate} = -3$V for ON state. (f) Emission intensity along the exciton flux for OFF (red line) and ON (black line) regimes (correspond to the false color images in (d) and (e)).

electrode and form the geometry of a three-beam star. This excitonic integrated circuit can perform several operations with the exciton fluxes, determined by the patterns of the exciton photoexcitation and the electrode voltage.

The first scheme demonstrates directional switching of the exciton flux. The excitons are photoexcited at the input of the top EXOT (electrode 1) and travel to the left and right paths (electrodes 2 and 3, respectively) due to the potential energy gradient, which is created by the voltages on electrodes 1-4. The exciton flux is controlled by the voltages on the gate electrodes V_{g1}, V_{g2}, and V_{g3}, as demonstrated in Fig. 2.5b. Opening the right gate and closing the left gate directs the exciton flux to the right path, while exchanging V_{g2} and V_{g3} switches the flux direction. The exciton fluxes are visualized by the exciton emission. Figure 2.5e shows that the ON/OFF ratio of the excitonic directional

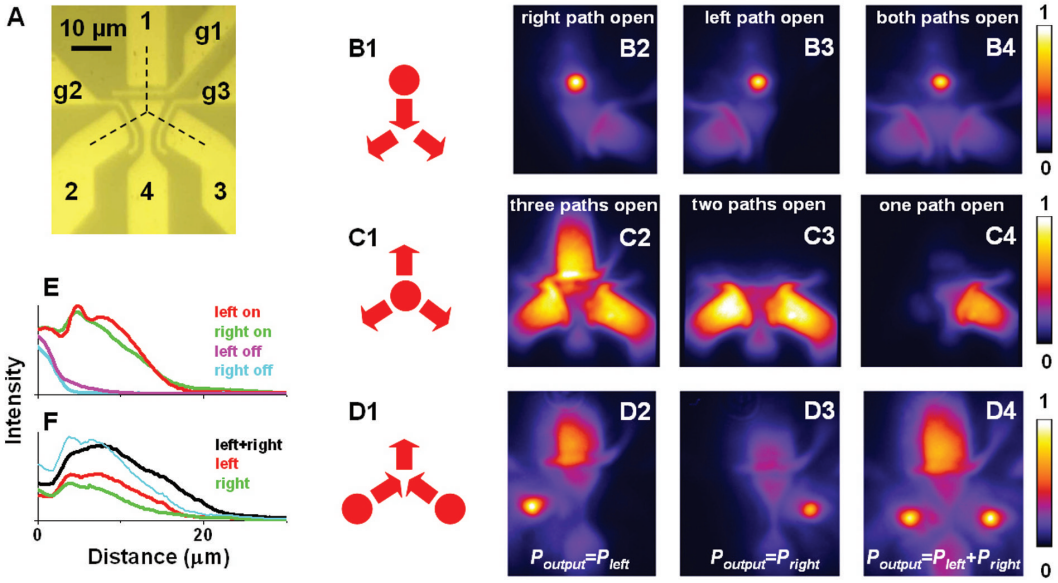

Figure 2.5: Operation of the excitonic integrated circuit. (a) Electrode pattern. (b1,c1,d1) Schematics for photoexcitation spots (points) and fluxes (arrows) of indirect excitons in the circuit. (b1-b4) Demonstration of the directional switch. The excitons are photoexcited at electrode 1. The energy gradient for the indirect excitons from electrode 1 towards electrodes 2 and 3 is created by the electrode voltages V_1=-0.5 V, V_4=-1.5 V, V_2=V_3=-2.5 V, and V_{g1}=-2 V. The exciton fluxes are directed by electrodes g2 and g3; for (b2) V_{g2}=0, V_{g3}=-3 V; for (B3) V_{g2}=-3 V, V_{g3}=0; for (b4) V_{g2}=-3 V, V_{g3}=-3 V. (c1-c4) Demonstration of the star switch. The excitons are photoexcited at the center. The energy gradient for the indirect excitons from electrode 4 towards electrodes 1-3 is created by the electrode voltages, V_1=V_2=V_3=-1.5 V, V_4=-0.5 V. The exciton fluxes are directed by electrodes g1-g3; for (c2) V_{g1}=V_{g2}=V_{g3}=-2 V; for (c3) V_{g1}=0 V, V_{g2}=V_{g3}=-2 V; for (c4) V_{g1}=V_{g2}=0, V_{g3}=-2 V. (d1-d4) Demonstration of flux merging for indirect excitons. The excitons are photoexcited at electrodes 2 (d2), 3 (d3), or 2 and 3 (d4). The energy gradient for the indirect excitons from electrodes 2 and 3 towards electrode 1 is created by the electrode voltages V_1=-2.5 V, V_2=V_3=-0.5 V, V_4=-1.5 V, V_{g1}=-3 V, V_{g2}=V_{g3}=-2 V. (e) Emission intensity along the exciton fluxes (lower dashed lines in (a)) for the left and right paths of the directional switch in ON and OFF regimes (correspond to the false color images in (b)). (f) Emission intensity along the exciton flux (top dashed line in (a)) for the left, right, and both paths open of the flux merger (correspond to the false color images in (d)). The experimental combined signal integrated over the output is within 5 percent of the sum of the signals from the left and right paths (thin cyan line).

switch exceeds 50. The typical transported exciton density, estimated from the exciton energy shift as in [Hammack *et al.*, 2006b], is $n \sim 5 \times 10^{10} cm^{-2}$ when

the device is open. In turn, the corresponding number of transported excitons $N = nS \sim 10^5$, where S is the area of the exciton cloud at the region of output electrode.

The second scheme demonstrates directional switching of the exciton flux in a star geometry (Fig. 2.5c). The excitons are photoexcited at the common electrode at the center of the circuit and travel to the top, left, and right paths due to the potential energy gradient, which is created by the voltages on electrodes 1-4. The exciton flux is controlled by V_{g1}, V_{g2}, and V_{g3}, which open or close the corresponding path. Figure 2.5c demonstrates directing the exciton fluxes to three paths (c2), two paths (c3), and one path (c4).

Another scheme demonstrates merging of the exciton fluxes (Fig. 2.5d). The excitons are photoexcited at the electrodes 2 and 3 and travel towards the top electrode due to the potential energy gradient, which is created by the voltages on electrodes 1-4. The exciton fluxes from the left and right arms are controlled by V_{g2} and V_{g3}, respectively. The two fluxes flow to the top separately when only one of the paths is open (d2 and d3) and are combined when both paths are open (d4). When both paths are open the circuit implements the optoelectronic sum operation for the exciton fluxes (d2-d4). Figure 2.5f shows that the excitonic flux merger performs the sum operation with a high accuracy: The experimental combined signal integrated over the output is within 5 percent of the sum of the signals from the left and right paths. Note that the circuit can also implement the all-optical logic AND gate with 1 set at a higher level, which is achieved by the combined input signals from the both paths ($P_{output-1} \approx P_{left} + P_{right}$), and 0 set at a lower level, which cannot be achieved by the left or right input signal separately ($P_{output-0} < P_{left} + P_{right}$).

The exciton energy as a function of coordinate is presented in Fig. 2.6. The images demonstrate the excitons' drift down the potential energy gradient created by the pattern of electrode voltages. Previous studies have shown that in this temperature range and in the presence of a potential energy gradient, exciton transport in a CQW structure can be described by drift and diffusion [Hammack *et al.*, 2006b].

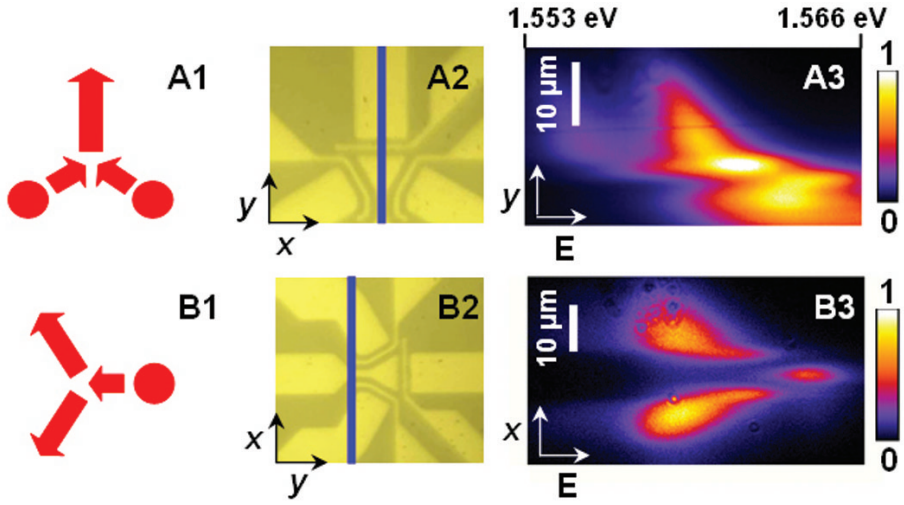

Figure 2.6: Indirect exciton flux follows the energy gradient. (a1) Schematic for indirect exciton fluxes in the flux merger. (a2) x-y image of the excitonic integrated circuit. (a3) Energy-y image of the indirect exciton flux. The exciton energy was dispersed by the spectrometer; the spectrometer slit position is shown by blue line in (a2). Applied voltages and excitation spot positions are the same as in Fig. 2d4. (b1) Schematic for indirect exciton fluxes in the directional switch. (b2) y-x image of the excitonic integrated circuit. (b3) Energy-x image of the indirect exciton flux. The spectrometer slit position is shown by blue line in (b2). Applied voltages and excitation spot position are the same as in Fig. 2b4.

Devices based on excitons can only be operational for temperatures where the excitons exist. This temperature range is determined to be roughly below E_x/k_B, where E_x is the exciton binding energy and k_B is the Boltzmann constant [Chemla *et al.*, 1984]. For indirect excitons formed in a $Al_{0.33}Ga_{0.67}As/GaAs$ CQW structure with d = 12 nm, E_x/k_B is on the order of 40K [Szymanska & Littlewood, 2003]. Note however that E_x can be varied by choosing different semiconductor materials and different structure parameters. For instance, in wide bandgap semiconductor materials E_x/k_B approaches room temperature. The operation temperature is also limited by the possibility of spatial separation of electrons and holes by the applied electric field. The energy eF_zd should be higher than k_BT (e.g. for the sample studied in this paper eF_zd reaches 50 meV ~ 600 K, see Fig. 2.4b). Note also that efficient device operation requires high-quality samples with a low nonradiative recombination rate.

The circuits perform electronic operations on excitons, which can also

be viewed as electronic operations on photons using excitons as intermediate media. Our device operates as a directional switch, star switch, and flux merger. The direct coupling of photons, used in communication, to excitons, used as the device operation media, may lead to the development of efficient exciton-based optoelectronic devices. The demonstrated control of exciton fluxes opens the possibility to study excitons in controllable potential profiles. Virtually any in-plane potential relief can be created for excitons by the appropriately designed voltage pattern, including for instance traps, quantum point contacts, conveyers, and lattices.

2.4 Further work

We have demonstrated that indirect excitons are a promising platform for the development of optoelectronic logic elements. These devices created a foundation upon which further advancements in exciton-based optoelectronics have been made. This section will summarize recent advancements in the field made by our research group.

High temperature operation:

As mentioned previously, GaAs quantum wells only support exciton binding up to temperatures $T \approx 40$K. In general, the higher the temperature at which devices are operational, the more practical they are for real world applications. In that light, in [Grosso *et al.*, 2009] we demonstrate that exciton-based optoelectronics can be operational up to $T \approx 125$K. The devices are based on an AlAs/GaAs coupled quantum well structure. A small $d \sim 3$ nm results in a high binding energy of indirect excitons in such CQW $E_{ex}/k_B \sim 100$ K [Zrenner, 1992], permitting device operation at elevated temperatures. The devices include the exciton optoelectronic transistor (EXOT), the excitonic bridge modulator (EXBM), and the excitonic pinch-off modulator (EXPOM). This is a two orders of magnitude increase in the operation temperature compared to the earlier devices, which were shown to operate at $T = 1.4$K.

All-optical exciton transistor:

The demonstrated exciton transistors have a photonic input and a photonic output. However, they are controlled electronically. It would be advantageous to show that these devices can also be controlled optically. Such operation is demonstrated in [Kuznetsova *et al.*, 2010]. In this paper, the main advancement is the inclusion of a metal-semiconductor-metal photoconnector to the structure. Then, it is shown that an optical input can modulate the gate potential, and hence turn the transistor off and on. Promisingly, it is further demonstrated that light at 786nm can control the device. This wavelength is in the range of the exciton wavelength; this suggests that the output of one transistor could be used to control the gate voltage of another transistor, and hence allow daisy chaining of excitonic devices and perhaps amplification of exciton signals.

2.5 Acknowledgements

The text of chapter 2, in part, is a reprint of the material as it appears in A.A. High, A.T. Hammack, L.V. Butov, M, Hanson & A.C. Gossard, *Exciton optoelectronic transistor*, Optics Letters 32, 2466 (2007), ©Optical Society of America, where the dissertation author was the first author. The co-authors in this publication directed, supervised, and co-worked on the research which forms the basis of this chapter.

The text of chapter 2, in part, is a reprint of the material as it appears in A.A. High, E.E. Novitskaya, L.V. Butov, M. Hanson & A.C. Gossard, *Control of exciton fluxes in an excitonic integrated circuit*, Science 321, 229 (2008); published online 19 June 2008, ©American Academy for the Advancement of Science, where the dissertation author was the first author. The co-authors in this publication directed, supervised, and co-worked on the research which forms the basis of this chapter.

Chapter 3

Excitons in electrostatic traps

3.1 Motivation

One of the most stunning developments of the last twenty years in physics was the observation of Bose-Einstein condensation (BEC) in cold atomic gases [Anderson *et al.*, 1995; Bradley *et al.*, 1995; Davis *et al.*, 1995]. The researchers observed a dramatic phase change from a classical state, in which the momentum distribution was thermal, to a quantum state, in which there was massive occupation of the ground state of the system. The atoms in the ground state became completely indistinguishable from each other, and in effect the researchers succeeded in creating a super particle, in which all the members were in perfect phase.

However, it was not enough to simply hold a collection of atoms in place and wait for them to condense; rather, to achieve the ultra-cold temperatures necessary for BEC, the researchers were required to develop sophisticated traps which could not only hold the atoms but could cool them at the same time. The development of evaporative cooling was a critical step towards achieving atomic BEC.

Traps have also been of fundamental interest in studies of indirect excitons. As a bosonic particle, excitons are expected to undergo BEC at low temperatures, see the discussion in chapter 1. This phase transition will be

density dependent. Therefore, it is of general interest to develop a trap that will efficiently collect excitons into the trap center. Since indirect excitons are electronically controllable they lend themselves well to electrostatic traps, and in fact many electrostatic traps have been prototyped [Huber *et al.*, 1998; Hammack *et al.*, 2006a; Chen *et al.*, 2006; Gorbunov & Timofeev, 2006; Schinner *et al.*, 2011]. Electrostatic traps are of particular interest because they offer the possibility of controlling the exciton potential *in situ*. Along with electrostatic traps excitons were studied in a variety of traps including strain-induced traps [Trauernicht *et al.*, 1983; Kash *et al.*, 1988; Naka & Nagasawa, 2005; Yoshioka *et al.*, 2011], traps created by laser-induced interdiffusion [Brunner *et al.*, 1992], magnetic traps [Christianen *et al.*, 1998], and laser-induced traps [Hammack *et al.*, 2006b; Alloing *et al.*, 2012].

In this chapter, we present the development of precision-engineered electrostatic traps for indirect excitons. In particular, we demonstrate two new traps; the elevated trap and the diamond trap. These traps offer unique advantages over existing techniques, including evaporative cooling of the exciton cloud as well as efficient collection of excitons to the trap center. We utilize the traps to gain insight into exciton-exciton interaction and exciton screening of the disorder potential.

3.2 The Elevated Trap

In this section, we present studies of indirect excitons in an elevated trap. The elevated trap allows evaporative cooling of the exciton cloud. The transition from a normal to elevated trap results in the appearance of narrow lines in the emission spectrum. The density, temperature, and voltage dependences indicate that these lines correspond to the emission of individual states of indirect excitons in a disorder potential in the elevated trap. We show that the linewidth of the exciton emission is a combination of inhomogeneous broadening due to the disorder potential as well as homogenous broadening due to exciton-exciton interaction.

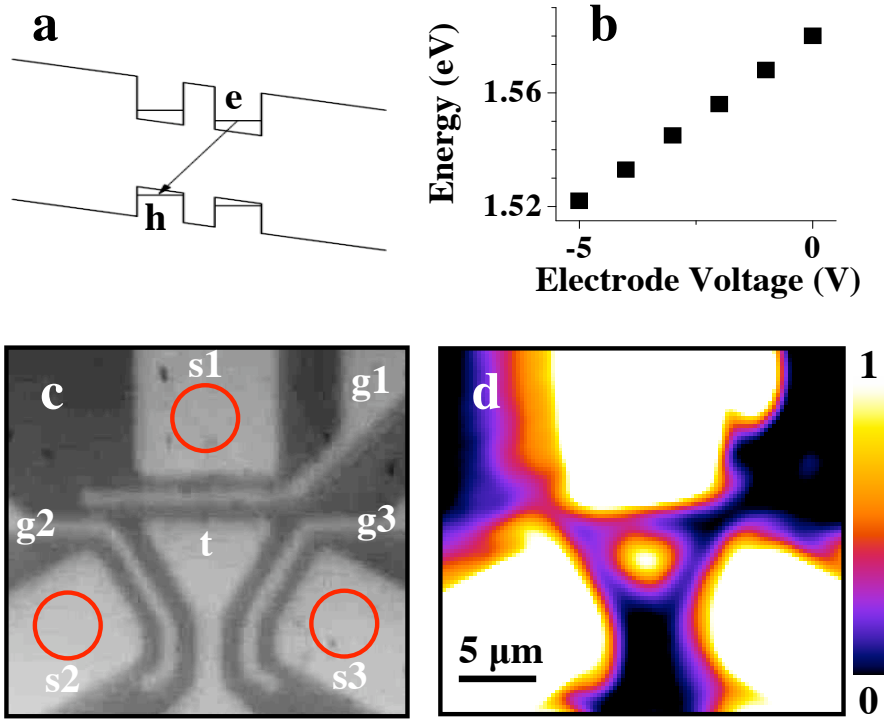

Figure 3.1: Imaging excitons in the elevated trap. (a) Energy band diagram of the CQW structure; e, electron; h, hole. (b) Energy of indirect excitons vs electrode voltage (applies for all electrodes on the sample). (c) Electrode pattern. A trap is formed at electrode t by voltages on electrodes s, g, and t. The circles show the positions of the laser excitation. (d) Emission image of indirect excitons in the elevated trap regime. The cloud of indirect excitons in the elevated trap is in the center. $V_s = -2$ V, $V_g = -1.5$ V, $V_t = -.5$ V, $P_{ex} = 750\mu$W, $T = 1.4$K.

In-plane potential profiles were created by the pattern of electrodes shown in Fig. 3.1c. Elevated traps for indirect excitons in the region of central electrode t were created by applying $|V_t| < |V_g|, |V_s|$, while normal traps were created by applying $|V_t| > |V_g|, |V_s|$. The energy of the elevated trap is above the energy of its surroundings, $E_t > E_g, E_s$ (Fig. 3.2a), while the energy of the normal trap is below, $E_t < E_g, E_s$ (Fig. 3.2c).

The elevated trap was fabricated in a similar manner as the devices in chapter 2. In fact, the elevated trap utilizes the same electrode geometry as the excitonic integrated circuit. The excitons were photoexcited by a 633 nm HeNe laser focused to a spot $\sim 5\mu$m in diameter in the area shown by the

upper circle in Fig. 1c (except the data in Fig. 1d, which was measured with three excitation spots at the three circles in Fig. 1c. The results with one and three excitation spots were qualitatively similar). For the elevated trap regime, excitons in the trap were mainly created by the tail of the laser excitation which reduced heating in the trap area. The emission images were taken by a CCD with an interference filter 800 ± 5 nm, which covers the spectral range of the indirect excitons. The spatial resolution was 1.5 microns. The spectra were measured using a spectrometer with resolution 0.18 meV. All presented spectra were taken from the trap center.

3.2.1 Appearance of sharp lines in the elevated trap

For the entire range of studied densities ($P_{ex} = 1 - 1140\mu$W with the smallest limited by signal strength) the emission spectrum in the normal trap was a structureless line with FWHM > 1 meV, like that in Fig.3.2d. However, sharp lines were observed in the emission spectrum in the elevated trap (Fig.3.2b). FWHM of lines 2-4 were measured as low as 0.18 meV, which is close to the spectrometer resolution. The sharp lines vanish at the transition from the elevated trap to normal trap, i.e. at $E_t \approx E_g$ (Fig.3.2e). They also vanish with increasing bath temperature (Fig.3.2f).

Varying the electrode voltage V_t results in an energy shift of lines 1-4, Fig.3.2g. The measured $\delta E \approx 10.4 V_t$ meV/V corresponds to $d \approx 10.7$ nm, which is close to the nominal distance between the QW centers. Therefore, lines 1-4 correspond to the emission of indirect excitons. Note that sharp lines in the emission of excitons in QWs were observed earlier [Zrenner *et al.*, 1994; Hess *et al.*, 1994; Gammon *et al.*, 1996]. They were attributed to the emission of excitons localized in local minima of the in-plane disorder potential. The latter forms mainly due to QW width and alloy fluctuations [Zrenner *et al.*, 1994; Hess *et al.*, 1994; Gammon *et al.*, 1996; Hegarty *et al.*, 1984; Takagahara, 1985; Zimmermann *et al.*, 1997]. In contrast to the sharp lines in Fig. 3.2, the sharp lines in [Zrenner *et al.*, 1994; Hess *et al.*, 1994; Gammon *et al.*, 1996] correspond to the emission of *direct* excitons with both electrons and holes confined in one QW.

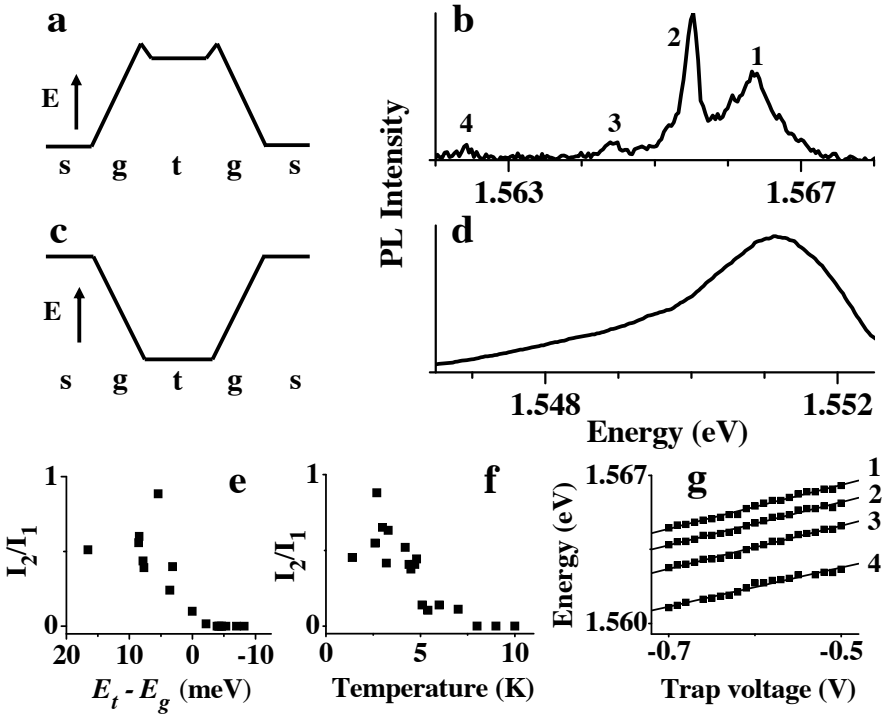

Figure 3.2: Emission spectra of excitons in the elevated trap. (a) Schematic of an elevated trap. (b) Emission spectra of indirect excitons in the elevated trap. $V_s = -2$V, $V_g = -1.5$V, $V_t = -.5$V. (c) Schematic of a normal trap. (d) Emission spectra of indirect excitons in the normal trap. $V_s = -2$V, $V_g = -2.5$V, $V_t = -3.5$V. (e) The ratio of line 2 to line 1 intensities I_2/I_1 vs energy difference between the indirect excitons in the trap and surrounding gates. (f) I_2/I_1 vs bath temperature. $V_s = -2$V, $V_g = -1.5$V, $V_t = -.5$V, $P_{ex} = 6.3\mu$W. (g) Energies of lines 1-4 vs V_t. $V_s = -2$V, $V_g = -1.5$V. For (b,d,e,g), $T = 1.4$K and $P_{ex} = 18\ \mu$W.

In analogy to the interpretation of sharp lines corresponding to the emission of direct excitons [Zrenner *et al.*, 1994; Hess *et al.*, 1994; Gammon *et al.*, 1996], we attribute the observed sharp lines (Fig. 3.2b) to the emission of indirect excitons localized in local minima of the disorder potential in the trap. We note that the local minima of a disorder potential can be considered as "natural quantum dots" [Zrenner *et al.*, 1994]; in turn, natural quantum dots for indirect excitons can be considered as a counterpart of quantum dot pairs and posts [Krenner *et al.*, 2005; Stinaff *et al.*, 2006; Scheibner *et al.*, 2007; Krenner *et al.*, 2008].

In general, the particle localization length is small for the lowest energy states in a disorder potential and increases with increasing energy [Lee &

Ramakrishnan, 1985]. The particle can be considered as localized when the localization length is small compared to the system size, the trap size in our case, and delocalized (over the system) when the localization length is comparable to the system size. The density dependence presented below indicates that low-energy lines 2-4 correspond to the emission of localized states, while high-energy line 1 (which can be a set of unresolved narrower lines) corresponds to the emission of delocalized excitons.

First, we discuss why the sharp lines are observed in the elevated trap regime and vanish in the normal trap regime. The observation of individual localized states in the disorder potential is facilitated by collecting the exciton emission from a small area (Fig.3.1d) containing not too many localized states so that their emission can be resolved. However, both the normal and elevated traps utilize the small area, while sharp lines emerge only in the elevated trap regime (Fig.3.2e). Their emergence is facilitated by an effective "cooling" of the excitons present only in an elevated trap. Since the energy of excitons in the elevated trap is higher than in the surrounding areas, excitons can escape the trap. The escape rate of lower-energy strongly-localized excitons is generally slower. This increases the occupation of lower-energy strongly-localized states in comparison to that of higher-energy weakly-localized (or delocalized) states. An increase in the relative occupation of lower-energy states can be considered as lowering the exciton temperature. This mechanism has similarities with evaporative cooling. In turn, the sharp lines vanish with increasing temperature (Fig.3.2f) and in the normal trap regime where "evaporative cooling" is absent (Fig.3.2e).

Note that in the normal trap the excitons travel to the trap center downhill potential energy gradient that may increase the exciton temperature [Hammack *et al.*, 2006b]. In turn, in the elevated trap traveling uphill may reduce the exciton temperature. However, in the presented experiments this is inessential since the estimated number of excitons which can overpass the potential energy hill and reach the elevated trap is small compared to the number of excitons created in the trap due to the tails of the laser excitation.

One can introduce an effective temperature $\tilde{T}$ for the population balance between the localized and delocalized states as $\delta = n_{\rm deloc}/n_{\rm loc} \sim \exp[-\varepsilon/(k_{\rm B}\tilde{T})]$, where ε is a localization energy. Then the "cooling efficiency" in the elevated trap regime can be quantified by the parameter $\gamma = \delta_{\rm norm}/\delta_{\rm elev}$. A large γ observed in the experiments indicates an efficient cooling. In turn, the temperatures in the elevated trap regime and in the normal trap regime are related by $1/\tilde{T}_{\rm elev} = 1/\tilde{T}_{\rm norm} + (k_{\rm B}/\varepsilon)\ln\gamma$. This allows a rough estimate for $\tilde{T}_{\rm elev}$. Assuming $\gamma \gtrsim 10$ and $\varepsilon/k_{\rm B} \sim 10$K (correspond to line 2, Fig.3.2) and $\tilde{T}_{\rm norm} \sim 3$K (corresponds to a typical temperature of the indirect excitons in the presence of cw excitation and without the "cooling" [Butov *et al.*, 2001; Hammack *et al.*, 2006b]), one obtains $\tilde{T}_{\rm elev} \lesssim 1.8$K.

The "cooling efficiency" γ can be estimated by using the rate equations for occupations of the localized and delocalized states at equilibrium, which result to $\gamma = 1 + \tau/\tau_{\rm esc}$, where $\tau^{-1} = \Lambda^{-1}\tau_{\rm loc}^{-1} + \tau_{\rm opt}^{-1}$, $\Lambda^{-1} = (\Lambda_{\rm l} + \Lambda_{\rm d})/\Lambda_{\rm l}$, $\Lambda_{\rm d}$ ($\Lambda_{\rm l}$) is the population rate of the delocalized (localized) states due to the laser excitation, $\tau_{\rm opt}$ and $\tau_{\rm loc}$ are the radiative and localization times of the delocalized excitons, and $\tau_{\rm esc}$ is their escape time from the elevated trap ($\tau_{\rm esc} \sim S_{\rm trap}/D_{\rm x} \sim 0.1$-$1\,ns$ for elevated trap area $S_{\rm trap} \sim 1\mu$m^2 and diffusion coefficient $D_{\rm x} \sim 10 - 100$ cm^2/s [Ivanov *et al.*, 2006]). For direct excitons with a short lifetime $\tau_{\rm opt} \sim 0.01 - 0.1$ ns, the cooling is inefficient. Indeed, in this case $\gamma < 1 + \tau_{\rm opt}/\tau_{\rm esc} \sim 1.1$. On the contrary, the cooling can be efficient for indirect excitons with a long lifetime $\tau_{\rm opt} \sim 10 - 10^4$ ns. In this case $\gamma \sim 1 + \Lambda\tau_{\rm loc}/\tau_{\rm esc}$. It reaches $\gamma \sim 10$ estimated from the experiments when $\tau_{\rm esc} \sim 0.1\Lambda\tau_{\rm loc}$.

3.2.2 Density dependence of excitons in the elevated trap

The density dependence of the emission of indirect excitons in the elevated trap is presented in Figs.3.3, 3.4. In the entire studied density range, states 1-4 are confined in the elevated trap. This confinement is revealed by the finite spatial extension of all states in the trap $\sim 3\mu$m (Figs. 3.1d, 3.3a). (Note parenthetically that the confinement may involve a small barrier at the trap edges, shown schematically in Fig. 3.2a, however the exact trap profile is beyond the

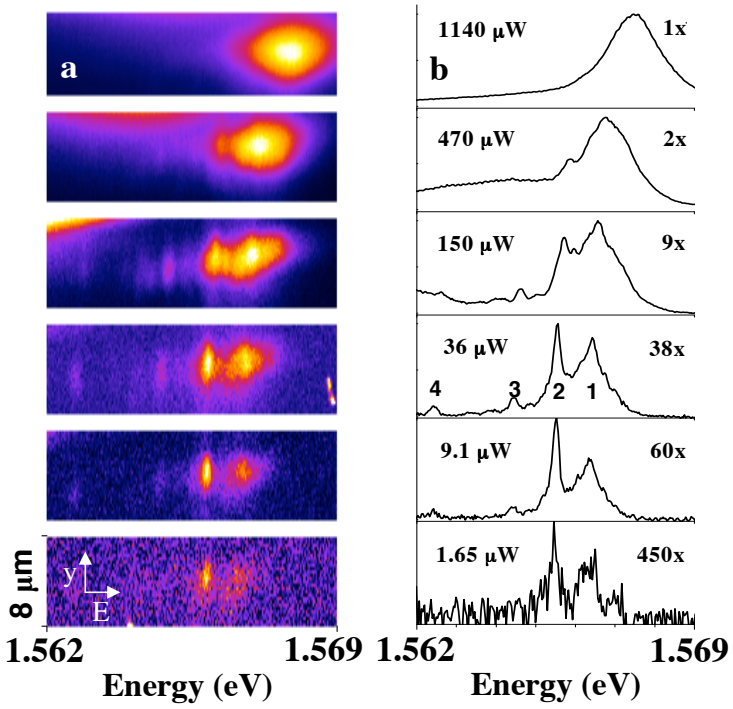

Figure 3.3: Density dependence of excitons in the elevated trap. (a) $E - y$ emission images and (b) spectra of indirect excitons in the elevated trap vs P_{ex}. $V_s = -2$V, $V_g = -1.5$V, $V_t = -.5$V, $T = 1.4$K. P_{ex} and magnification are indicated on (b).

scope of this paper). The features of the density dependence are considered below.

The exciton energy increases with density due to the repulsive dipole-dipole interaction of the indirect excitons (Figs.3.3, 3.4b). The exciton density n can be estimated from the energy shift δE as $n = \epsilon\delta E/(4\pi e^2 d)$ [Yoshioka & Macdonald, 1990; Zhu *et al.*, 1995; Lozovik & Berman, 1996; Ivanov, 2002]. It is presented at the top of Figs.3.4a-c. The energy shift of the localized states is close to that of the delocalized states.

The emission intensity of the localized excitons saturates as shown in Fig.3.4c for line 2. The saturation indicates that only a finite a number of excitons can occupy a local minimum of the disorder potential. For the minimum corresponding to line 2 this number appears to be one. Indeed, if a second exciton were added to the minimum, the energy of the exciton state in it would

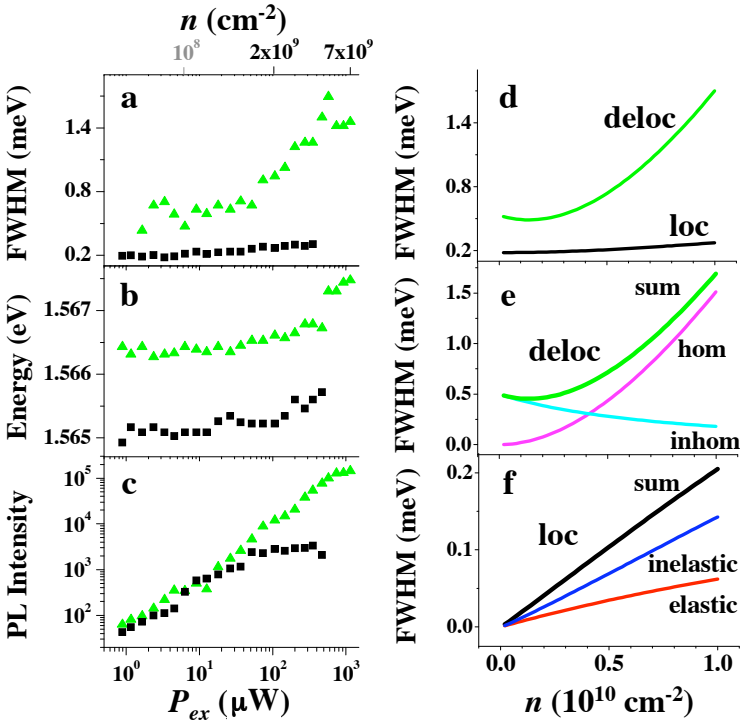

Figure 3.4: Modeling of localized and delocalized exciton interaction. (a) FWHM, (b) energy, and (c) intensity of line 1 (green triangles) and line 2 (black squares) vs P_{ex}. Density listed on top is an estimate based on the exciton energy shift, the lowest value is an estimate based on the PL intensity ratio. $V_s = -2$V, $V_g = -1.5$V, $V_t = -.5$V, $T = 1.4$K. (e) Calculated FWHM of emission line of delocalized indirect excitons (green). Thin lines present the contributions from homogeneous broadening due to exciton-exciton interaction (magenta) and inhomogeneous broadening due to disorder (cyan). The disorder amplitude $U^{(0)}/2 = 0.35$ meV corresponds to line 1. (f) Calculated FWHM of emission line of localized indirect excitons (black). Thin lines present the contributions from inelastic (blue) and elastic (red) exciton scattering. $\varepsilon = 1.3$ meV corresponds to line 2. (d) Calculated FWHM of emission lines including the resolution 0.18 meV for comparison with the experimental data in (a).

increase due to the repulsive interaction. Since the area of the minimum is small compared to the area of the entire trap, adding one more exciton should result to a significant increase of the exciton density in it and, in turn, to a sharp increase of the energy of the localized state. Since no such energy increase is observed (Fig.3.4b), no more than one exciton can occupy the local potential minimum. This is consistent with the small estimated exciton localization length in the

minimum $l_{loc} \sim \hbar/\sqrt{(2M_x\varepsilon)} \sim 10$ nm, comparable to the exciton Bohr radius. The effect is similar to the Coulomb blockade for electrons. It is due to the dipole-dipole repulsion of the indirect excitons.

The emission lines broaden with density (Fig.3.3b, 3.4a). While the widths of lines 2-4 increase by only about 0.1 meV, the width of line 1 increases by more than 1 meV (Fig.3.4a). The strong difference indicates that lines 2-4 correspond to the emission of localized states, while line 1 – delocalized, as discussed below.

The spectral width of the delocalized state emission is approximated by $\Delta_{\rm FWHM} = [\Gamma^2_{\rm hom} + \Gamma^2_{\rm inhom}]^{1/2}$, where $\Gamma_{\rm hom} = \hbar/\tau_{\rm x-x} + \hbar/\tau_{\rm x-LA} + \hbar/\tau_{\rm rec}$ is the homogeneous broadening due to exciton – exciton and exciton – phonon scattering and finite recombination lifetime and $\Gamma_{\rm inhom} = \langle U_{\rm rand}\rangle$ is the inhomogeneous broadening due to disorder, $\langle U_{\rm rand}\rangle$ is the average amplitude of the CQW in-plane long-range disorder potential. For $n \gtrsim 10^8\,{\rm cm}^{-2}$ relevant to the experiments, $\Gamma_{\rm hom}$ is well approximated by $\hbar/\tau_{\rm x-x}$ with $\tau_{\rm x-x}$ given by

$$\frac{1}{\tau_{\rm x-x}} = \left(\frac{u_0 M_{\rm x}}{2\pi}\right)^2 \left(\frac{k_B T}{\hbar^5}\right) e^{-T_0/T} F_0 \int_0^\infty du \int_0^{2\pi} d\phi \times \frac{e^{2u}}{\left[e^{u(1-\cos\phi)} - F_0\right]\left[e^{u(1+\cos\phi)} - F_0\right]\left[e^{2u} - F_0\right]}, \tag{3.1}$$

where $F_0 = 1 - e^{-T_0/T}$, $T_0 = \pi\hbar^2 n/(2M_{\rm x})$, and u_0 is approximated by $u_0 \simeq 4\pi e^2 d/\epsilon$ [Ivanov *et al.*, 1999]. In this sample, excitons have mass M_x=.22m_0. $\Gamma_{\rm hom}(n)$ evaluated with Eq. (3.1) is shown in Fig. 3.4e.

The inhomogeneous broadening is dominant at low densities where the interaction effects vanish. It produces a linewidth of 0.5 meV for the studied sample, Fig.3.4a. The inhomogeneous broadening decreases with increasing density due to screening of the long-range disorder potential by interacting indirect excitons as

$$\Gamma_{\rm inhom} = \frac{U^{(0)}}{1 + [(2M_{\rm x})/(\pi\hbar^2)](e^{T_0/T} - 1)u_0}, \tag{3.2}$$

where $U^{(0)} = 2\langle|U_{\rm rand}(\mathbf{r}_\parallel)|\rangle$ is the amplitude of the unscreened disorder potential, when $n \to 0$ [Ivanov, 2002]. $\Gamma_{\rm inhom}(n)$ evaluated with Eq. (3.2) is shown in Fig.3.4e.

The density increase also results in the homogeneous broadening of the localized states, lines 2-4 (Fig.3.4a), due to the scattering of the localized exciton with delocalized excitons. It is given by $\Gamma_{\rm hom}^{\rm (loc)} = \hbar/\tau_{\rm in} + \hbar/\tau_{\rm el}$ with

$$\frac{\hbar}{\tau_{\rm in}} = \left(\frac{u_0 M_{\rm x}}{2\pi\hbar^2}\right)^2 k_B T\,(1+F_0)\,F_0 \int_{2\Delta}^{\infty} du \int_0^{2\pi} d\phi \times \frac{e^{2u}}{\left[e^{u-\Delta-f(u)\cos\phi} - F_0\right]\left[e^{u-\Delta+f(u)\cos\phi} - F_0\right]\left[e^{2u} - F_0\right]}, \tag{3.3}$$

$$\frac{\hbar}{\tau_{\rm el}} = \left(\frac{u_0 M_{\rm x}}{2\pi\hbar^2}\right)^2 k_B T\,F_0 \int_{0}^{\infty} du \int_0^{2\pi} d\phi \times \frac{e^{u/\cos 2\phi}}{\left[e^{u/\cos 2\phi} - F_0\right]\left[e^{u\tan 2\phi} - F_0\right]}, \tag{3.4}$$

where $f(u) = \sqrt{u(u-2\Delta)}$ and $\Delta = \varepsilon/(2k_{\rm B}T)$. The first (second) contribution is due to the inelastic (elastic) scattering channel "localized exciton + delocalized exciton → delocalized (localized) exciton + delocalized exciton". In elastic scattering the delocalized exciton changes its momentum by the amount which can be relaxed by the localized exciton, $\sim 1/l_{loc}$. The numerical evaluations with Eqs. (3.1),(3.3),(3.4) show that the homogeneous broadening of the localized state is much smaller than that of the delocalized state (Fig. 4e,f). This difference can be attributed to the energy gap ε, which reduces the number of possible states for the scattering of localized excitons. This difference in linewidth broadening with increasing density allows distinguishing the localized from delocalized states and attribute lines 2-4 to the former and lines 1 to the latter. The theoretical and experimental results are in agreement, compare Figs.3.4a and 3.4d.

3.3 The Diamond Trap

Of particular interest is a trap which can provide a confining potential with the exciton energy gradually reducing towards the trap center. Such a parabolic-like potential could collect excitons from a large area, creating a dense exciton gas. This, in turn, can facilitate the creation of a degenerate exciton gas and eventually exciton BEC in the trap.

In this section, we report on the principle and realization of a new electrostatic trap for indirect excitons - the diamond trap. The diamond trap creates a parabolic-like confining potential for excitons with a single electrode. We present studies of exciton behavior in the trap. At low densities and temperatures, excitons in the trap are localized by the disorder potential. However, with increasing density, the disorder is screened by exciton-exciton interaction, and the excitons become free to collect to the trap center. At high density, the trap behaves as a smooth parabolic potential which realizes a cold and dense exciton gas at the trap center.

3.3.1 Creation of a parabolic-like trapping potential

Confining potentials can be made by using multi-ring traps [Hammack *et al.*, 2006a], however such traps require a large number of contacts, which makes the design complex. In contrast, the diamond trap creates a parabolic-like potential using a single electrode. Advantages include simplicity of fabrication and accuracy of control. For instance, switching off the confining potential, like in atomic time-of-flight experiments, or modulating trap depth, like in atomic collective mode experiments, [Cornell & Wieman, 2002; Ketterle, 2002] can be realized by modulating the electrode voltage.

The diamond trap is formed by a single top electrode of a diamond shape, Fig. 3.5c. Since a thinner electrode produces a smaller electric field in the z direction (due to the field divergence near the electrode edges), the potential of the diamond trap $eF_z d$ is deepest at the center, where the electrode is widest, and becomes progressively shallower towards the diamond tips. The trap profile

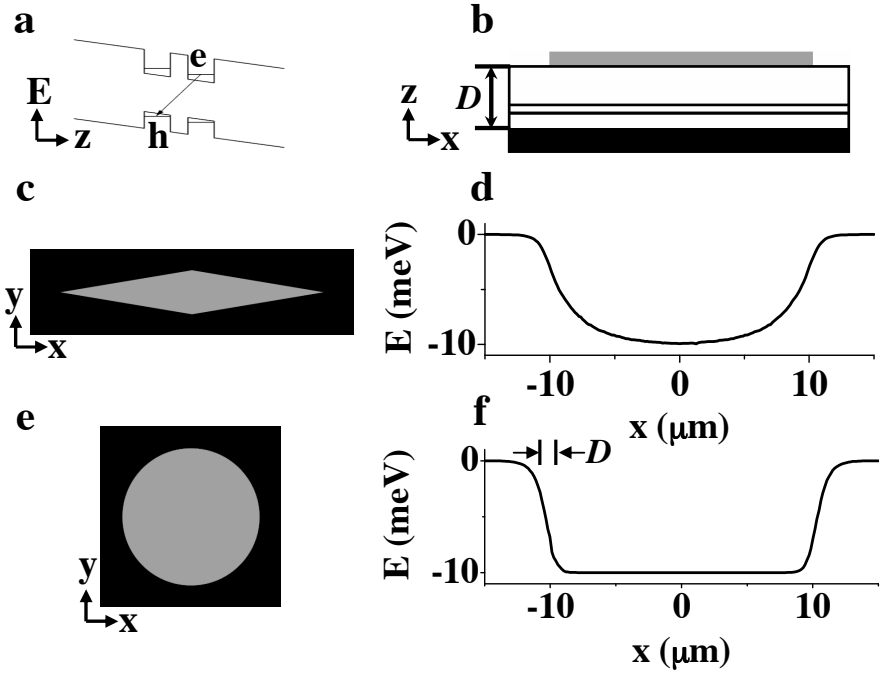

Figure 3.5: Principle of operation for the diamond trap. (a) Energy band diagram of the CQW; e, electron; h, hole. (b) Schematic of device structure. (c,d) A diamond-shaped electrode creates a parabolic-like trap. (e,f) A circular electrode creates a box-like trap. $D = 1\mu$m, the CQW is 100 nm above the bottom electrode, $d = 12$ nm, the diamond electrode is $3.5 \times 20\mu$m, and the applied voltage is 1 V in the calculations..

calculated numerically from the Poisson equation is presented in Fig. 3.5d. Its shape is well approximated by

$$U_{\text{trap}}(x, y) = \frac{-U_0}{2}\left[\tanh\left(\frac{y+w}{a}\right) - \tanh\left(\frac{y-w}{a}\right)\right], \tag{3.5}$$

where a controls the sharpness of the trap and $w = w(x) = L_y(1 - |x|/L_x)$ is the width of the diamond pattern. The calculations show that a parabolic-like in-plane potential is formed by a diamond electrode (the potential is also parabolic-like in y-direction). In comparison, the potential created by a circular electrode is box-like (Fig. 3.5e,f). It varies only within a small length from the electrode edge $\sim D$, where D is the distance between the electrodes, 1 μm in our samples (Fig. 3.5b).

The device includes a $3.5\times30\mu$m diamond electrode, a 600 nm wide 'wire' electrode which surrounds the diamond, and 'outer plane' electrode (Fig. 3.6).

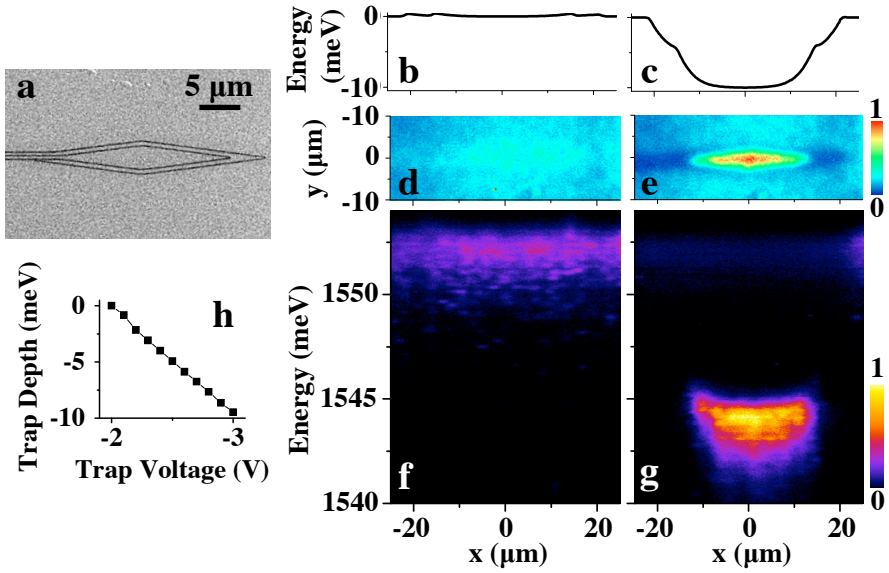

Figure 3.6: Realization of diamond trap as a normal trap. (a) SEM image of the diamond trap. (b,d,f) Flat potential ($V_d = V_w = V_p = -2$ V). (c,e,g) Normal trap ($V_d = -3, V_w = -2.5, V_p = -2$ V). (b,c) Simulation of exciton energy. (d,e) $x - y$ and (f,g) $x - E$ emission images. (h) Trap depth vs. V_d. For all data, $T = 1.4$ K, $\lambda_{ex} = 633$ nm, $P_{ex} = 28\mu$W.

The sample structure and fabrication techniques are the same as in the devices presented in chapter 2. The excitons were photoexcited by a 633 nm HeNe laser or Ti:Sp laser tuned to the direct exciton resonance at 789 nm. The excitation was defocused over the device area. The spectra were measured with resolution 40μeV. The spatial resolution was 1.5μm. Potential profiles were calculated using COMSOL Inc. Multiphysics software.

Experimental results verify the creation of a parabolic-like trap (Fig. 3.6). By varying the diamond electrode voltage V_d with respect to the wire voltage V_w and outer plane voltage V_p, we go from a flat exciton energy (Fig. 3.5b,d,f) to a normal trap (Fig. 3.5c,e,g). The parabolic-like shape of the trap is evident in the $x - E$ emission image (Fig. 3.5g). The collection of excitons to trap center is seen in both the $x - y$ and $x - E$ images (Fig. 3.5e,g).

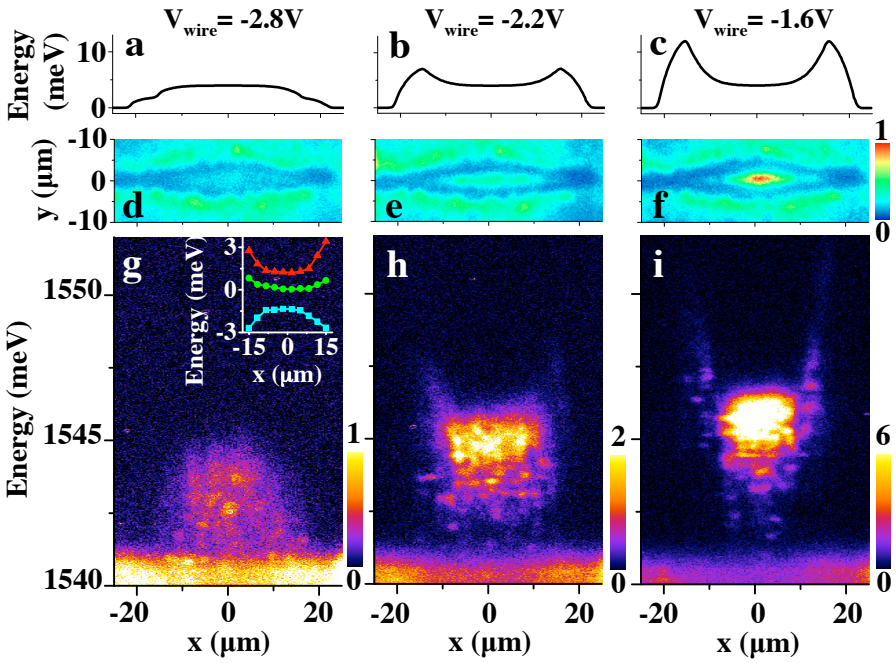

Figure 3.7: Realization of diamond trap as an elevated trap. (a-c) Calculated potential profiles vs. $|V_w|$ showing the transition from a bump to elevated trap. The corresponding $x-y$ (d-f) and $x-E$ (g-i) emission images of the exciton cloud. Inset: The measured trap profile for $|V_w| = 2.8$ (squares), 2.0 (circles), and 1.6 V (triangles). For all data, $T = 1.4$ K, $\lambda_{ex} = 633$ nm, $P_{ex} = 28\mu$W, $V_d = -2.5$ V, $V_p = -3$ V.

3.3.2 The diamond trap as an elevated trap

The 'wire' and 'outer plane' electrodes are not necessary for creating a normal trap. However, they are used for creating an elevated trap in which the trap energy is at a higher energy than its surroundings. This allows evaporative cooling of the exciton gas, since higher energy excitons are more likely to escape the trap than lower energy excitons. The evaporative cooling results in an enhancement of the population of lower energy exciton states localized in local minima of the disorder potential in the trap [High *et al.*, 2009a]. The localized exciton states manifest themselves by sharp emission lines located at the state positions (Figs. 3.7h, 3.8a).

Figure 3.7 demonstrates creation of elevated traps. Varying V_w transforms the energy profile from a bump to elevated trap. Increasing the height of the

trap walls enhances the exciton collection to the trap center. A higher amount of spatially localized sharp lines in the spectrum shows that excitons are more localized in the elevated trap regime than in the normal trap regime (Fig. 3.6g, 3.7h), indicating lower exciton temperature in the former.

3.3.3 Experimental studies of excitons in the diamond trap

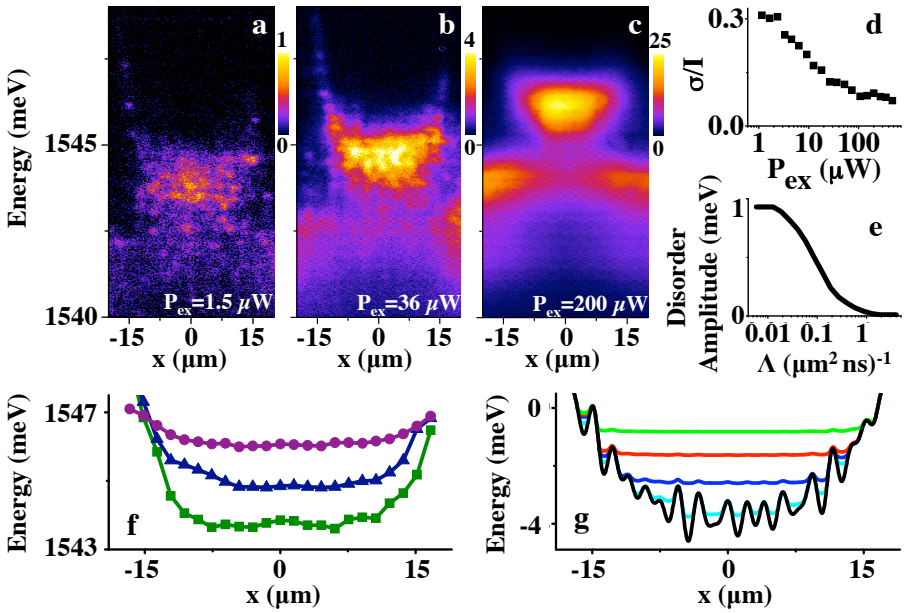

Figure 3.8: Density dependence of excitons in the elevated diamond trap. (a-c) $x-E$ emission images of excitons in an elevated trap for P_{ex} = 1.5, 36, and 200 μW. (d) Ratio of signal variation to signal intensity. (e) Simulated amplitude of 1 meV disorder with increasing exciton density. (f) Energy profile for P_{ex} = 1.5 (squares), 36 (triangles), and 200μW (circles). (g) Simulated energy profile of indirect excitons in a parabolic-like trap with disorder for exciton creation rate Λ = 0.1, 0.5, 1.3, and 2 μm^{-2} ns^{-1} (from bottom to top). For all data, T = 1.4 K, λ_{ex} = 789 nm, $V_d = -2.5$, $V_w = -1.8$, and $V_p = -3$ V.

The remainder of this section concerns the elevated trap regime. Figure 3.8 presents the density dependence. At low density, the excitons are localized in disorder and evenly distributed across the trap (Fig. 3.8a). As the exciton density is increased, the disorder is screened by exciton-exciton interaction as revealed by the disappearance of sharp emission lines, which correspond to the

localized states (Fig. 3.8a-c). This is quantified by the signal variation due to localization σ, which drops with increasing density, indicating screening of the disorder (Fig. 3.8d, the noise contribution to σ is negligible).

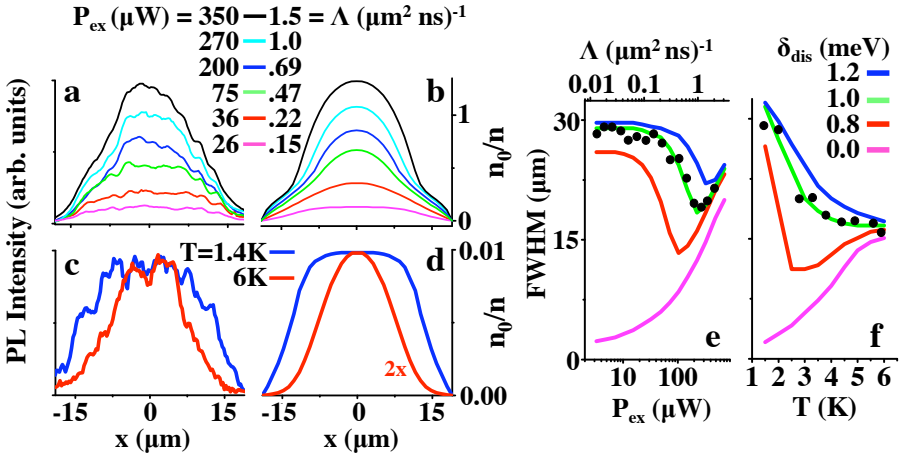

Figure 3.9: Comparison of experiment and modeling of excitons in the elevated diamond trap. (a) Experimental emission profile and (b) simulated density profile of excitons in the trap vs. P_{ex} at T = 1.4 K. n_0 is the density of quantum degeneracy. (c) Experimental emission profile and (d) simulated density profile of excitons for T = 1.4 and 6 K at P_{ex} = 9μW, Λ = 0.05. Experimental (points) and simulated (lines) FWHM of the exciton cloud (e) vs. P_{ex} and Λ at T = 1.4 K and (f) vs. T at P_{ex} = 9μW, Λ=0.05 for different disorder amplitudes. For all data, V_d = −2.5, V_w = −1.8, and V_p = −3 V. λ_{ex} = 789 nm.

At high densities, excitons effectively collect to the trap center. This is revealed by a significant reduction of the exciton cloud width (Fig. 3.8a-c, 3.9a,b,e). We attribute the observed density-enhanced exciton collection to the screening of trap disorder by exciton-exciton interaction. This interpretation is confirmed by the temperature dependence at low densities (Fig. 3.9c,d,f): The exciton cloud width decreases with increasing temperature, consistent with exciton delocalization due to thermal activation over the disorder potential.

3.3.4 Modeling

This interpretation was examined by theoretical estimates. Similar to Ref. [Ivanov *et al.*, 2006], we start with the continuity equation for exciton density

$n(\mathbf{r}, t)$ and current $\mathbf{J}(\mathbf{r}, t)$:

$$\frac{\partial n}{\partial t} + \nabla \mathbf{J} + Rn = \Lambda \,, \tag{3.6}$$

where $R = \tau_r^{-1}$ is the recombination rate and Λ is the generation rate due to photoexcitation. Taking into account the Einstein relation, we can write the current as follows:

$$\mathbf{J} = -D \frac{dn}{d\mu_0} \nabla \left\{ [U(\mathbf{r}) + \gamma \nu_1 n] + \mu_0(n) \right\} . \tag{3.7}$$

Here D is the diffusion coefficient. The terms in the square brackets present the potential acting on the excitons. $U(\mathbf{r})$ is the potential due to trap and disorder and $\gamma \nu_1 n$ is the potential created by exciton-exciton repulsion. The latter is treated as local, neglecting $1/r^3$ dipolar tails. ν_1 is the exciton density of states per spin. The dimensionless parameter γ presents the interaction strength. The last term is the "bare" chemical potential (due to kinetic energy only) given by

$$\mu_0(n, T) = T \ln \left(1 - e^{-n/n_0} \right) , \quad n_0 = g \nu_1 T \,. \tag{3.8}$$

Here n_0 is the density at which exciton gas become quantum degenerate and $g = 4$ is the spin degeneracy.

We measure density in dimensionless units $\tilde{n} \equiv n/n_0$, which has the physical meaning of the Bose occupation factor. $n_0 \approx 1.5 \times 10^{10}\,\mathrm{cm}^{-2} \times T[\mathrm{K}]$. Then

$$\frac{\partial \tilde{n}}{\partial t} + \nabla \tilde{\mathbf{J}} + R\tilde{n} = \frac{\Lambda}{n_0} \,, \tag{3.9}$$

$$\tilde{\mathbf{J}} = -\frac{D}{T} \left(e^{\tilde{n}} - 1 \right) \nabla U - D_{\mathrm{eff}} \nabla \tilde{n} \,, \tag{3.10}$$

$$D_{\mathrm{eff}} = D \left[g\gamma (e^{\tilde{n}} - 1) + 1 \right] . \tag{3.11}$$

In the steady state $\partial \tilde{n}/\partial t = 0$, and Eq. (3.9) becomes

$$\nabla \left(-D_{\mathrm{eff}} \nabla \tilde{n} + \mathbf{J}_{\mathrm{con}} \right) + R\tilde{n} = \frac{\Lambda}{n_0} \,, \tag{3.12}$$

$$\mathbf{J}_{\mathrm{con}} = -\frac{D}{T} \left(e^{\tilde{n}} - 1 \right) \nabla U \,. \tag{3.13}$$

This equation can be obtained from formulas of Ref. [Ivanov *et al.*, 2006] with a simplifying approximation of constant T and R.

In the model, $U = U_{\text{trap}} + U_{\text{dis}}$, with the trap potential given by Eq. (3.5). Disorder in our narrow CQW is primarily due to fluctuations of the QW width. Such fluctuations occur on all length scales. The short-range disorder is accounted for by the diffusion coefficient D. Potential U_{dis} represents the long-range component. It was simulated by three incommensurate lattices $U_{\text{dis}} = (\delta_{dis}/3)(\sin \pi\omega_1 x + \cos \pi\omega_2 x + \sin \pi\omega_3 x), \omega_1 = \sqrt{2}, \omega_2 = \sqrt{3}, \omega_3 = \sqrt{5}\,\mu\,\text{m}^{-1}$. Here δ_{dis} is an adjustable amplitude. The set of equations (8), (9) was solved numerically for $\tilde{n}(\mathbf{r})$. In the calculations, $\gamma = 3$ and $\tau_r = 30$ ns following Refs. [Remeika *et al.*, 2009; Ivanov *et al.*, 2006] and the boundary conditions at the diamond perimeter $\tilde{n} = \Lambda/(Rn_0) = \text{const}$.

The simulations show the screening of disorder by interacting indirect excitons and vanishing of localized states (Fig. 3.8e,g), in agreement with the experiment (Fig. 3.8d). Furthermore, the simulations reveal the role of disorder in exciton collection to the trap center. For zero disorder amplitude, the width of exciton cloud monotonically increases with density due to the screening of U_{trap}. However, for finite disorder, the dependence is nonmonotonic: At low densities, excitons are localized in disorder and broadly distributed over the trap area. As the density increases, excitons begin to screen the disorder U_{dis} and collect towards the trap center, which leads to cloud narrowing. At high densities, the disorder is essentially screened, and excitons begin to screen the long range trap potential U_{trap}, which leads to cloud broadening (Fig. 3.9e). The screening of the potential is also demonstrated by the energy profiles (Fig. 3.8f,g).

Increasing the temperature leads to a monotonic increase of the cloud width for zero disorder due to the thermal occupation of higher energy states in the trap. However, for finite disorder, increasing the temperature first leads to the narrowing of the exciton cloud due to thermal delocalization of excitons and collection to the trap center and then to the cloud widening when delocalized excitons spread over higher energy states in the trap (Fig. 3.9f). The comparison to the experimental data (Fig. 3.9e,f) leads to an estimated long-range disorder amplitude $\delta_{dis} \sim 1$ meV, close to the emission linewidth at low densities. The

model reproduces the experimental narrowing of the exciton cloud with increasing density (Fig. 3.9a,b,e) and temperature (Fig. 3.9c,d,f), thus confirming the interpretation of the density-enhanced narrowing effect in terms of the screening of the trap disorder. At high densities, the trap behaves essentially "disorder free"; compare experimental data with $\delta_{dis} = 0$ line in Fig. 3.9e.

In conclusion, we have shown that a single diamond-shaped electrode creates a parabolic-like potential for indirect excitons. We observed collection of excitons to trap center with increasing density and demonstrated that this effect is due to screening of the trap disorder by exciton-exciton interaction. At high densities, the trap behaves as a smooth parabolic potential which realizes a cold and dense exciton gas at the trap center.

3.4 Further Work

The principle of the diamond trap is to control the electric field at the z-axis by controlling the electrode density at the sample surface. As the electrode becomes thinner, the electric field becomes weaker, and hence the exciton energy increases. This principle of control of exciton energy by density modulation is not limited to diamond shaped electrodes, and in [Kuznetsova *et al.*, 2010] it is shown that essentially any in-plane potential profile can be achieved by modulating the electrode density at the surface through inclusion of holes in the electrode. Of critical importance, the potential profiles can be achieved by using only a *single* electrode. This simplifies design as well as offers protection against the electrical failures that can happen when multiple electrodes are at different voltages, as in the elevated trap and the diamond trap.

This principle of density modulation has been further utilized in [Leonard *et al.*, 2012], in which a linear ramp potential - a diode - for excitons is created through a single electrode.

3.5 Acknowledgements

The text of chapter 3, in part, is a reprint of the material as it appears in A.A. High, A.T. Hammack, L.V. Butov, L. Mouchliadis, A.L. Ivanov, M. Hanson & A.C. Gossard, *Indirect excitons in elevated traps*, Nano Letters 9, 2094 (2009), ©American Chemical Society, where the dissertation author was the first author. The co-authors in this publication directed, supervised, and co-worked on the research which forms the basis of this chapter.

The text of chapter 3, in part, is a reprint of the material as it appears in A.A. High, A.K. Thomas, G. Grosso, M. Remeika, A.T. Hammack, A.D. Meyertholen, M.M. Fogler, L.V. Butov, M. Hanson & A.C. Gossard, *Trapping indirect excitons in a GaAs quantum-well structure with a diamond-shaped electrostatic trap*, Physical Review Letters 103, 087403 (2009), ©American Physical Society, where the dissertation author was the first author. The co-authors in this publication directed, supervised, and co-worked on the research which forms the basis of this chapter.

Chapter 4

Spontaneous coherence and spin textures in cold exciton gases

4.1 Motivation

There are intriguing theoretical predictions for a range of coherent states in cold exciton systems, including BEC [Keldysh & Kozlov, 1968], BCS-like condensate [Keldysh & Kopaev, 1965], charge-density-wave [Chen & Quinn, 1991], and condensate with spontaneous time-reversal symmetry breaking [Wu & Shem, 2008]. Since excitons are much lighter than atoms, quantum degeneracy can be achieved in excitonic systems at temperatures orders of magnitude higher than the micro-Kelvin temperatures needed in atomic vapors [Cornell & Wieman, 2002; Ketterle, 2002]. Exciton gases need be cooled down to a few Kelvin to enter the quantum regime. Although the temperature of the semiconductor crystal lattice T_l can be lowered well below 1 K in He-refrigerators, lowering the temperature of the exciton gas T_X to even a few Kelvin is challenging [Tikhodeev *et al.*, 1998; Jang & Wolfe, 2006]. Due to recombination, excitons have a finite lifetime which is too short to allow cooling to low temperatures in regular semiconductors. In order to create a cold exciton gas with T_X close to T_l, the exciton lifetime should considerably exceed the exciton cooling time. Besides this, the realization of a cold and dense exciton gas requires an excitonic

state to be the ground state and have lower energy than the electron-hole liquid [Keldysh, 1986].

In earlier studies, evidence for spontaneous coherence was obtained for indirect excitons in coupled quantum wells (CQW) [Butov & Filin, 1998] and for indirect excitons in quantum Hall bilayers [Spielman *et al.*, 2000; Eisenstein & MacDonald, 2004]. These experiments are reviewed in chapter 1. The onset of spontaneous coherence was evidenced by a strong enhancement of the recombination [Butov & Filin, 1998] and tunneling [Spielman *et al.*, 2000] rate, respectively. The results of other transport and optical experiments were also consistent with spontaneous coherence of indirect excitons [Butov *et al.*, 1994; Butov & Filin, 1998; Butov *et al.*, 2001; Spielman *et al.*, 2000; Eisenstein & MacDonald, 2004; Tutuc *et al.*, 2004; Tiemann *et al.*, 2008; Karmakar *et al.*, 2009]. However, no direct measurement of coherence has been performed in these studies.

Exciton coherence is imprinted on coherence of their light emission, which one can study by interferometry. In an earlier work, researchers reported an enhancement of the exciton coherence length in the macroscopically ordered exciton state (MOES) [Yang *et al.*, 2006; Fogler *et al.*, 2008]. However, these experiments used a single-pinhole interferometric technique which does not measure the coherence function $g_1(\delta\mathbf{r})$ and the derivation of the exciton coherence length in [Yang *et al.*, 2006; Fogler *et al.*, 2008] was based on a mathematical analysis of the data.

In this dissertation, the studied indirect excitons may have four spin projections on the z direction normal to the CQW plane: $J_z = -2, -1, +1, +2$. The states $J_z = -1$ and $+1$ contribute to left- and right-circularly polarized emission and their coherent superposition to linear polarized emission, while the states $J_z = -2$ and $+2$ are dark [Maialle *et al.*, 1993; Wu & Shem, 2008]. The exciton condensate is a four-component coherent state in general. The build-up of exciton coherence should manifest itself in an increase of the coherence length and polarization degree of the exciton emission. The former phenomenon is general for both one- and multi-component condensates [Penrose & Onsager, 1956] while the latter is specific to multi-component condensates [Read *et al.*,

2009]. In this chapter, we report the emergence of both long-range spontaneous coherence of excitons and spontaneous polarization. A pattern of extended spontaneous coherence, measured by shift-interferometry, is correlated with a pattern of spontaneous polarization, measured by polarization-resolved imaging. These two experiments reveal the properties of a multi-component coherent state.

4.2 Exciton system and experimental schematic for probing coherence and spin

In this section we will discuss the exciton system in question as well as the experimental methods for probing exciton coherence and spin.

4.2.1 The exciton rings

The experiments in this chapter will probe coherence and spin in the region of rings in the exciton emission pattern. Exciton rings, including the inner ring, external ring, and localized bright spot (LBS) rings were observed earlier [Butov *et al.*, 2002]. The external and LBS rings form on the boundaries between electron-rich and hole-rich regions; the former is created by current through the structure (specifically, by the current filament at the LBS center in the case of the LBS ring), while the latter is created by optical excitation [Butov, 2004; Rapaport *et al.*, 2004]. The external and LBS rings are sources of cold excitons. In the area of these rings coherence forms spontaneously. Figure 4.2d shows a segment of the exciton emission pattern with a section of the external ring and smaller LBS rings.

The external and LBS rings provide optimal conditions for the formation of a cold exciton gas for the following reasons: (i) The rings are spatially separated from the optical excitation spot and, therefore, the excitons in the rings are formed from cold electrons and holes thermalized to the lattice temperature, (ii) the heating of the exciton gas due to the binding energy released at the exciton

formation is suppressed due to long lifetimes of indirect excitons, (iii) indirect excitons generated in the rings can further cool down to the lattice temperature when they travel out of the source. The studies of exciton kinetics [Hammack *et al.*, 2009] show that indirect excitons cool down to the lattice temperature within first few microns from the source and the cold indirect excitons can travel over tens of microns out of the source before recombination.

In this work, the area of study is beyond the inner ring, which is formed by indirect excitons traveling away from the optical excitation spot [Ivanov *et al.*, 2006; Hammack *et al.*, 2009]. The photoexcited electrons recombine within the inner ring [Hammack *et al.*, 2009; Ivanov *et al.*, 2006]. Therefore, in the area of external and LBS rings with no photoexcited electrons coherence forms spontaneously; it is not affected by coherence of the optical pumping.

4.2.2 Coherence measurements

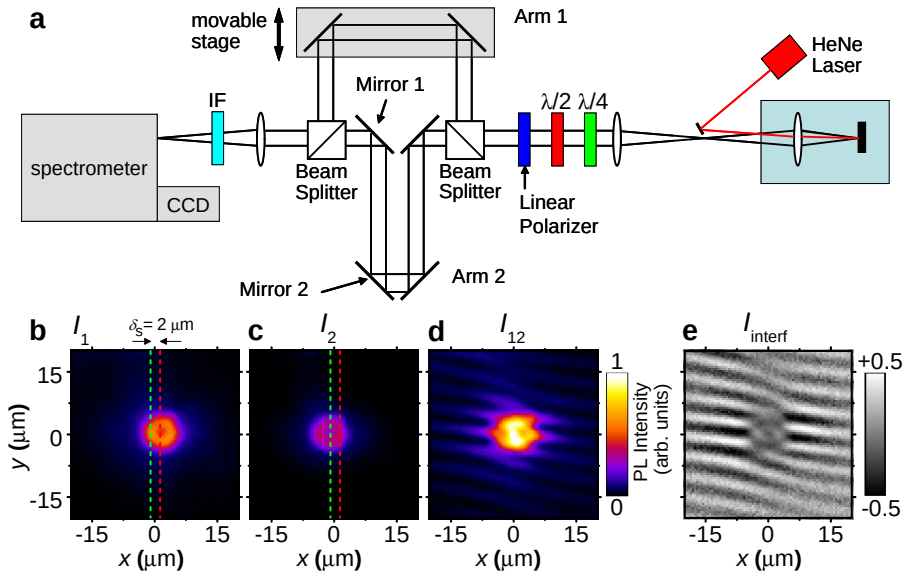

Figure 4.1: Schematic of interference measurements. (a) Interferometric setup. (b-d) Emission image of indirect excitons measured with (b) arm 1 open, (c) arm 2 open, and (d) both arms open. (e) $I_{\text{interf}}(x, y)$ obtained from (b-d). $P_{\text{ex}} = 2.9\,\text{mW}$, $T_{\text{bath}} = 0.1\,\text{K}$.

We use a Mach-Zehnder (MZ) interferometer to probe the coherence of

the exciton system (Fig. 4.1). The emission beam is made parallel by an objective inside the optical dilution refrigerator and lenses. A combination of a quarter-wave plate and a half-wave plate converts the measured polarization of the emission to the y-polarization, which is then selected by a linear polarizer. This ensures only the y-polarized light enters the MZ interferometer thus eliminating polarization-dependent effects, which otherwise can be caused by the interferometer and spectrometer. In the shift-interferometry experiment and polarization-resolved experiment, the spectrometer operates in the zero-order dispersionless regime. The emission is split between arm 1 and arm 2 of the MZ interferometer. The path lengths of arm 1 and arm 2 are set equal using the movable stage. The interfering emission images produced by arm 1 and 2 of the MZ interferometer are shifted relative to each other along x to measure the interference between the emission of excitons, which are laterally separated by δx. Mirror 1 and Mirror 2 are used to control the fringe period, and Mirror 2 is used to control δx. After the interferometer, the emission is filtered by an interference filter of linewidth $\pm 5, \mathrm{nm}$ adjusted to the exciton emission wavelength $\lambda = 800\,\mathrm{nm}$. The filtered signal is then focused to produce an image, which is recorded by a liquid-nitrogen cooled CCD. We measure emission intensity I_1 for arm 1 open, intensity I_2 for arm 2 open, and intensity I_{12} for both arms open, and then calculate

$$I_{\mathrm{interf}} = (I_{12} - I_1 - I_2)/(2\sqrt{I_1 I_2})\,. \tag{4.1}$$

In general, for two partially coherent sources located at $\mathbf{r}_1$ and $\mathbf{r}_2$, one has the relation [Milonni & Eberly, 1988],

$$I_{\mathrm{interf}} = \cos\delta\theta(\mathbf{r}_1, \mathbf{r}_2)\,\zeta(\mathbf{r}_1, \mathbf{r}_2)\,, \tag{4.2}$$

where $\delta\theta(\mathbf{r}_1, \mathbf{r}_2)$ is the phase difference of the two sources and $\zeta(\mathbf{r}_1, \mathbf{r}_2)$ is their degree of coherence. In our experimental geometry, there is a small tilt angle α between the image planes of the two arms. As a result, the phase difference

$$\delta\theta(\mathbf{r}_1, \mathbf{r}_2) = q_t y + \phi(\mathbf{r}_1, \mathbf{r}_2) \tag{4.3}$$

has a component linear in y — the coordinate in the direction perpendicular to the tilt axis — which produces periodic oscillation of I_{interf}. The period of the

interference fringes is set by $q_t = 2\pi\alpha/\lambda$. The coherence function $\zeta(\mathbf{r}_1, \mathbf{r}_2)$ for $\mathbf{r}_1 - \mathbf{r}_2 = \delta\mathbf{x}$ is given by the amplitude of these interference fringes.

4.2.3 Polarization-resolved measurements

The schematic for taking polarization resolved images is also presented in Figure 4.1. Light emitted by the sample is collected and made parallel by a combination of lenses (simplified to one lens in schematic). Polarization selection is done by a combination of quarter-wave plate ($\lambda/4$), half-wave plate ($\lambda/2$), and linear polarizer. The linear polarizer is aligned such that y-axis polarized emission is transmitted to the CCD.

To measure linear polarizations: The quarter-wave plate is aligned so that the fast and slow axis are along the x- and y-axis. Hence, x- and y- polarized emission I_x and I_y are transmitted unchanged. Then, to measure I_y, the half-wave plate fast axis is aligned along the y-axis. I_y is transmitted unchanged, and is then transmitted through the linear polarizer. To measure I_x, the half-wave plate axis is aligned 45° relative to the y-axis. Then, I_x is rotated to the y-axis and is transmitted through the linear polarizer.

To measure circular polarizations The quarter-wave plate is aligned so that the fast and slow axis are rotated by 45° with respect to the y-axis. Then, circularly polarized emission $I_{\sigma+}$ and $I_{\sigma-}$ are converted to x- and y-polarized light. This light is then selected in the same manner as above.

4.3 Spontaneous coherence in a cold exciton gas

4.3.1 Spontaneous patterns of spin and coherence

The pattern of the first-order coherence function $g_1(\delta x)$ is measured by shift-interferometry: the emission images produced by arm 1 and 2 of the Mach-Zehnder interferometer (Fig. 4.2c) are shifted with respect to each other to measure the interference between the emission of excitons spatially separated by δx.

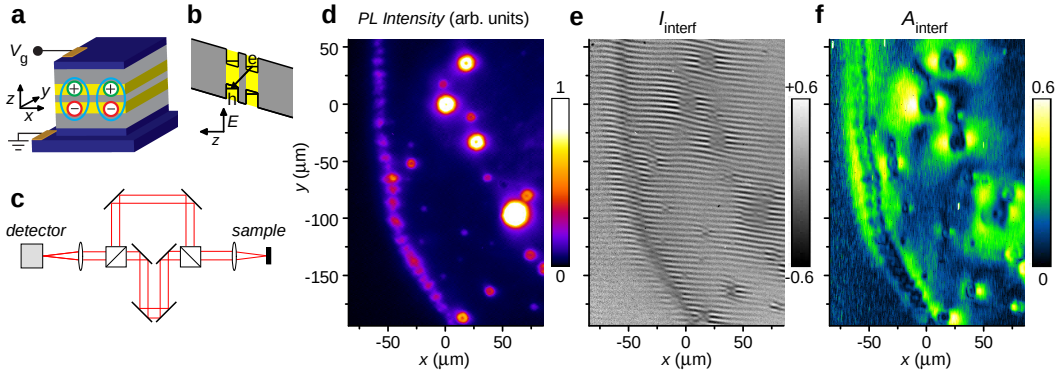

Figure 4.2: Emission, interference, and coherence patterns of indirect excitons in the region of the exciton rings. (a) Schematic of CQW structure: n^+-GaAs (blue), $Al_{0.33}Ga_{0.67}As$ (gray), GaAs QW (yellow). (b) CQW band diagram. (c) Schematic of the interferometric setup. (d) Emission pattern. (e) Interference pattern for $\delta x = -2\,\mu$m. (f) Pattern of amplitude of the interference fringes presenting a map of coherence. $T_{\text{bath}} = 0.1$ K.

Figure 4.2 presents the pattern of interference fringes (Fig. 4.2e) and the map of their amplitude A_{interf} (Fig. 4.2f). A_{interf} describes the coherence degree of excitons as detailed below. The regions of extended spontaneous coherence of excitons correspond to green color in this figure.

Figure 4.3 presents the patterns of coherence of indirect excitons in regions of an LBS and external ring. The observed properties of exciton coherence are qualitatively similar around both these sources of cold excitons. We first consider an LBS region. At low temperatures, a strong enhancement of A_{interf} is observed at distance $r \sim r_0 = 7\,\mu$m away from the LBS center (Figs. 4.3b,c,i). This enhancement of the coherence degree shows the emergence of extended spontaneous coherence of excitons.

Furthermore, the phase of the interference fringes ϕ_{interf} experiences a shift at $r \sim r_0 = 7\,\mu$m, which defines a phase domain boundary (Fig. 4.3b). The shift in phase correlates with the enhancement of A_{interf} (Fig. 4.3b,c). Its magnitude $\delta\phi = \phi^{\text{outer}}_{\text{interf}} - \phi^{\text{inner}}_{\text{interf}}$ increases with δx (Fig. 4.3j). The interference pattern in the shift-interferometry experiment with the shift δx can be simulated using the formula $I_{interf} = |\Psi(\mathbf{r}) + e^{iq_t y}\Psi(\mathbf{r}+\delta\mathbf{x})|^2$, where $q_t = 2\pi\alpha/\lambda$ sets the period of interference fringes (α is a small tilt angle between the image planes of the

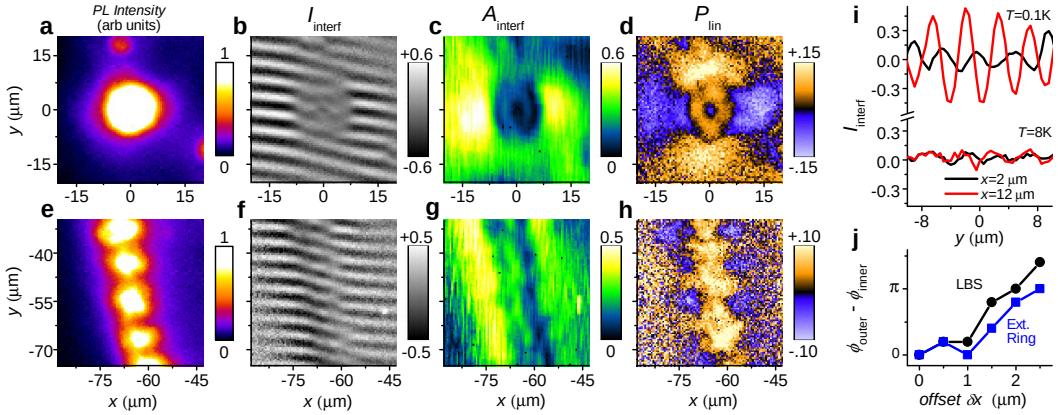

Figure 4.3: Coherence of indirect excitons in regions of an LBS and the external ring. (a-d) refer to the region of an LBS. (e-h) refer to a region of the external ring. (a,e) Emission pattern. (b,f) Interference pattern at shift $\delta x = -2\,\mu$m. (c,g) Amplitude $A_{\rm interf}(x, y)$ of interference fringes. (d,h) Linear polarization of exciton emission $P_{\rm lin} = (I_x - I_y)/(I_x + I_y)$. (i) y axis cross sections of $I_{\rm interf}(x, y)$ at $x = 2\,\mu$m (black lines) and $x = 12\,\mu$m (red lines) at $T_{\rm bath} = 0.1$ K and 8 K. (j) The shift in the phase of interference fringes in (b) at $r \approx 7\,\mu$m (black) and in (f) at $\approx 4\,\mu$m away from the middle circumference of the external ring (blue) *vs.* δx. $T_{\rm bath} = 0.1$ K for (a-h,j).

interferometer arms, λ is the emission wavelength) and the complex function $\Psi(\mathbf{r})$ represents the source amplitude at point $\mathbf{r}$. For a flow of excitons with momentum $\mathbf{q}$, $\Psi(\mathbf{r}) = e^{i\mathbf{qr}}$, so that $I_{interf} = 2 + 2\cos(q_t y + \mathbf{q}\delta\mathbf{x})$ and the shift in the phase of the interference fringes means a jump in (average) exciton momentum $\delta q \sim \delta\phi/\delta x \sim 2\,\mu\text{m}^{-1}$ at $r = r_0$.

Figure 4.3d presents a pattern of linear polarization around an LBS. It spatially correlates with the pattern of the amplitude and phase of the interference fringes, cf. Figs. 4.3b, c, and d. At $r \gtrsim r_0$ a vortex of linear polarization with the polarization perpendicular to the radial direction is observed. Such polarization vortices appear due to precession of the Stokes vector for excitons propagating out of the LBS origin as detailed in a later section.

Figure 4.4 shows that no spontaneous coherence is observed at high temperatures in a classical gas in regions of an LBS and the external ring. This is consistent with a temperature dependent phase transition from a classical gas to a quantum gas.

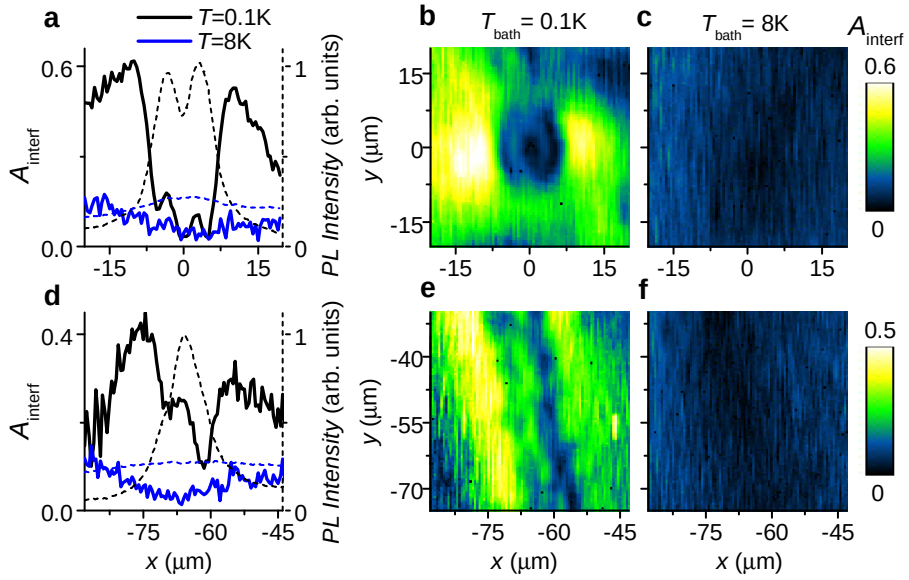

Figure 4.4: Coherence of indirect excitons in regions of an LBS and the external ring: Comparison with high-temperature data. (a-c) refer to the region of the LBS in Fig. 2a. (d-f) refer to the region of the external ring in Fig. 2e. (a,d) x axis cross sections at $y = 0$ (a) and $y = -55\mu$m (d) of $A_{\text{interf}}(x, y)$ at $\delta x = -2\mu$m for $T_{\text{bath}} = 0.1$ K (black solid lines) and 8 K (blue solid lines) and emission intensity for $T_{\text{bath}} = 0.1$ K (black dashed lines) and 8 K (blue dashed lines). (b,c,e,f) $A_{\text{interf}}(x, y)$ at $\delta x = -2\mu$m at $T_{\text{bath}} = 0.1$ K (b,e) and 8 K (c,f).

4.3.2 First-order coherence function of the exciton gas

The measurements of the first-order coherence function are discussed below. Coherence of the exciton gas is directly characterized by coherence of exciton emission, described by the first-order coherence function $g_1(\delta\mathbf{r})$. In turn, this function is given by the amplitude of the interference fringes $A_{\text{interf}}(\delta\mathbf{r})$ in 'the ideal experiment' with perfect spatial resolution. In practice, the measured $A_{\text{interf}}(\delta\mathbf{r})$ is given by the convolution of $g_1(\delta\mathbf{r})$ with the point-spread function (PSF) of the optical system used in the experiment [Fogler *et al.*, 2008]. The PSF width corresponds to the spatial resolution of the optical system ($\sim 1.5\mu$m in our experiments).

The measurements of $A_{\text{interf}}(\delta x)$ in the polarization vortex and in the LBS center are presented in Fig. 4.5a. In the hot LBS center, A_{interf} quickly drops with δx and the shape $A_{\text{interf}}(\delta x)$ fits well to the PSF, which is presented by blue line.

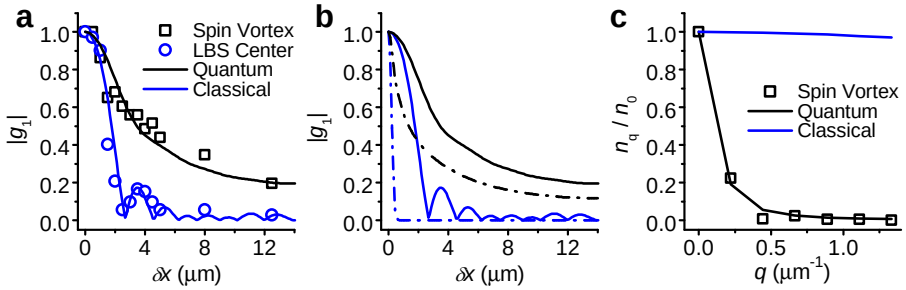

Figure 4.5: First-order coherence function and distribution in momentum space. (a) Measured $|g_1(\delta x)|$ for the polarization vortex (squares) and LBS center (circles) and simulated $|g_1(\delta x)|$ for a quantum (black line) and classical (blue line) gas. (b) Simulated $|g_1(\delta x)|$ for a quantum (black) and classical (blue) gas with (solid) and without (dashed) convolution with PSF. (c) Distribution in momentum space obtained by the Fourier transform of g_1 in (b) for a quantum (black line) and a classical (blue line) gas.

In the polarization vortex, $g_1(\delta x)$ extends to large δx demonstrating extended spontaneous coherence. A fit to the experimental points computed using a model described below is shown by black line.

Figures 4.5b and 4.5c demonstrate the relation between the first-order coherence function and particle distribution in momentum space. Figure 4.5b presents $g_1(\delta x)$ for a classical gas (blue dashed line) and quantum gas (black dashed line) for a spatially homogeneous gas of noninteracting particles with a quadratic dispersion. For a full derivation, see Appendix C. Both gases are at 0.1 K, the classical gas has a very small occupation number $n_0 \ll 1$ of the $q = 0$ momentum state while the quantum gas has $n_0 = 5000$. The convolution of these $g_1(\delta x)$ with the PSF produces black and blue solid lines, which fit to $A_{\text{interf}}(\delta x)$ in the spin polarization vortex and in the LBS center, respectively (Figs. 3a,b). The Fourier transform of $g_1(\delta x)$ in Fig. 4.5b gives the momentum occupation factor n_q in Fig. 4.5c.

Figures 4.5b and 4.5c illustrate that a classical gas is characterized by a broad distribution in momentum space n_q and a narrow first-order coherence function $g_1(r)$, while a quantum gas is characterized by a narrow n_q and an extended $g_1(r)$. For a classical gas, $g_1(r)$ drops within the thermal de Broglie wavelength λ_{dB}, which scales $\propto T^{-1/2}$ and is about 0.5 μm at 0.1 K. The extension

of $g_1(r)$ well beyond λ_{dB} indicates a coherent exciton state.

Figure 4.5a illustrates also why $\delta x = 2\,\mu$m is selected for mapping extended spontaneous coherence of excitons. The shift $\delta x = 2\,\mu$m is chosen to exceed both λ_{dB} and the PSF width. At such δx, only weak coherence given by the PSF value at $\delta x = 2\,\mu$m can be observed for a classical gas. The regions of enhanced coherence exceeding such background level reveal the regions with extended spontaneous coherence of excitons.

4.3.3 Pattern of coherence length

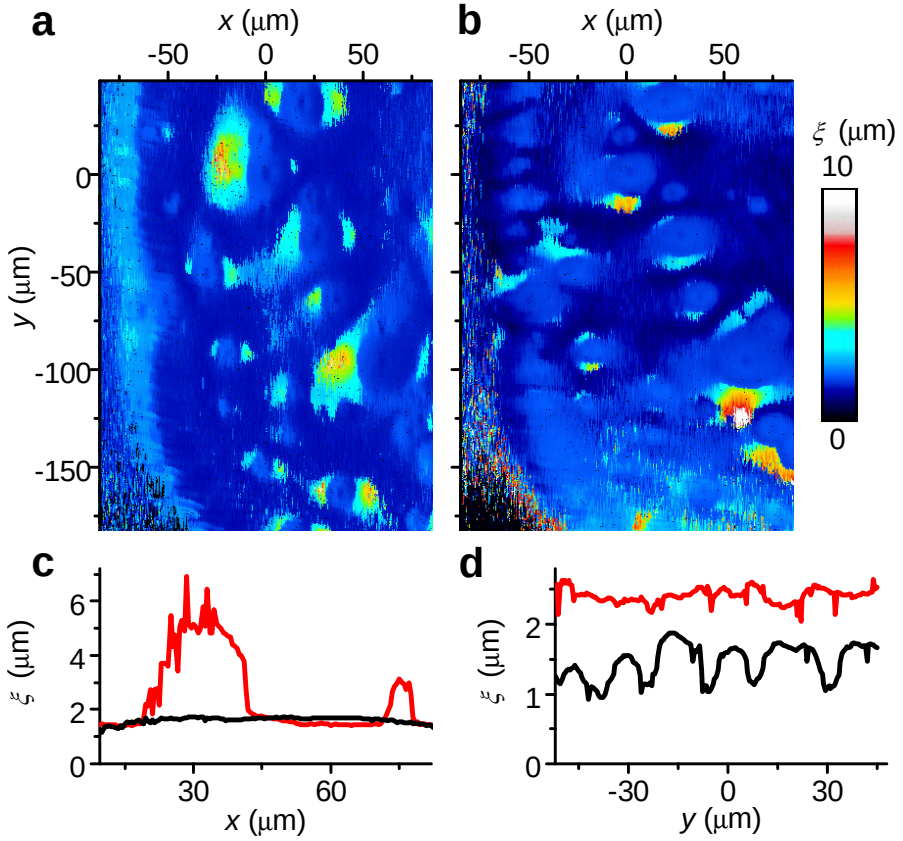

Figure 4.6: Pattern of coherence length of excitons $\xi(x, y)$. (a,b) $\xi(x, y)$ for a shift along (a) x and (b) y. (c,d) Cross section of $\xi(x, y)$ (c) through LBS [$y = -90\,\mu$m] and (d) along external ring [$x = -70\,\mu$m] for a shift along x (red) and y (black). $T_{\text{bath}} = 0.1$ K.

Next, we present a pattern of coherence length. The spatial extension of

$g_1(\delta r)$ can be characterized by a coherence length ξ. To consider all points in the pattern on equal footing, we evaluate ξ as δr at which the interference visibility drops e times. We measured the exciton interference pattern at different δr to produce the spatial map of $g_1(\delta r)$ and, in turn, ξ. Figures 4.6a and 4.6b show the pattern of ξ for the shift between the interfering excitons along x and y, respectively. Figures 4.6c and 4.6d present the cross sections of $\xi(x, y)$ in the region of the polarization vortex (c) and MOES (d).

The regions of a classical gas in the $\xi(x, y)$ pattern correspond to the smallest observed coherence length given by the PSF width. Long-range spontaneous coherence of excitons is observed in the polarization vortices and in the macroscopically ordered exciton state (Fig. 4.6). The coherence length in these regions is much larger than in a classical gas, indicating a coherent state with a much narrower than classical exciton distribution in momentum space, characteristic of a condensate.

The observed coherence length in the polarization vortex exceeds $\lambda_{dB} = 0.5\,\mu$m at 0.1 K by more than order of magnitude (Fig. 4.6). The coherence length in the MOES is smaller than in the polarization vortex. This may be related to fluctuations of the exciton density wave in the external ring. Such fluctuations were observed recently and their studies will be reported in future works.

The patterns of coherence length are different for the shifts along x and y, revealing a directional property of exciton coherence. In the region of the polarization vortices, ξ is higher in the direction along the shift between the interfering excitons [x direction for the δx-shift (Fig. 4.6a), and y direction for the δy-shift (Fig. 4b)]; In the region of the MOES, ξ is higher for δx-shift along the direction of exciton propagation away from the external ring in Fig. 4.6a. These data indicate that the extension of $g_1(\mathbf{r})$ is higher when the exciton propagation direction is along vector $\mathbf{r}$.

4.3.4 Phase singularities in the exciton interference pattern

Finally, we present phase singularities. A well known example of phase singularities is a quantized vortex. In a singly quantized vortex, the phase of

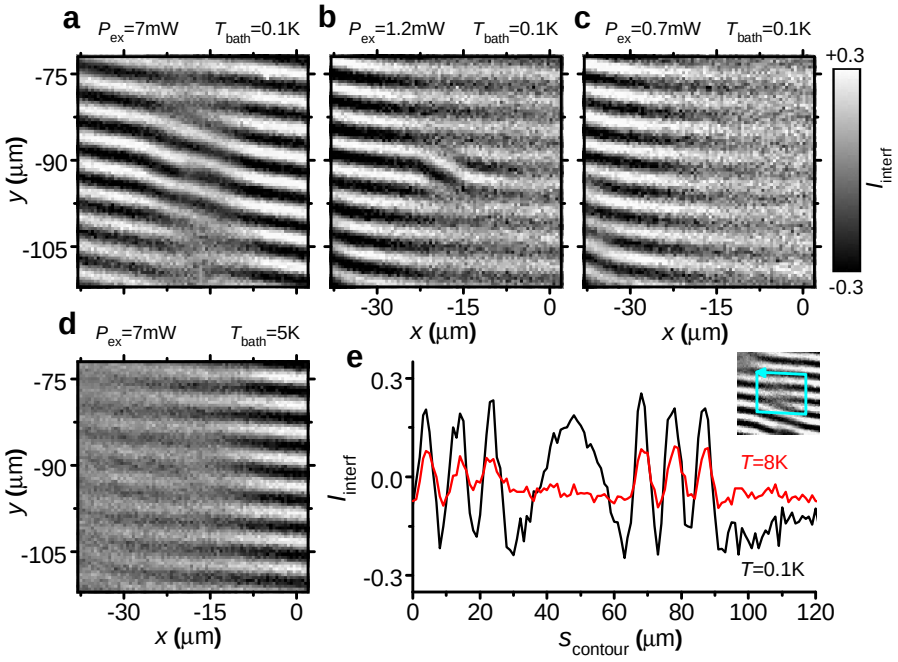

Figure 4.7: Fork-like defects in exciton interference pattern. (a-d) Interference pattern $I_{\text{interf}}(x, y)$ around an LBS vs. (a-c) P_{ex} and (a,d) T_{bath}. (e) I_{interf} along a closed contour [shown in inset] for $T_{bath} = 0.1$ K (black) and 8 K (red). $\delta x = 2\,\mu$m.

the wavefunction winds by 2π around the singularity point that can be revealed as a fork-like defect in a phase pattern. Fork-like defects in interference patterns were reported for optical vortices, vortices in atom condensates, and polariton vortices, see [Scheuer & Orenstein, 1999; Hadzibabic *et al.*, 2006; Lagoudakis *et al.*, 2008] and references therein.

We observed a number of fork-like defects in the interference pattern of a cold exciton gas. For instance more than 20 of them are present in Fig. 4.2e. A larger scale is presented in Fig. 4.7. Figure 4.7a shows forks in the interference pattern indicating the presence of phase singularities. We study the properties of this phenomenon and show that its origin is different from a quantized vortex.

The forks in the interference pattern are observed at low temperatures in a quantum exciton gas (Fig. 4.7a) and vanish at high temperatures in a classical exciton gas (Fig. 4.7d). At low temperatures, a closed contour around the fork crosses an odd number of interference fringes so the phase of the interference fringes winds by 2π, indicating a phase singularity (Fig. 4.7e). Similar properties

are observed for quantized vortices.

However, the distance between the left- and right-facing forks in the interference pattern is different from the shift $\delta x = 2\,\mu$m in the shift-interferometry experiment and depends on the excitation power (Fig. 4.7a-c). This indicates the difference between the observed phase singularity and a quantized vortex. Indeed, straightforward simulations show that a quantized vortex is characterized by a pair of opposite forks separated by a distance equal to the shift in the shift-interferometry experiment (see the following section).

4.3.5 Simulation of the interference patterns

The interference pattern in the shift-interferometry experiment is simulated using the formula

$$I_{12} = |\Psi(\mathbf{r}) + e^{iq_t y}\Psi(\mathbf{r} + \delta\mathbf{x})|^2, \tag{4.4}$$

where the complex function $\Psi(\mathbf{r})$ represents the source amplitude at point $\mathbf{r}$ and δx is the in-plane shift.

First, we considered a quantized vortex. The simulations (Fig. 4.8) show that a quantized vortex is characterized by a pair of opposite forks separated by the distance equal to the shift in the shift-interferometry experiment.

The shift $\delta x = 2\,\mu$m (Fig. 4.8a) is close to the shift in the experiment (Figs. 4.7a and 4.9a). Clearly, the interference pattern produced by a quantized vortex (Fig. 4.8a) is different from the interference pattern observed in our experiment (Fig. 4.9a), where the distance between the left- and right-facing forks in the interference pattern is not equal to the shift $\delta x = 2\,\mu$m in the shift-interferometry experiment. This indicates the difference between the observed phase singularity and a quantized vortex.

We also considered an amplitude function Ψ, which is composed of a large number (24) of mutually incoherent radial waves $J_0(q|\mathbf{r} - \mathbf{r}_j|)$ whose centers $\mathbf{r}_j$ are uniformly distributed along a ring (the ring radius is 8μm in the simulations). Here $J_0(z)$ is the Bessel function. Each of these sources had the same radial momentum q. The simulations of the interference pattern produced by a ring-

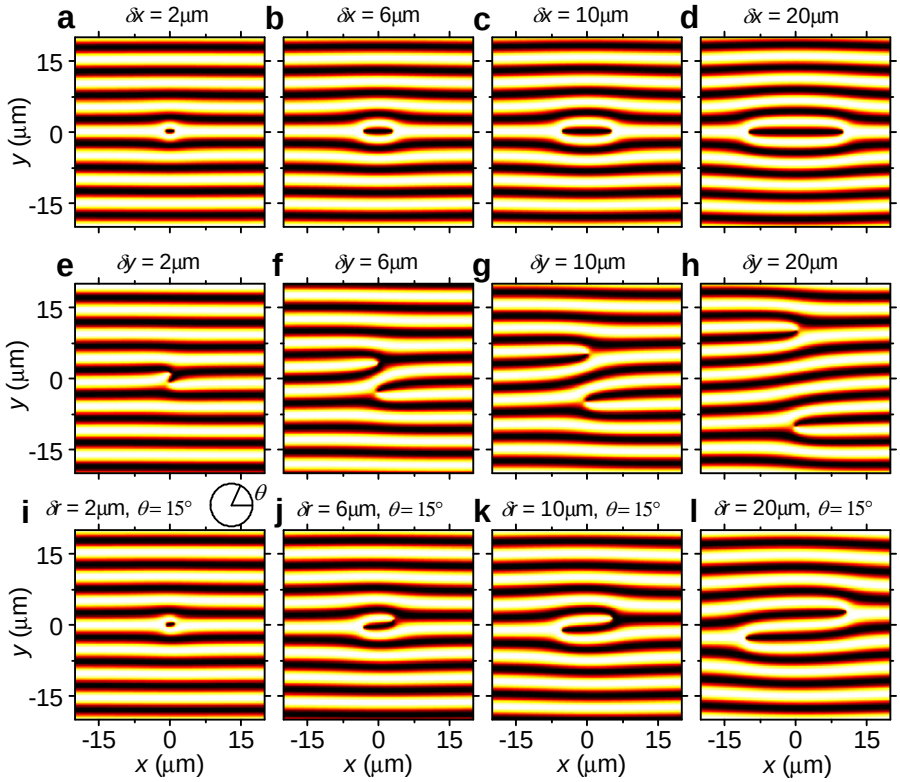

Figure 4.8: Simulations of interference pattern in the shift-interferometry experiments for a quantized vortex of excitons. The shifts are along x (a-d), y (e-h), and at 15^0 to x (i-l). A quantized vortex is characterized by a pair of opposite forks separated by the distance equal to the shift in the shift-interferometry experiment

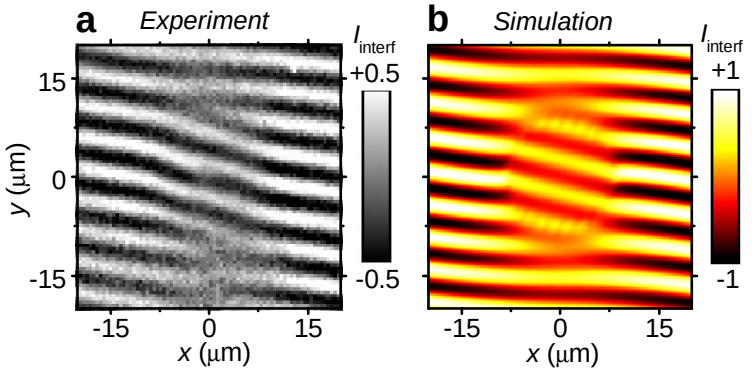

Figure 4.9: Simulated interference patterns for a ring shaped source of excitons. (a) Measured interference pattern. (b) Simulations of interference pattern in the shift-interferometry experiments for excitons produced by 24 point sources distributed along the 8-μm radius ring. $\delta x = 2\,\mu$m in (a) and (b).

shaped source result in the interference pattern with opposite forks separated by a distance much larger than δx, in qualitative agreement with the experiment (Fig. 4.9). The simulations also show a higher coherence outside the ring region and a higher coherence along the direction of the shift $\delta\mathbf{x}$.

In the experiment, the exciton source is a ring, therefore, it is reasonable to assume that the exciton source is a ring as it is done in the simulations. In the experiment, there is heating of the exciton gas in the source due to the binding energy released at the exciton formation, therefore, it is reasonable to assume that the separated point sources on the ring are mutually incoherent as it is done in the simulations.

Simulations of the interference pattern produced by a ring-shaped source, such as an LBS ring, result in the interference pattern with opposite forks separated by a distance much larger than δx, in qualitative agreement with the experiment. A ring-shaped source with particles propagating away from their origin on the ring produces a more complicated phase pattern than a vortex, yet both objects are characterized by the spreading of particle velocities over all directions. The observed phase singularities constitute the properties of a quantum exciton gas with extended spontaneous coherence (Fig. 4.7a) and no such phase singularity is observed at high temperatures in a classical gas (Fig. 4.7d).

4.4 Spin texture in a cold exciton gas

Spin ordering forms the basis for a number of fundamental effects in physics. Macroscopic spin ordering with neighboring spins parallel or antiparallel to each other is responsible for ferromagnetism and antiferromagnetism. More complex spin structures, also known as spin textures, determine the physical properties of exotic states of matter and are currently under intense investigation. Those spin structures include skyrmion spin textures in quantum Hall ferromagnets [Girvin, 2000] and graphene [Fertig & Brey, 2007], ferromagnetic domains and spin vortices in atom Bose-Einstein condensates [Sadler *et al.*, 2006], skyrmion lattices in chiral magnets [Muehlbauer *et al.*, 2009; Yu *et al.*,

2010], and half-vortices in He3 [Salomaa & Volovik, 1987] and polariton condensates [Lagoudakis *et al.*, 2009]. Spin textures are also characteristic of topological insulators [Qi & Zhang, 2010].

Indirect excitons in CQW are characterized by properties which are essential for the observation of spin textures: (i) Long lifetimes of indirect excitons allow them to cool to low temperatures within about 0.1 K of the lattice temperature, which can be lowered to well below 1 K in a dilution refrigerator. This allows the realization of a cold exciton gas with temperature well below the temperature of quantum degeneracy, which is in the range of a few Kelvin for typical exciton densities $\sim 10^{10}$ cm^{-2} for the studied GaAs/AlGaAs CQW [Butov *et al.*, 2001]. (ii) Long lifetimes of indirect excitons allow them to travel over large distances before recombination [Hagn *et al.*, 1995; Larionov *et al.*, 2000; Butov *et al.*, 2002; Gärtner *et al.*, 2006; Ivanov *et al.*, 2006]. (iii) The exciton spin relaxation induced by the electron-hole exchange interaction is strongly suppressed for indirect excitons with small electron-hole overlap and, as a result, spin relaxation times of indirect excitons can be orders of magnitude longer than those of regular excitons [Vinattieri *et al.*, 1994; Larionov & Golub, 2008; Leonard *et al.*, 2009; Kowalik-Seidl *et al.*, 2010].

In the previous section, we demonstrated that a pattern of exciton spin was closely correlated with the pattern of coherence, compare Fig. 4.3c,d and g,h. In this section, we explore the observed spin texture in-depth.

4.4.1 Properties of the exciton spin texture

The spin texture is observed around the rings in the exciton emission pattern. Figure 4.10c shows a segment of the exciton pattern with a section of the external ring and smaller localized bright spot (LBS) rings. Figure 4.10d and 4.10e show the corresponding pattern of linear and circular polarization.

The observed phenomena are qualitatively similar for both exciton sources – the external ring and LBS ring, as is detailed below. An LBS ring is close to a model radially symmetric source of excitons; therefore, we first discuss the features of the spin texture around the LBS. All LBS rings in the emission pattern

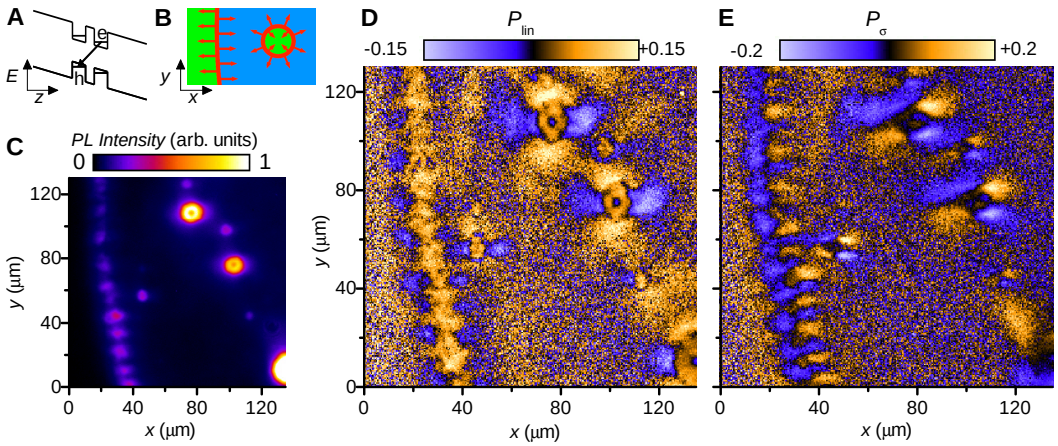

Figure 4.10: Spin texture in a cold exciton gas. (a) Energy-band diagram of the CQW; e, electron; h, hole. (b) Schematic of exciton formation in the exciton rings; Excitons (red) form on the boundary of hole-rich (blue) and electron-rich (green) areas. (c) A segment of the emission pattern of indirect excitons showing the external ring (left) and multiple Localized Bright Spots (LBSs). (d,e) (d) Pattern of linear polarization $P_{lin} = (I_x - I_y)/(I_x + I_y)$ and (e) pattern of circular polarization $P_\sigma = (I_{\sigma^+} - I_{\sigma^-})/(I_{\sigma^+} + I_{\sigma^-})$ of the emission of indirect excitons in the region of (C) at $T_{bath} = 0.1$ K

show similar spin textures. The observed phenomena are listed below.

1. A ring of linear polarization is observed around the LBS center (Fig. 4.10d, 4.11a). Measurements with a rotating polarizer confirm polarization along the x-direction. The ring radius, where the linear polarization is maximum, is about 3μm. The ring of linear polarization vanishes with increasing temperature (Fig. 4.11b).

2. A vortex of linear polarization is observed around the LBS center (Fig. 4.10d, 4.11a). Figures 4.10d, 4.11a show that y-polarization is observed along x-direction and x-polarization is observed along y-direction. Measurements with a rotating polarizer confirm that the polarization is perpendicular to the radial direction for all azimuthal angles θ for the polarization vortex. The polarization vortex is observed in the range of distances from the LBS center $3 \lesssim r \lesssim 20\mu$m (Fig. 4.10d, 4.11a). The ring of linear polarization and polarization vortex overlap at $r = 3 - 5\mu$m forming a more complex spin texture. The polarization vortex vanishes with increasing temperature (Fig. 4.11b,d).

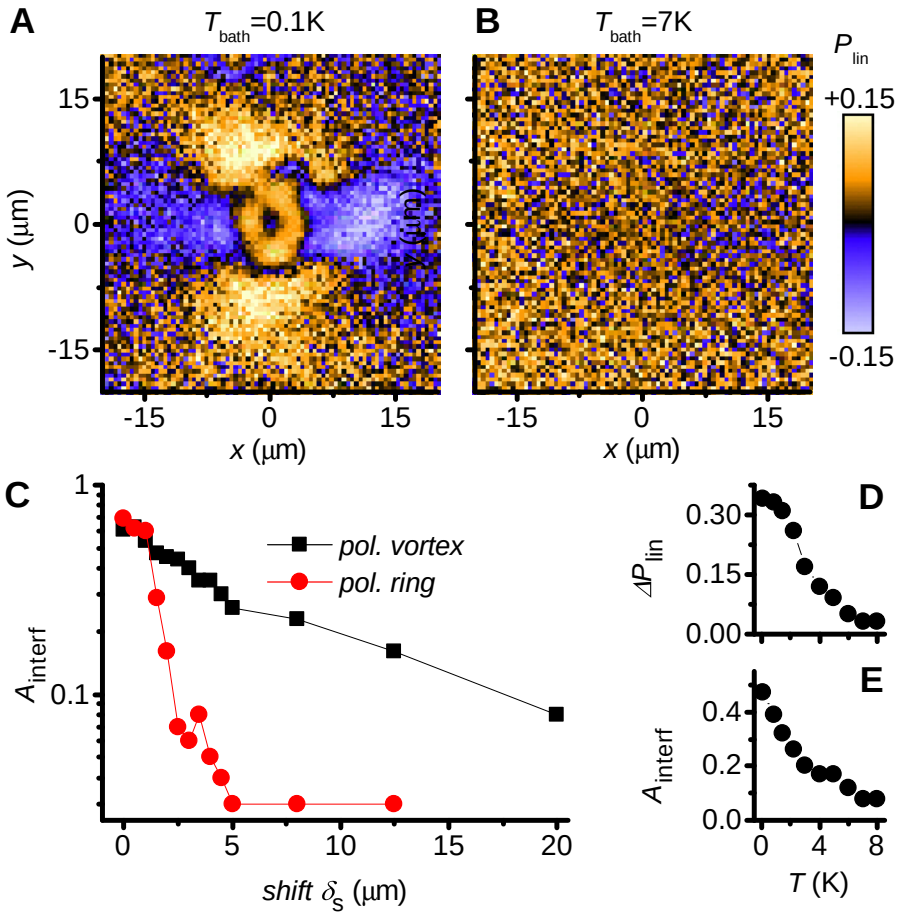

Figure 4.11: Spin texture: Linear polarization. (a,b) Measured linear polarization of the emission of indirect excitons $P_{lin} = (I_x - I_y)/(I_x + I_y)$ around the LBS centered at (105,75), fig.1c, at (a) T_{bath} = 0.1 K and (B) T_{bath} = 7 K (c) Exciton coherence measured by shift-interferometry: Interference visibility A_{interf} vs. shift δ_s for the vortex of linear polarization (squares), 18μm left of LBS center, and the polarization ring (points), 2μm left of LBS center. The LBS is centered at (80,105), fig.1c. T_{bath} = 0.1 K. (d,e) Emergence of the vortex of linear polarization and extended coherence at low temperatures: (d) The amplitude of azimuthal variation of P_{lin}, ΔP_θ, at r = 10μm and (e) interference visibility A_{interf} in the polarization vortex for δ_s = 2μm vs. temperature.

3. The flux of excitons from the LBS origin is anisotropic (Fig. 4.12a): The emission intensity is enhanced along the x-axis, the polarization direction in the polarization ring. The exciton flux anisotropy vanishes with increasing temperature (Fig. 4.13c) so the exciton flux from the LBS origin is isotropic at high temperatures.

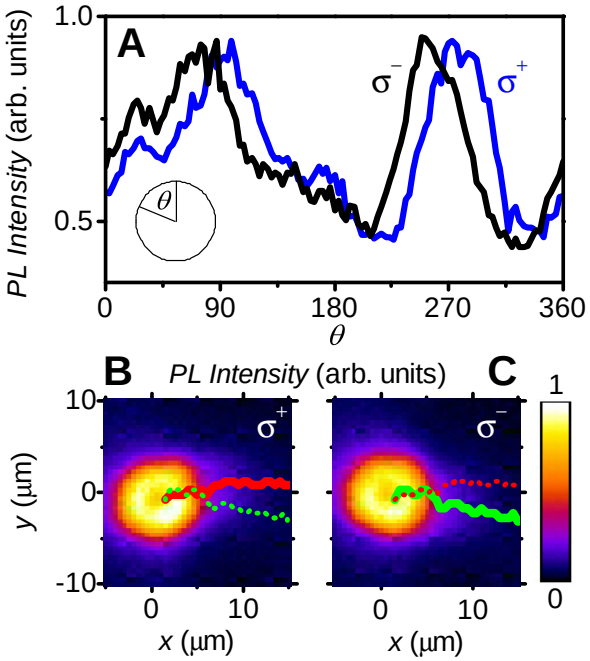

Figure 4.12: Anisotropy of exciton flux and skew between circular polarizations. (a) Azimuthal variation of the emission intensity of indirect excitons at $r = 8\mu$m in σ^+ (blue) and σ^- (black) polarizations. Angles are measured from the y-axis. (b,c) Traces of the σ^+ (red) and σ^- (green) emission peak around $\theta = 270°$ [see (A)]; The emission image in (b) σ^+ and (c) σ^- polarization is also shown.

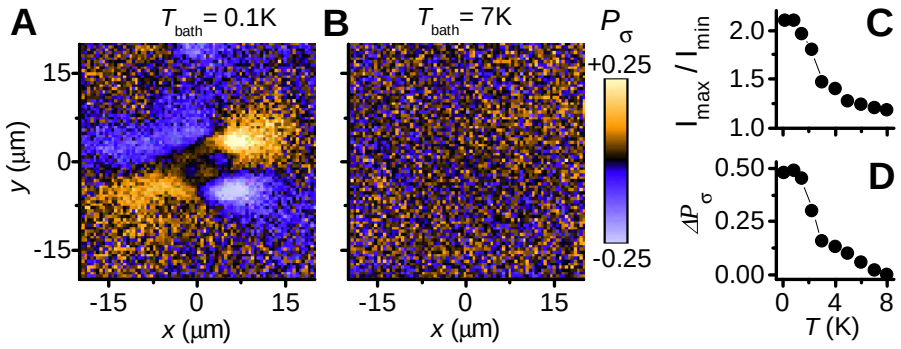

Figure 4.13: Spin texture: Circular polarization. (a,b) Measured circular polarization of the emission of indirect excitons $P_\sigma = (I_{\sigma^+} - I_{\sigma^-})/(I_{\sigma^+} + I_{\sigma^-})$ around LBS at (a) $T_{bath} = 0.1$ K and (b) $T_{bath} = 7$ K (c) The ratio of maximum to minimum in the azimuthal variation of the total emission intensity of indirect excitons I_{max}/I_{min} at $r = 8\mu$m vs. temperature. (d) The amplitude of variation of P_σ around the LBS centered at (105,75), Fig. 4.10c, vs. temperature.

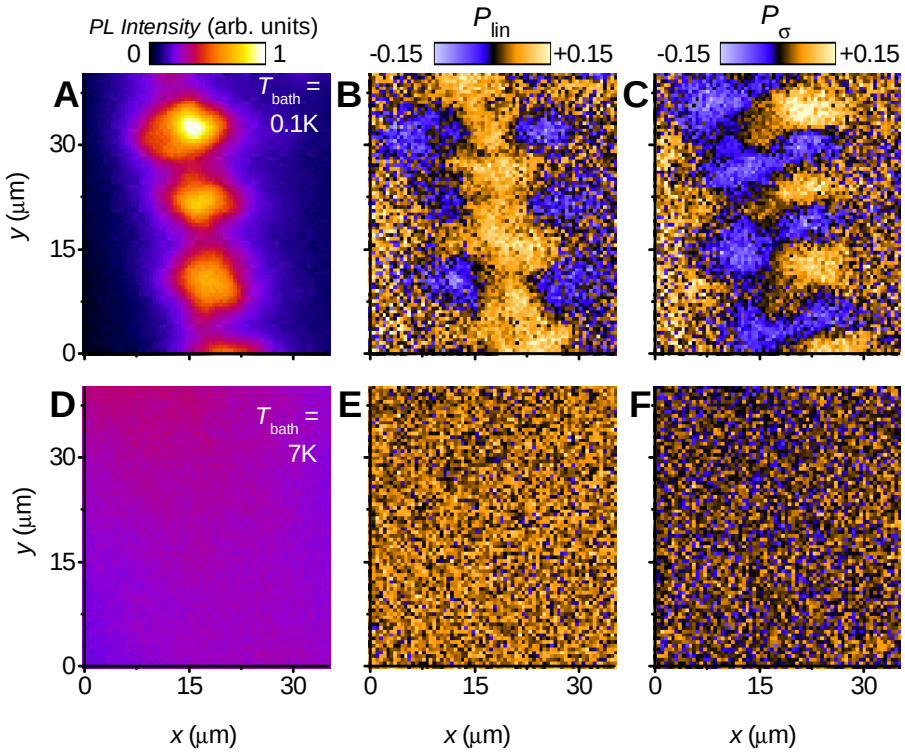

Figure 4.14: Spin texture around external ring. (a,d) Emission of indirect excitons in the external ring region. (b,d,e,f) Pattern of linear (b,e) and circular (c,f) polarization around the external ring at T_{bath} = 0.1 K (a-c) and T_{bath} = 7 K (d-f).

4. A skew of the exciton fluxes in orthogonal circular polarizations (Fig. 4.12a-c) and a corresponding four-leaf pattern of circular polarization (Fig. 4.10e,4.13a) is observed around the LBS. The skew of the exciton flux is observed in the range of distances from the LBS center $5 \lesssim r \lesssim 15\mu$m (Fig. 4.12b,c). The corresponding four-leaf pattern of circular polarization vanishes with increasing temperature (Fig. 4.13b,d).

5. Similar polarization textures are observed in the external ring region (Fig. 4.14). At low temperatures, the macroscopically ordered exciton state (MOES) characterized by a spatially ordered array of higher-density beads [Butov *et al.*, 2002] and a large exciton coherence length [Yang *et al.*, 2006] forms in the external ring. The polarization texture in the external ring region appears as the superposition of the polarization textures produced by the MOES beads with each being similar to the texture produced by an LBS (compare Fig. 4.14b

with Fig. 4.11a and Fig. 4.14c with Fig. 4.13e). A periodic array of beads in the MOES (Fig. 4.14a) creates a periodic polarization texture (Fig. 4.14b,c). The fragmentation of the external ring and the spin texture in the region of the external ring vanish with increasing temperature (Fig. 4.14d-f). Both the position of the external ring and the wavelength of the exciton density wave are controlled by the laser excitation indicating that the exciton density modulation in the MOES is not governed by disorder in the sample. The presence of spin texture in the external ring region confirms that the spin texture does not arise due to a local defect structure.

6. As mentioned in the previous section, an extended exciton coherence with a large coherence length ξ is observed in the region of the polarization vortex (Fig. 4.11c). In contrast, ξ is short in the region of the polarization ring, which is close to the hot LBS center. With reducing temperature, the exciton spin textures emerge in concert with coherence (Fig. 4.11d,e).

4.4.2 Modeling of spin texture

Below, we briefly discuss the observed phenomena and consider a model which can lead to the appearance of an exciton spin texture. This model is based on ballistic exciton transport and precession of spins of electrons and holes. The heavy hole excitons in GaAs QWs may have four spin projections on the structure axis: $-2, -1, +1, +2$. The spin states -1 and $+1$ are optically active and contribute to left- and right-circularly polarized emission, while the states -2 and $+2$ are so called dark excitons which are optically inactive [Maialle *et al.*, 1993; de Andrada e Silva, 1997; Wu & Shem, 2008]. The splitting of linearly polarized exciton states originates from in-plane anisotropy induced by the crystallographic axis orientation and strain. The precession of spins of electrons and holes moving in the QW plane originates from this splitting and spin-orbit interaction which is described by a Dresselhaus Hamiltonian $H_e = \beta_e \left(k_x^e \sigma_x - k_y^e \sigma_y\right)$ for electrons and $H_h = \beta_h \left(k_x^h \sigma_x + k_y^h \sigma_y\right)$ for holes [Luo *et al.*, 2010], where $\mathbf{k}_{e,h}$ are electron and hole wave-vectors, $\beta_{e,h}$ are constants, and $\sigma_{x,y}$ are Pauli matrices.

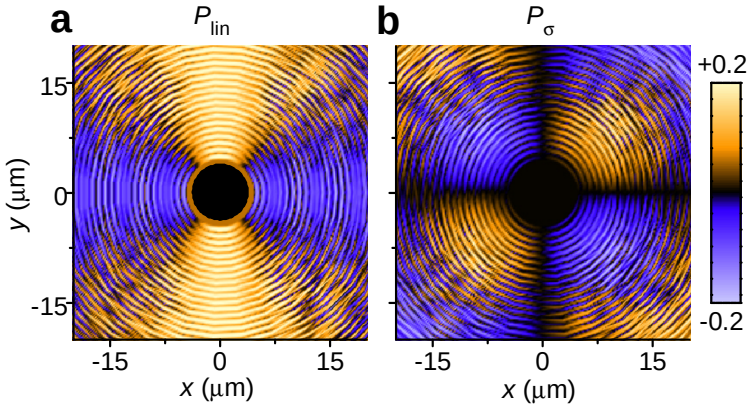

Figure 4.15: Simulation of spin texture around localized bright spots. (a,b) Simulated (a) pattern of linear polarization, and (b) pattern of circular polarization around LBS. The LBS center is in the origin. The black region in the center refers to a hot exciton gas, which is not considered in the simulations.

The appearance of an exciton spin texture within this model is outlined below. Details are presented in the Appendix.

A ring of linear polarization: The splitting between the linearly polarized exciton states leads to linear polarization of the exciton gas at thermal equilibrium. Heating of the exciton gas at the origin reduces the polarization degree in the center and, as a result, leads to the appearance of a ring of linear polarization.

A vortex of linear polarization: Spin-orbit coupling provides two channels for conversion of bright to dark excitons and vice versa with the phase gained by excitons during such conversion dependent on their propagation direction. This results in populating the exciton states whose polarization is normal to the wave vector and, in turn, the appearance of a vortex of linear polarization.

A four-leaf pattern of circular polarization: The beats between orthogonal linearly polarized exciton states lead to the appearance of a four-leaf pattern of circular polarization in a qualitative similarity to the optical spin Hall effect [Leyder *et al.*, 2007]. The appearance of a vortex of linear polarization and four-leaf pattern of circular polarization within the model rely on ballistic propagation of excitons with coherent spin precession.

4.4.3 Discussion

A ring of linear polarization: The current filament forms a heating source at the LBS center while no such local heating source is present in the external ring [Butov, 2004], consistent with the ring of linear polarization in the LBS area and its absence in the external ring area (Fig. 4.11a and 4.14b).

A vortex of linear polarization: The appearance of this spin texture indicates a transport regime where the spin polarization is locked to the direction of particle propagation, scattering is suppressed, and the mean free path is dramatically enhanced. Indeed, the vortex of linear polarization indicates that the exciton polarization is perpendicular to the direction of exciton propagation from the origin. The observation of the polarization vortex up to $\sim 20\mu$m away from the origin (Fig. 4.10d,4.11a) indicates that the exciton propagation direction is maintained over this distance. Such propagation requires suppression of exciton scattering on disorder. In comparison, for a classical exciton transport even with a very high diffusion coefficient $D = 100$ cm^2/s, the exciton mean free path is only $\sim 1\mu$m so maintaining polarization normal to the direction to the origin over $\sim 20\mu$m is unlikely due to multiple collisions.

Extended coherence: The suppression of exciton scattering in the region of the polarization vortex is evidenced by extended exciton coherence with a large coherence length $\xi \sim 8\mu$m (Fig. 4.11c). In comparison, for a classical exciton gas, ξ_{cl} is close to the thermal de Broglie wavelength, which scales $\propto T^{-1/2}$ and is about 0.5μm at 0.1 K. Large $\xi \gg \xi_{cl}$ in the region of the polarization vortex indicates a coherent exciton state with a much narrower than classical exciton distribution in momentum space, characteristic of a condensate.

4.5 Acknowledgements

The text of chapter 4, in part, is a reprint of the material as it appears in A.A. High, J.R. Leonard, A.T. Hammack, M.M. Fogler, L.V. Butov, A.V. Kavokin, K.L. Campman & A.C. Gossard, *Spontaneous coherence in a cold exciton gas*, Nature 483, 584 (2012), ©Nature Publishing Group, where the dissertation author was

the first author. The co-authors in this publication directed, supervised, and co-worked on the research which forms the basis of this chapter.

The text of chapter 4, in part, is a reprint of the material as it appears in A.A. High, A.T. Hammack, J.R. Leonard, Sen Yang, L.V. Butov, T. Ostatnicky, A.V. Kavokin & A.C. Gossard, *Spin texture in a cold exciton gas*, arXiv:1103.0321, where the dissertation author was the first author. The co-authors in this publication directed, supervised, and co-worked on the research which forms the basis of this chapter.

Chapter 5

Condensation of excitons in a trap

The confinement of atomic vapors in traps has led to the realization of Bose-Einstein condensation of atoms [Anderson *et al.*, 1995; Bradley *et al.*, 1995; Davis *et al.*, 1995]. Condensation is equivalent to the emergence of spontaneous coherence of matter waves [Penrose & Onsager, 1956]. The detection of spontaneous coherence is a direct experimental measurement of condensation. The bosonic nature of excitons allows for their condensation at low temperatures, as discussed in chapter 1 [Keldysh & Kozlov, 1968].

Excitons have been studied in a variety of traps, including electrostatic traps [Huber *et al.*, 1998; Hammack *et al.*, 2006a; Chen *et al.*, 2006; Gorbunov & Timofeev, 2006; High *et al.*, 2009a,b; Schinner *et al.*, 2011], strain-induced traps [Trauernicht *et al.*, 1983; Kash *et al.*, 1988; Naka & Nagasawa, 2005; Yoshioka *et al.*, 2011], traps created by laser-induced interdiffusion [Brunner *et al.*, 1992], magnetic traps [Christianen *et al.*, 1998], and laser-induced traps [Alloing *et al.*, 2012; Hammack *et al.*, 2006b]. However, in spite of intensive studies, no emergence of spontaneous coherence of excitons in a trap was observed until present. Spontaneous coherence of excitons was probed in a ring-shaped trap [Gorbunov & Timofeev, 2006], however, no enhancement of the interference contrast, and, in turn, the degree of first-order coherence with lowering temperature was shown. Spontaneous coherence of excitons was also probed in a different system - the exciton rings [Yang *et al.*, 2006; Fogler *et al.*, 2008; High *et al.*, 2012]. These measurements are discussed in chapter 4. The ring forms on the interface between

the electron-rich and hole-rich regions and lacks the crucial advantage of traps - the opportunity to control the condensates.

In this chapter, we report on the observation of condensation and spontaneous coherence in a gas of indirect exciton confined in an electrostatic trap. Imaging and interferometric measurements detect that excitons condense at the trap bottom and exciton spontaneous coherence emerges with lowering temperature. Below a temperature of about 1 K, the direct signature of Bose-Einstein condensation - the extension of coherence over the entire cloud - is observed.

5.1 Experimental Setup

In this section we will discuss the trapping method and experimental characterization of the interferometer.

5.1.1 Remote excitation of the diamond trap

We realize an electrostatic trap for indirect excitons using a diamond-shaped electrode (Fig. 5.1b). Since a thinner electrode produces a smaller F_z due to field divergence near the electrode edges the diamond trap creates a confining potential with the exciton energy gradually reducing towards the trap center (Fig. 5.1c,d) [High *et al.*, 2009b]. Details on the diamond trap are presented in chapter 3.

The excitons are photoexcited by a 633 nm HeNe laser. The excitation beam is focused to a spot about 5μm in diameter on a side of the trap (Fig. 5.1b,c). This excitation scheme allows further cooling of the photoexcited excitons when they travel towards the trap center, thus facilitating the realization of a cold exciton gas in the trap (cooling of excitons away from the laser excitation spot also leads to the realization of a cold exciton gas in the inner ring in exciton emission pattern and in laser-induced traps [Hammack *et al.*, 2006b]).

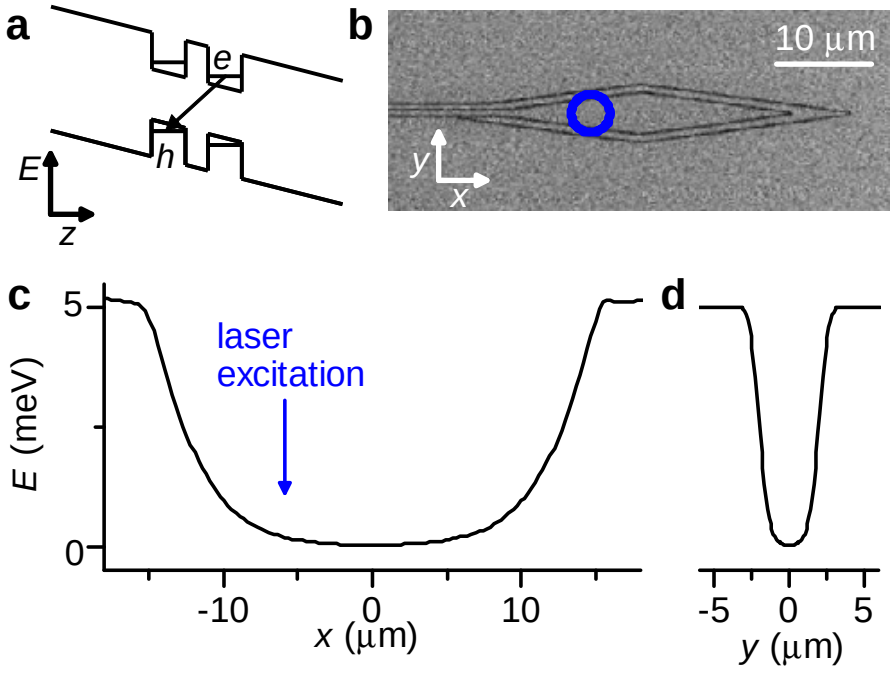

Figure 5.1: Schematic for remote excitation in the diamond trap. (a) Energy-band diagram of the CQW structure. e, electron; h, hole. (b) SEM image of electrodes forming the diamond trap: A diamond-shaped electrode is surrounded by a thin wire electrode followed by an outer plane electrode. (c,d) Simulation of exciton energy profile through the trap center along x (c) and y (d) for $V_{diamond} = -2.5$ V, $V_{wire} = -2$ V, and $V_{plane} = -2$ V. The position of the laser excitation spot is indicated by the circle in (b) and by the arrow in (c).

5.1.2 Interferometric Setup

The first-order coherence function $g_1(\delta x)$ is measured by shift-interferometry: The emission images produced by arm 1 and 2 of the Mach-Zehnder interferometer (Fig. 5.2a) are shifted with respect to each other to measure the interference between the emission of indirect excitons spatially separated by δx. We measure emission intensity I_1 for arm 1 open, I_2 for arm 2 open, and I_{12} for both arms open, and calculate $I_{\text{interf}} = (I_{12} - I_1 - I_2)/(2\sqrt{I_1 I_2})$ (Fig. 5.2b-e). $g_1(\delta x)$ is given by the amplitude of the interference fringes in I_{interf}. Fig. 5.3 shows I_1, I_2,and I_{12} for $\delta x = 0\mu$m, $\delta x = 4\mu$m, and $\delta x = 6\mu$m.

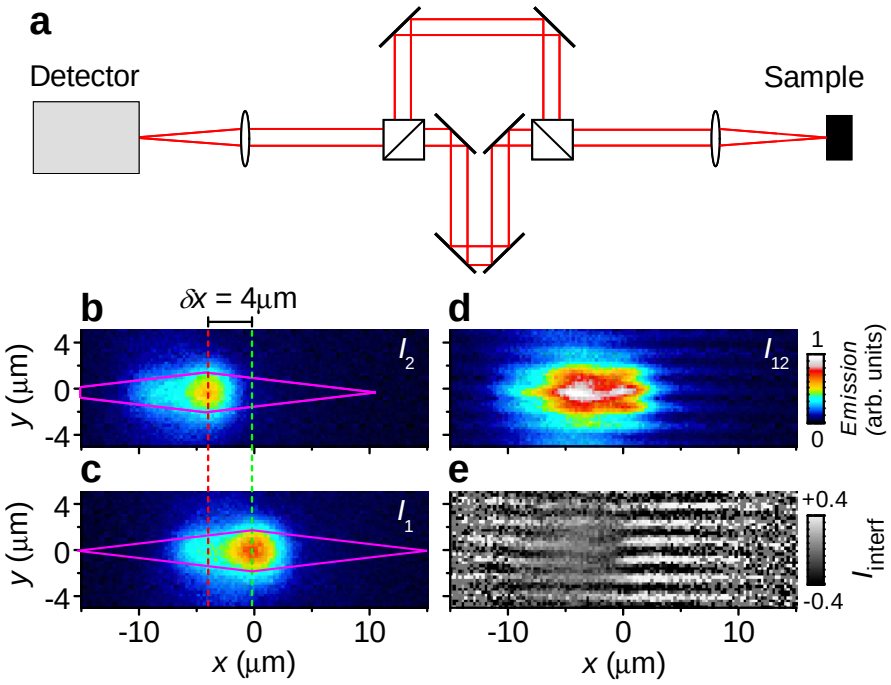

Figure 5.2: Method of interference measurements to measure coherence in the trap. (a) Schematic of the interferometric setup. (b-d) Emission image of indirect excitons measured with arm 2 open (b), arm 1 open (c), and both arms open (d). T_{bath} = 0.1 K, P_{ex} = 1.9 μW. (e) I_{interf} obtained from (b-d).

5.1.3 Emission Spectra and Fourier spectroscopy measurements

Figure 5.4a presents the spectra at low and high temperature measured by spectrometer. In all interference and imaging experiments in this chapter, only the emission of indirect excitons (IX) is measured. This is achieved by using an interference filter. The transmission curve of the interference filter is presented in Fig. 5.4a. This curve shows that the contribution of the weak emission of direct excitons (DX) or any other emission (such as low-energy bulk emission) has been cut off by the interference filter. Therefore, any change of the amplitude of the interference fringes $A_{interf}(\delta x)$ and, in turn, the coherence length measured in our experiments is due to a change of coherence of indirect excitons.

We also measured amplitude of interference fringes A_{interf} vs. the difference in the path lengths of arm 1 and arm 2 of the MZ interferometer δz and corresponding time delay δt for indirect excitons in the center of the trap

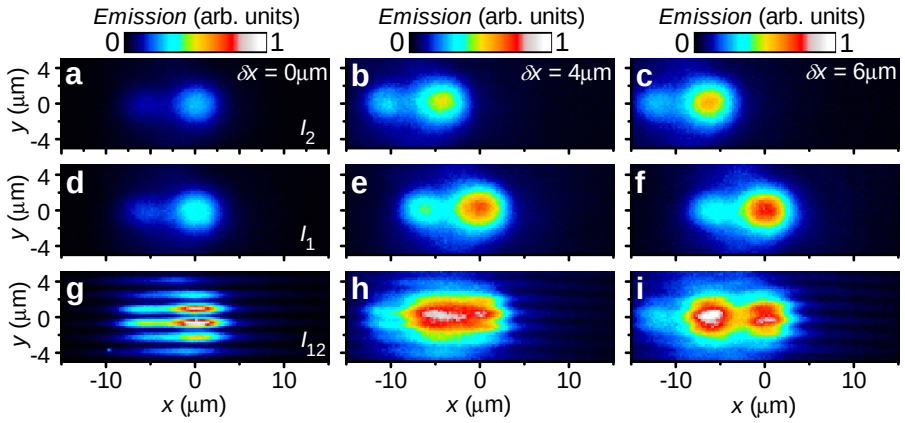

Figure 5.3: Emission images for different interferometer offsets δx: Emission images I_2 for arm 2 open (a-c), emission images I_1 for arm 1 open (d-f), and interference images I_{12} for both arms open (g-i) for shift $\delta x = 0$ (a,d,g), 4 μm (b,e,h), and 6 μm (c,f,i). $T_{bath} = 0.1$ K, $P_{ex} = 2.2\,\mu$W.

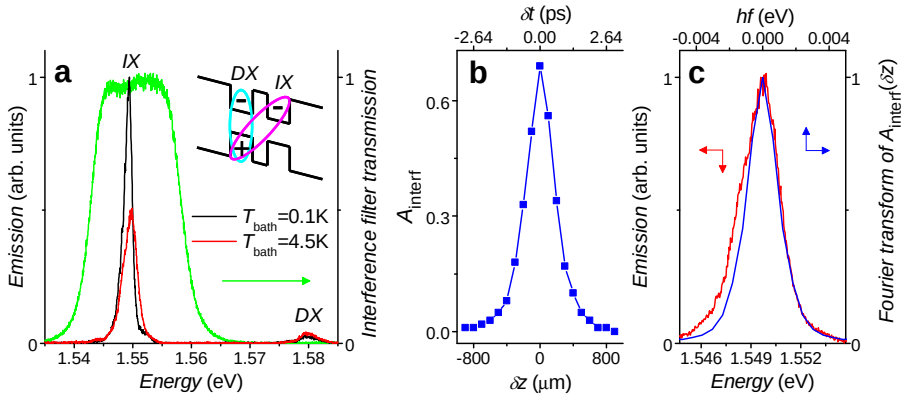

Figure 5.4: Characterization of interferometer: Emission spectra and Fourier spectroscopy measurements. (a) Emission spectra in the center of the trap for $T_{bath} = 0.1$ K (black line) and 4.5 K (red line) measured by spectrometer. Emission of direct excitons (DX) and indirect excitons (IX) is indicated. Green line presents the transmission curve of the interference filter used in the shift-interferometry, Fourier-spectroscopy, and imaging experiments. Inset: Band diagram of the CQW with direct and indirect excitons. (b) Fourier-spectroscopy measurements: Amplitude of interference fringes A_{interf} vs. the difference in the path lengths of arm 1 and arm 2 of the MZ interferometer δz and corresponding time delay δt for indirect excitons in the center of the trap at $T_{bath} = 4.5$ K. (c) Calculated spectrum based on Fourier transform of $A_{\text{interf}}(\delta t)$ in (b) (blue line) and spectrum of indirect excitons measured by spectrometer in the center of the trap at $T_{bath} = 4.5$ K (red line). $P_{ex} = 1.9\,\mu$W.

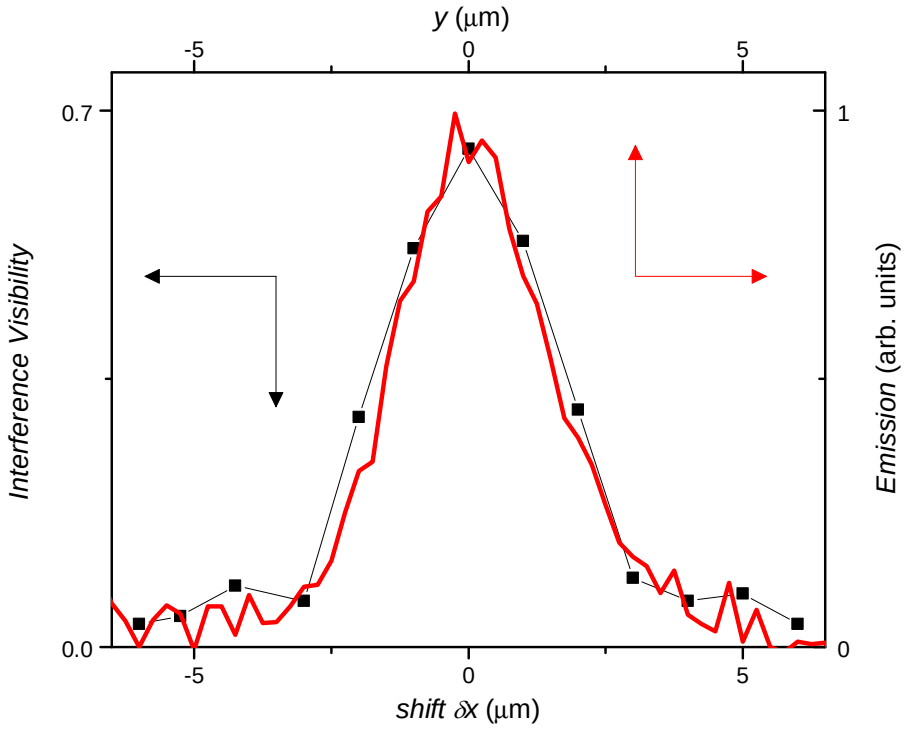

Figure 5.5: Comparison of interference visibility at high temperature and spatial resolution. Interference visibility vs. shift δx for excitons in trap at T_{bath} = 8 K (black squares) and y-axis cross section of exciton emission in a segment of the thin wire on the left from the diamond, see Fig. 5.1b (red line). The width of the wire, 0.6 μm, is significantly smaller than the spatial resolution and, therefore, the wire can be considered as a source of vanishing width.

(Fig. 5.4b). The spectrum obtained by this Fourier-spectroscopy measurement is in a good agreement with the spectrum measured by spectrometer (Fig. 5.4c).

5.1.4 Measurement of the point-spread function.

The point-spread function (PSF) of the optical setup is measured by exciting a segment of the thin wire on the left from the diamond (see Fig. 5.1b) and measuring the spatial profile of exciton emission across the wire (Fig. 5.5). The width of this wire is 0.6 μm, significantly smaller than the PSF width for our optical setup. Therefore, the wire can be considered as a source of vanishing width so the spatial profile of exciton emission across the wire is given by the PSF. This independent measure of the PSF is in good agreement with the $A_{interf}(\delta x)$

function at high temperatures $T \gtrsim 4$ K (Fig. 5.9) that is given by the PSF width.

5.2 Experimental observations

5.2.1 Observation of spontaneous coherence

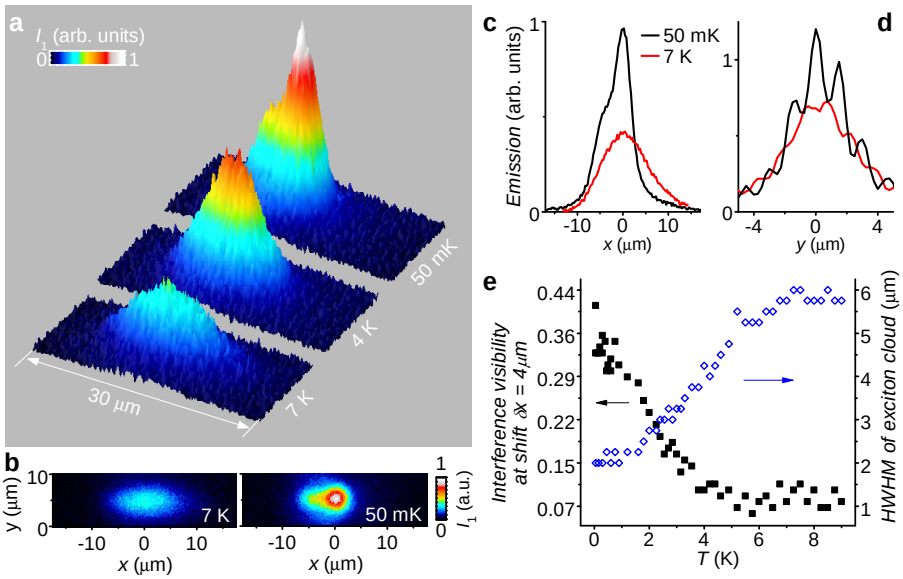

Figure 5.6: Observation of spontaneous coherence in the trap. (a,b) Emission patterns I_1 for temperatures $T_{\text{bath}} = 7$, 4, and 0.05 K. (c,d) Spatial profiles of the emission patterns (c) and interference patterns I_{12} at shift $\delta x = 4\,\mu$m (**d**) for $T_{\text{bath}} = 7$ K (red) and 0.05 K (black). (e) Amplitude of the interference fringes A_{interf} at shift $\delta x = 4\,\mu$m averaged over $0 < x < 1.5\,\mu$m (black squares) and half-width at half-maximum (HWHM) of the exciton emission pattern along x (blue diamonds) vs. temperature. $P_{ex} = 1.9\,\mu$W.

Figure 5.6 presents the temperature dependence of exciton emission and interference patterns. At high temperatures, the exciton cloud spreads over the trap resulting in a broad spatial profile of the exciton emission. With lowering temperature, excitons collect at the trap center (Fig. 5.6a,b,c,e). Studies of atoms in traps also show the collection of atoms at the trap center with lowering temperature due to the reduction of the thermal spreading of atoms over the trap and, eventually, condensation of atoms [Anderson *et al.*, 1995; Bradley *et al.*, 1995; Davis *et al.*, 1995].

To determine if condensation of excitons is realized in the trap, we performed shift-interferometry measurements. We found that the exciton collection at the trap center with lowering temperature is accompanied by a strong enhancement of the amplitude of the interference fringes A_{interf} for the interference between the emission of indirect excitons spatially separated by δx (Fig. 5.6d,e). Quantitative characteristics of spontaneous coherence and condensation can be obtained from the measurements of A_{interf} as a function of δx [Penrose & Onsager, 1956]. Such measurements are presented in the next sections.

5.2.2 Density dependence of g_1

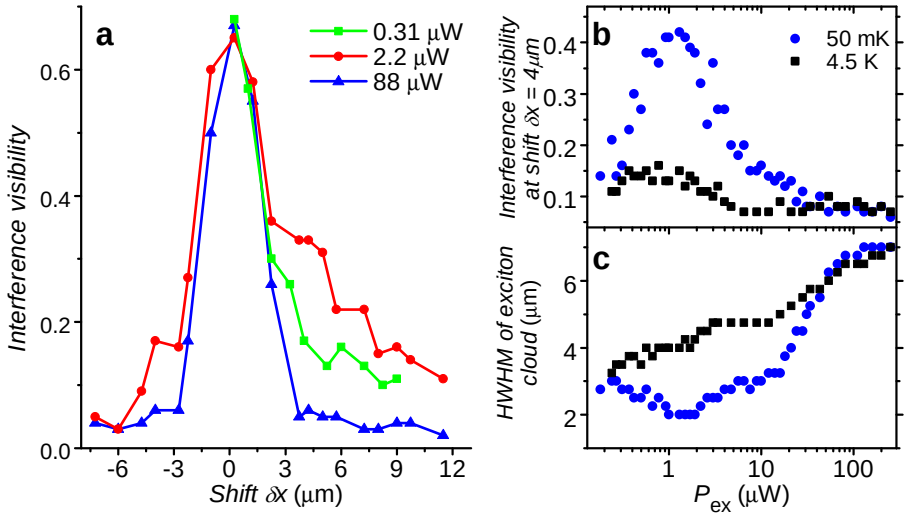

Figure 5.7: Density dependence of spontaneous coherence. (a) Amplitude of the interference fringes $A_{\text{interf}}(\delta x)$ for excitons in the trap for excitation density $P_{ex} = 0.31\,\mu$W (green squares), 2.2 μW (red circles), and 88 μW (blue triangles) at $T_{\text{bath}} = 50$ mK. (b,c) A_{interf} at shift $\delta x = 4\,\mu$m averaged over $0 < x < 1.5\,\mu$m (b) and HWHM of the exciton emission pattern along x (c) vs. P_{ex} for $T_{\text{bath}} = 50$ mK (blue circles) and 4.5 K (black squares).

Figure 5.7a presents $A_{\text{interf}}(\delta x)$ for different densities. The exciton temperature is higher in the excitation spot [Hammack *et al.*, 2006b]. This is consistent with low values of A_{interf} at negative δx, which correspond to the interference between the emission of a hot exciton gas in the excitation spot and exciton gas in the trap center. We consider positive δx, which correspond to the interference

between the emission of an exciton gas in the trap center and exciton gas at positive x further away from the hot excitation spot.

Figure 5.7c presents the density dependence of the width of the exciton emission pattern along x. At high temperature T_{bath} = 4.5 K, the width of the emission pattern of the exciton cloud monotonically increases with density. This is consistent with screening of the potential landscape in the trap by indirect excitons due to the repulsive exciton-exciton interaction [High *et al.*, 2009b]. However, a drastically different behavior is observed at low temperature T_{bath} = 50 mK: The increase of density leads to the reduction of the cloud width, indicating the exciton collection at the trap center. Only at the highest densities, the high-temperature behavior is recovered.

Figure 5.7b presents the density dependence of A_{interf}. At high temperature T_{bath} = 4.5 K, the coherence degree is low for all densities. However, at low temperature T_{bath} = 50 mK, the increase of density leads to a strong enhancement of A_{interf}, followed by its reduction. As in the case of varying temperature (Fig. 5.6e), with varying density, the exciton collection at the trap center is accompanied by the enhancement of the coherence degree of excitons (Fig. 5.7b,c).

5.2.3 Temperature dependence of g_1

The density, at which the coherence degree of excitons is close to maximum (Fig. 5.7b), has been chosen to study the temperature dependence due to the strongest coherence enhancement with reducing temperature. Figure 5.8 shows cross sections of intensity for different temperatures and offsets, along with the cross sections of I_{interf} from which $A_{\text{interf}}(\delta x)$ is calculated. Figure 5.9a presents the amplitude of the interference fringes $A_{\text{interf}}(\delta x)$ for different temperatures. The spatial extension of $A_{\text{interf}}(\delta x)$ can be characterized by a coherence length ξ at which the interference visibility drops e times. A strong enhancement of the exciton coherence length is observed at low temperatures (Fig. 5.9c). While at high temperatures ξ is considerably smaller than the exciton cloud width, at low temperatures the entire exciton cloud becomes coherent (Figs. 5.6e, 5.9).

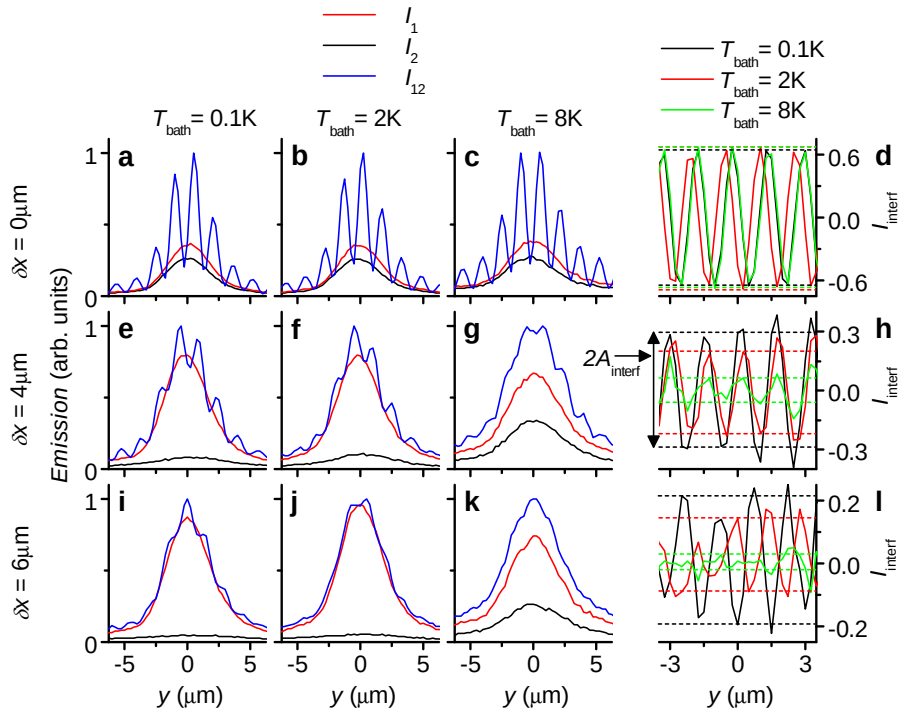

Figure 5.8: Spatial profiles of I_1,I_2, I_{12}, and I_{interf} at different offsets and temperatures. (a-c, e-g, i-k) Spatial profiles along y at $x = 0$ of I_1 (red), I_2 (black), and I_{12} (blue) at shift $\delta x = 0$ (a-c), 4 μm (e-g), and 6 μm (i-k). $T_{bath} = 0.1$ K (a,e,i), 2 K (b,f,j), and 8 K (c,g,k). (d,h,l) Spatial profiles along y at $x = 0$ of I_{interf} at $T_{bath} = 0.1$ K (black), 2 K (red), and 8 K (green) for $\delta x = 0$ (d), 4 μm (h), and 6 μm (l). Amplitudes of interference fringes A_{interf} are indicated by dashed lines. $P_{ex} = 1.9\mu$W.

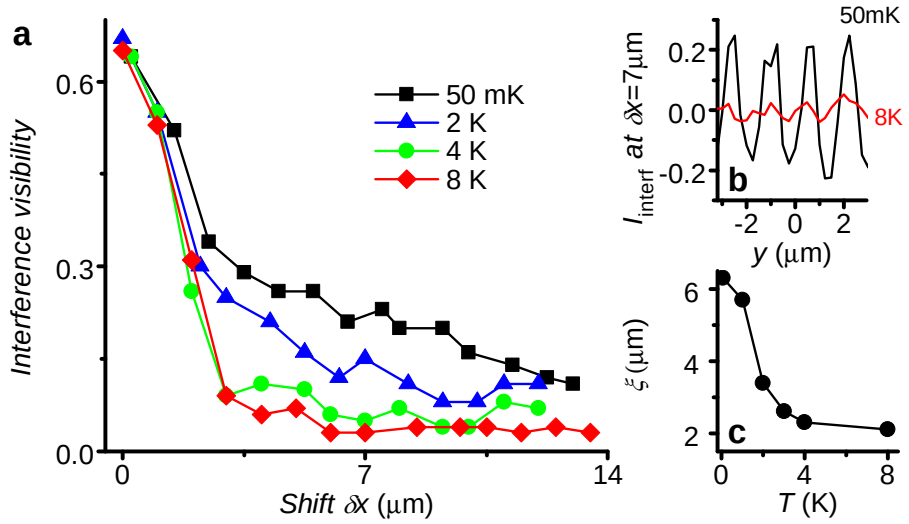

Figure 5.9: Measurements of the first order coherence function at different T. (a) $A_{\text{interf}}(\delta x)$ for excitons in the trap for $T_{\text{bath}} = 50\,\text{mK}$ (black squares), 2 K (blue triangles), 4 K (green circles), and 8 K (red diamonds). (b) I_{interf} for $T_{\text{bath}} = 50\,\text{mK}$ (black) and 8 K (red) at shift $\delta x = 7\,\mu$m. (c) The exciton coherence length ξ as a function of temperature. $P_{ex} = 1.9\,\mu$W.

5.3 Estimation of transition temperature

In this section, we estimate the temperature of Bose-Einstein condensation (BEC) of excitons in the trap and compare it with the measured condensation temperature. For a rough estimate, we use the formula for BEC in a system of ideal noninteracting bosons in a parabolic 2D trap [Ketterle & van Druten, 1996; Mullin, 1997; Dalfovo *et al.*, 1999]: $T_c = \frac{\sqrt{6}}{\pi}\hbar\omega_{2D}\sqrt{N/g}$, where $\omega_{2D} = (\omega_x\omega_y)^{1/2}$, ω_x and ω_y are the trap oscillator frequencies, g is the spin degeneracy, and N is the number of particles in the trap. A parabolic fit to the trap profile (Fig. 5.1c,d) $E(x,y) = \frac{m}{2}(\omega_x^2x^2 + \omega_y^2y^2)$ gives for $g = 4$ and exciton mass $m = 0.22m_0$ [Butov *et al.*, 2000]: $\omega_x \sim 4\times10^9\ \text{s}^{-1}$, $\omega_y \sim 3\times10^{10}\ \text{s}^{-1}$, and $T_c \sim 0.03\sqrt{N}$.

The exciton density n can be estimated from the energy shift. For the data in Fig. 5 at the lowest temperatures, the measured energy shift $\delta E \approx 1.3$ meV. Using the plate capacitor formula for the density estimate $\delta E = 4\pi e^2 nd/\varepsilon$ [Yoshioka & Macdonald, 1990; Zhu *et al.*, 1995; Ivanov, 2002], where $d \approx 12$ nm is the separation between the electron and hole layers for our sample and ε is the

background dielectric constant, gives $n \sim 10^{10}$ cm^{-2}. For the size of the exciton cloud in the trap ~ 10 μm^2 (Fig. 5.6), a total exciton number in the trap $N \sim 10^3$. This gives $T_c \sim 1$ K.

The plate capacitor formula underestimates the density [Schindler & R., 2008; Ivanov *et al.*, 2010]. Using the correction for the relation between δE and n estimated in [Remeika *et al.*, 2009], we obtain from the energy shift $N \sim 3 \times 10^3$ and $T_c \sim 2$ K. These rough estimates of the temperature of exciton BEC in the trap are close to the measured transition temperature ~ 2 K (Fig. 5.9c).

Note that the exciton density can be also roughly estimated from the light absorption: $n \sim \frac{P_{ex}}{E_{ex}A_{ex}}\alpha\tau$, where P_{ex} is the power of the excitation laser, E_{ex} is the photon energy of the excitation laser, A_{ex} is the excitation spot area, α is the fraction of photons emitted by the excitation laser that is transformed to indirect excitons due to the light absorption and carrier relaxation, and τ is the lifetime of indirect excitons. The uncertainty in the value of α makes such estimate rough. For $\alpha \sim 10^{-2}$, $P_{ex} \sim 2$ μW, $E_{ex} \sim 2$ eV, $A_{ex} \sim 10$ μm^2, and $\tau \sim 50$ ns, the estimate from the light absorption gives $n \sim 3 \times 10^{10}$ cm^{-2} and $N \sim 3 \times 10^3$.

5.4 Discussion

The data are discussed below. In the reported experiments, the laser excitation energy exceeds the exciton energy by about 400 meV and the laser excitation spot is spatially separated from the interfering excitons for positive δx. Therefore studied coherence in the exciton gas is spontaneous coherence; it is not induced by coherence of the laser excitation. [Note that for negative δx, the interfering excitons spatially overlap with the laser excitation spot and exciton coherence is suppressed (Fig. 5.7a), confirming that exciton coherence is not induced by the laser excitation.]

The coherence of an exciton gas is imprinted on the coherence of emission, which is described by the first-order coherence function $g_1(\delta x)$. In turn, this function is given by the amplitude of the interference fringes $A_{\text{interf}}(\delta x)$ in 'the ideal experiment' with perfect spatial resolution. In real experiments, the

measured $A_{\text{interf}}(\delta x)$ is given by the convolution of $g_1(\delta x)$ with the point-spread function (PSF) of the optical system used in the experiment [Fogler *et al.*, 2008]. The PSF is determined by measuring the emission profile across a source of vanishing width. The PSF is a peak at $\delta x = 0$ of the width corresponding to the spatial resolution of the optical system. A peak in $A_{\text{interf}}(\delta x)$ at $\delta x = 0$ due to the PSF can be seen both at low and high temperatures.

Both for a classical gas and quantum gas $g_1(\delta x)$ is close to 1 at $\delta x = 0$ and drops with increasing δx within the coherence length ξ. The difference between the classical and quantum gas is in the value of ξ. For a classical gas, ξ_{cl} is close to the thermal de Broglie wavelength $\lambda_{dB} = \sqrt{\frac{2\pi\hbar^2}{mT}}$, which is well below the PSF width in the studied temperature range ($\xi_{cl} < \xi_{cl@0.1K} \sim 0.5$ μm, the PSF width is ~ 2 μm). Therefore, for a classical gas at temperatures above 4 K, the measured ξ is given by the PSF width (Fig. 5.9).

For a classical gas, the coherence length $\xi \propto T^{-1/2}$ gradually increases with reducing temperature and remains small $< 0.5\mu$m for $T > 0.1K$, much smaller than the coherence length observed at the lowest temperatures (Fig.5.9). Therefore, an increase of the coherence length in a classical gas cannot lead to the increase in the contrast of the interference pattern at large δx observed in the experiment (Fig. 5.9).

In contrast, for a condensate, the coherence length becomes much larger than the thermal de Broglie wavelength and reaches the size of the exciton cloud in the trap so the entire exciton cloud becomes coherent. This signature of Bose-Einstein condensation is observed at the lowest temperatures in the experiment (Figs. 5.6e, 5.9). The measured transition temperature is $\sim$ 2 K (Fig. 5.9c), in good agreement with the estimate.

Finally, Fig. 5.9a also illustrates why $\delta x = 4\mu$m is selected for presenting coherence degree of excitons in Figs. 5.6 and 5.7. The shift $\delta x = 4$ μm exceeds both λ_{dB} and the PSF width. At such δx, only weak coherence given by the PSF value at $\delta x = 4$ μm can be observed for a classical gas. Higher A_{interf} exceeding such background level reveal spontaneous coherence of excitons.

The realization of exciton condensate in a trap opens the opportunity to

study the condensate properties. Traps allow precise control of condensates by in situ control of trap shape and depth that has been effectively used in studies of condensates of atoms. Similar control of condensates of excitons in condensed matter materials will allow studying condensates with parameters, such as mass, interaction, temperature, and characteristic times, orders of magnitude different from those in condensates of atoms. This will be the subject for future research.

5.5 Acknowledgements

The text of chapter 5, in part, is a reprint of the material as it appears in A.A. High, J.R. Leonard, M. Remeika, L.V. Butov, M. Hanson & A.C. Gossard, *Condensation of excitons in a trap*, Nano Letters 12, 2605 (2012), ©American Chemical Society, where the dissertation author was the first author. The co-authors in this publication directed, supervised, and co-worked on the research which forms the basis of this chapter.

Appendix A

Electronic behavior in crystals

In this appendix we will develop a basic understanding of the behavior of electrons in a crystal lattice. Lattices are formed by regular bonding between single or mixed-species atoms. This bonding is achieved through sharing of electrons in the outermost electronic orbitals of the atom. This allows us to distinguish between electrons that are tightly bound to the nucleus of the atom and electrons that are delocalized throughout the crystal structure. Since the delocalized electrons are no longer tightly bound to the nuclei, the cores of the nuclei develop a local positive charge. This local charge is attractive to the electron and results in the lattice potential. The presence of a lattice potential dramatically modifies the dynamics of electrons and holes (charge carriers) in the crystal. In particular, the lattice confines the allowed energy states of the carriers to bands, and gaps in energy can develop between bands. A full derivation of three-dimensional band structure is beyond this work and requires sophisticated mathematical methods. For an informative introduction to these methods please see *Solid State Physics* by Giuseppe Grosso and Giuseppe Pastori Parravicini. Here, we will only consider a simple one-dimensional model and show how energy bands can develop within a simple framework of Bragg scattering.

A.1 A simple one-dimensional model of electrons in a lattice

An electron in a one-dimensional potential $V(x)$ obeys the Schrödinger equation

$$-\frac{\hbar^2}{2m}\frac{d^2\psi(x)}{dx^2} + V(x)\psi(x) = \epsilon\psi(x). \tag{A.1}$$

We will consider a lattice potential $V(x)$ that satisfies the condition $V(x) = V(x + ma)$, where m is an arbitrary integer and a is the lattice constant. Since we are dealing with a regular, periodic structure it is useful to work in reciprocal space (with wavenumber k) rather than real space. The Fourier transform of a periodic potential $V(x)$ contains only plane waves with wavenumbers $G = 2\pi m/a$. We also take the Fourier transform of the wavefunction ψ, also with the condition that the electron wavefunction is periodic with the lattice, which implies $G - k = 2\pi l/a$, where l is an integer. Then,

$$V(\mathbf{x}) = \sum_{\mathbf{G}} V_{\mathbf{G}} e^{i\mathbf{G}\cdot\mathbf{x}}, \psi(\mathbf{x}) = \sum_{\mathbf{k}} C_{\mathbf{k}} e^{i\mathbf{k}\cdot\mathbf{x}}. \tag{A.2}$$

Substituting into the Schrödinger equation, we arrive at

$$\frac{\hbar^2}{2m}\sum_{\mathbf{k}} k^2 C_{\mathbf{k}} e^{i\mathbf{k}\mathbf{x}} + \sum_{\mathbf{k'}}\sum_{\mathbf{G}} C_{\mathbf{k'}} V_{\mathbf{G}} e^{i(\mathbf{k'}+\mathbf{G})\mathbf{x}} = \epsilon \sum_{\mathbf{k}} C_{\mathbf{k}} e^{i\mathbf{k}\mathbf{x}}. \tag{A.3}$$

In the summation variable, substitute $\mathbf{k'} = \mathbf{k} - \mathbf{G}$. Then by dividing out the sum over $\mathbf{k}$ we arrive at the eigenvalue equation

$$\left(\frac{\hbar^2}{2m} - \epsilon\right) C_{\mathbf{k}} + \sum_{\mathbf{G}} V_{\mathbf{G}} C_{\mathbf{k}-\mathbf{G}} = 0 \tag{A.4}$$

The eigenfunctions of this equation take the form

$$\psi_k(x) = e^{ikx} u_k(x), \tag{A.5}$$

where k is the wavenumber of the state and u_k is a periodic function where $u_k(x + ma) = u_k$. This is the Bloch theorem Bloch [1929]. Physically, the solutions of the Schrödinger equation take the form of traveling waves of wavenumber k where

the wave has some modulation on the lattice scale $u_k(x)$. Rather than consider electrons to be localized at some point in the lattice, we consider the electrons to be delocalized across the entire lattice with a well defined wavenumber. The n^{th} eigenvalues $\epsilon_n(k)$ and eigenvectors $\psi_n(k)$ of the Schrödinger equation are periodic functions of wavenumber with periodicity $\epsilon_n(k) = \epsilon_n(k + m2\pi/a)$, where $2\pi/a$ is also known as the periodicity of the reciprocal lattice. Due to this periodicity, the set of all unique electronic states in the system occur over the range $-\pi/a < k \leq \pi/a$, and can be specified by the wavenumber k and "band index" n.

The dynamics of an electron in a crystal are different from the dynamics of a free electron. A free electron has a wave function of the form $(1/\sqrt{L})e^{ikx}$, with eigenvalues of the momentum operator $p = -i\hbar\frac{d}{dx}$ given by $\hbar k$. By inspection, a Bloch function is not an eigenfunction of the momentum operator. Rather, $\hbar k$ of an electron in a crystal is referred to as the *quasi-momentum*. It can also be shown that the velocity of an electron in a crystal is related to the energy gradient by

$$v(k) = \frac{1}{\hbar}\frac{dE(k)}{dk}. \tag{A.6}$$

and the effective mass $m*$ of an electron in a crystal (how it responds to an external force) can be defined as

$$\frac{1}{m*} = \frac{1}{\hbar^2}\frac{d^2E(k)}{dk^2} \tag{A.7}$$

Grosso & Parravicini [2000]. Therefore, the effective mass and velocity of an electron in a given momentum and energy state is related to the local curvature of the band. The effective mass can differ significantly from the electron mass in a vacuum m_0.

A.2 Gaps in the dispersion relationship

Now we will show how gaps between energy bands can arise in a one-dimensional lattice. Consider a point in the nearly free electron model where there is a crossing between two energy bands, Fig. A.1. We will use degenerate

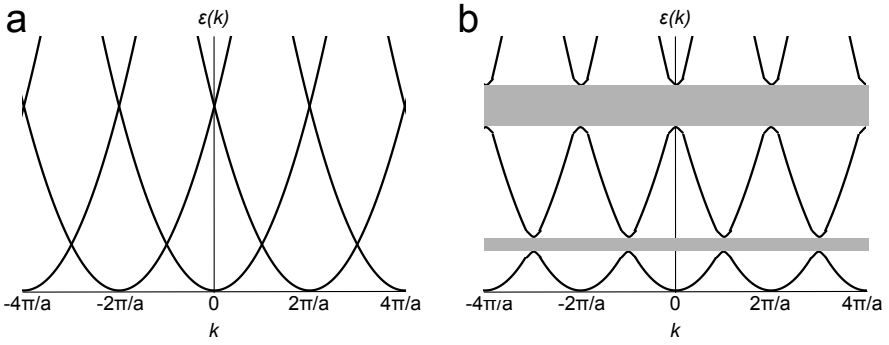

Figure A.1: Band structure of nearly-free electron in (a) the limit $V_{lattice} \rightarrow 0$ and (b) with a small lattice amplitude. The presence of a lattice potential opens energy gaps indicated by grey.

perturbation theory to explore what happens to the band crossing at the edge of the Brillouin zone $k = pi/a$ when a small lattice potential $V(x)$ is introduced. Let

$$\epsilon_0 = \frac{\hbar^2(\pi/a)^2}{2m}, \psi_1 = e^{ikx}, \psi_2 = e^{-ikx}. \tag{A.8}$$

We need to solve the matrix equation

$$\begin{pmatrix} <\psi_1|H|\psi_1> & <\psi_1|H|\psi_2> \\ <\psi_2|H|\psi_1> & <\psi_2|H|\psi_2> \end{pmatrix} \begin{pmatrix} c_1 \\ c_2 \end{pmatrix} = \epsilon \begin{pmatrix} c_1 \\ c_2 \end{pmatrix}$$

Then

$$<\psi_1|H|\psi_1>=<\psi_1|H|\psi_1>=\epsilon_0 + V_0, <\psi_1|H|\psi_2>=<\psi_2|H|\psi_1>=V_1 \tag{A.9}$$

where

$$V_0 = \frac{1}{L}\int V(x)dx, V_1 = \frac{1}{L}\int V(x)e^{i2\pi x/a}dx. \tag{A.10}$$

If the potential is attractive, then $V_0, V_1 < 0$. The eigenvalues of the matrix are

$$\epsilon = \epsilon_0 + V_0 \pm V_1 \tag{A.11}$$

and the eigenstates are

$$\psi_+ = \frac{1}{\sqrt{2}}(\psi_1 + \psi_2) = \frac{1}{\sqrt{2}}(e^{i\pi x/a} + e^{-i\pi x/a}) = \frac{2}{\sqrt{2}}\cos \pi x/a \tag{A.12}$$

and

$$\psi_- = \frac{1}{\sqrt{2}}(\psi_1 - \psi_2) = \frac{1}{\sqrt{2}}(e^{i\pi x/a} - e^{-i\pi x/a}) = \frac{-2i}{\sqrt{2}}\sin \pi x/a \tag{A.13}$$

The probability distribution of the wave functions are

$$|\psi_+|^2 = 2\cos^2\pi x/a, |\psi_-|^2 = 2\sin^2\pi x/a \tag{A.14}$$

Therefore, the eigenstates at $k = pi/a$ take the form of standing waves. If V is attractive and hence negative, the lower energy wave is peaked at $x = 0, a, 2a...$, and the higher energy wave is peaked at $x = a/2, 3a/2, 5a/2....$ Intuitively, this is reasonable; it is expected that the state is which the negatively charged electron is closest to the positively charged core should be at lower energy than the state where the electron is maximally peaked in between the ionic cores. Of critical importance, though, is that there is a gap in energy $2V_1$ between the states, and within this gap there are no allowed electronic states. Rather than allowing the energy bands to cross, the two bands merge to form a smooth lower energy band and a smooth higher energy band (see Fig. A.1). This is in stark contrast to a free electron state, in which an electron can take on any value of energy. Although this is a heavily simplified model, it still is informative as to the nature of energy gaps in three-dimensional crystals.

Another simplified way to visualize the formation of bands is the following: The energy levels of an well separated atoms are well defined. The electrons exist in orbitals with a specific energy associated with each orbital, and the energy levels of the separated atoms are degenerate. The orbital energies are separated by energy gaps. Now consider bringing the atoms closer and closer together, as in a crystal. The orbitals of the atoms will begin to mix, and due to interaction the degeneracy of the orbitals will be lifted. As the atoms are brought closer together the allowed energy in the orbitals will begin to broaden, and eventually some of the orbitals will merge to form bands. However, there will still be gaps in energy between the bands. Similar to single atoms in which the electrons exist in s, p, d, and f type orbitals, each band has an associated orbital angular momentum $L = 0, 1, 2...$ with $L_z \in L, L-1, L-2..., -L$.

A.3 Filling of bands: Conductors, Semiconductors, and Insulators

So far, we have considered the dispersion relationship of electrons in a lattice as smooth, continuous bands. However, this is only true in the case of an infinitely large lattice. For a finite lattice, the allowed values of k are broken into discrete momentum states. Consider a one-dimensional lattice of length $L = Na$, where N is the total number of unit cells and a is the lattice period. $\psi(x)$ is a Bloch function of the form e^{ikx}. Cyclic boundary conditions dictate that $\psi(x) = \psi(x + Na)$. Therefore, the boundary conditions require $e^{ikNa} = 1$, which restricts the values of k to

$$k = \frac{2\pi}{Na} l \tag{A.15}$$

where l is an integer. Note that the number of allowed k states from $-\pi/a < k < \pi/a$ is equal to N.

Electrons are fermions, i.e. spin 1/2 particles, and hence obey Fermi statistics. The Pauli exclusion principle dictates no more than one spin-up and one spin-down electron can occupy a given energy state. Therefore, electrons is a band effectively stack on top of each other in k-space, and in the limit temperature $T \to 0$ state the band is filled up to the Fermi energy.

The location of the Fermi level with respect to the band structure largely determines the conductive properties of the crystal. Assume a simple band structure at $T = 0$, in which the band is only partially filled with electrons. There will be an equal number of electrons with positive and negative k and hence positive and negative V. Applying an electric field along the x-axis will add some small momenta δk to each electron. Rather than considering a shift in momentum of all electrons, alternatively consider shifting one electron with initial momentum $k_i = -k_F$ to final momentum $k_f = k_F + 2\pi/(NA)$. Due to the close level spacing of energy levels in the band, it will cost little energy to shift an electron from $-k$ to $+k$. Then, there will be more electrons flowing in one direction than the other direction, and a current will arise. Therefore, a material with a partially filled band is conductive to electricity. Now consider a band in which

all electron states are occupied. In this case, the fermi level with be in the energy gap between bands. Since there are no empty states in the band, an electric field cannot shift the distribution of electrons to $+k$ or $-k$, and hence no current will flow in the presence of an electric field. Therefore, a material with the fermi level in between bands is an insulator. The difference between an "insulator" and a "semiconductor" is purely semantic. Both materials are characterized by the fermi level residing in the band-gap of the material; however, the band-gap in a material considered to be a semiconductor is generally smaller than in a material considered to be an insulator. In a semiconductor, a filled band is referred to as a valence band, and an empty band is referred to as a conduction band.

Finally, consider a nearly full band that is only missing a single electron, therefore leaving a single momentum state empty. Calculating the dynamics of all the electrons in the band would be quite complex; rather, it is much simpler to consider the dynamics of the vacant momentum state, also known as a *hole*. A hole carries charge $+e$. A hole in a energy band has some similarity to an bubble in water. A bubble flowing in one direction in water is equivalent to water with the volume of the bubble flowing in the opposite direction. Furthermore, a bubble will rise towards the surface in water in order to minimize the potential energy of the water. Similarly, a hole will minimize the energy of the electronic states in a band by "rising" towards higher energy states.

Appendix B

Electronic and optical properties of GaAs

B.1 Crystal and band structure of GaAs

GaAs is a zincblende crystal with lattice constant a = 5.6Å. The simplest way to visualize the crystal structure of GaAs is to consider it as a Face-Centered Cubic (FCC) lattice of Arsenic and a FCC lattice of Gallium, each with the same lattice constant and offset from eachother along the (111) direction by $d/4$, where d is the body diagonal of one the FCC units. GaAs is a semiconductor, meaning the electronic Fermi energy resides in a band gap. For a discussion of the fundamental differences between conductors and semiconductors, please consult Appendix A. The calculation of the full band structure of GaAs is beyond this work; instead, we will consider the band structure in the vicinity of the band gap. For GaAs, the band gap is direct (which will be discussed in the next section) and occurs at the so-called Γ point, which is at the center of the Brillouin zone.

In the region of the gap, there are four bands of interest. There is a single conduction band and three valence bands: The heavy-hole band, the light-hole band, and the split-off band, (see Fig. B.2). The GaAs samples studied in this thesis have a fundamental band gap of ΔE = 1.515eV at $T_{lattice}$ = 1.4K. Similar to atomic orbitals, each energy band has an associated quantized orbital angular

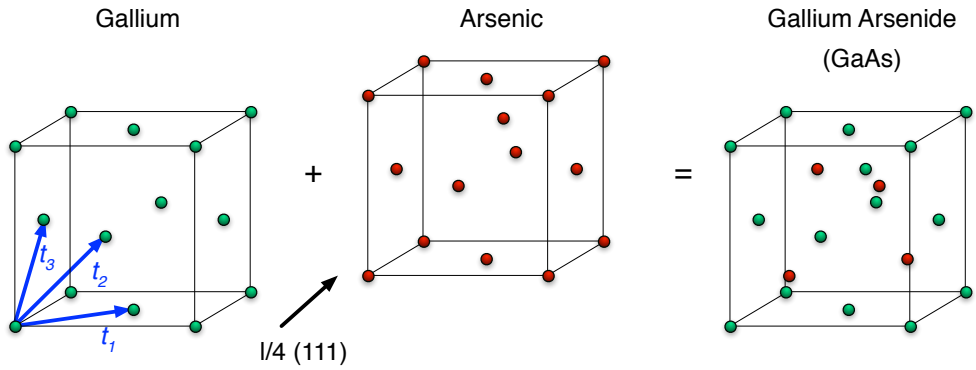

Figure B.1: Crystal structure of Gallium Arsenide. The three primitive lattice vectors t_1=(110), t_2=(101), and t_3=(011) are shown. The primitive lattice vectors have length $a/2$, where a is the lattice constant.

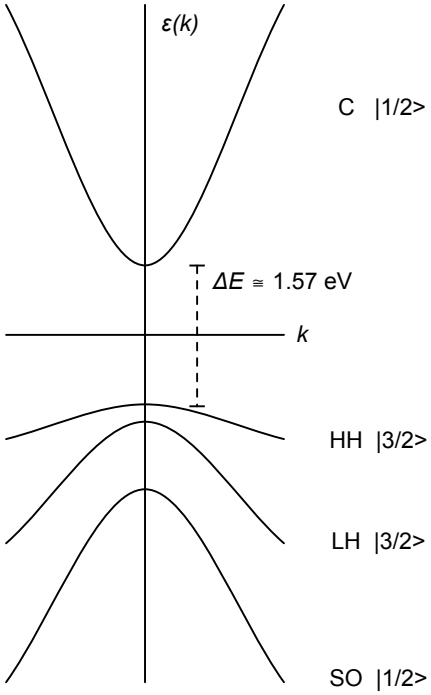

Figure B.2: Band structure of Gallium Arsenide in a two-dimensional quantum well. The bands shown are the conduction band (C), Heavy Hole band (HH), Light Hole band (LH), and Split Off band (SO). The total orbital quantum number j is also indicated. Energies are not drawn to scale.

momentum. The conduction band is an *S*-type orbital, meaning the orbital angular momentum $l = 0$, and hence the total angular momentum $j = l + s = 1/2$. The valence band structure of GaAs is more complex; the valence band is composed of *P*-type orbitals with $l = 1$. This means $j = 3/2$ or $1/2$. An electron in an orbital experiences a magnetic field due to its motion around a positively charged ion. This magnetic field couples to the angular momentum of the electron, and hence the strength of the interaction depends on the total electron angular momentum (spin plus orbital). For this reason, the $j = 1/2$ band has a lower energy by ≈ 300meV than the $j = 3/2$ bands, and is referred to as the split-off band. In bulk GaAs, the $j = 3/2$ states are degenerate at $k = 0$. However, due to differences in the electronic wave functions, the $j = 3/2$ states have different dispersions, and hence different effective mass. Recalling that the mass of an electron in a crystal is inversely proportional to the band curvature, the lower curvature band is referred to as the *heavy-hole* band and the higher curvature band is referred to as the *light-hole* band. In bulk GaAs, these bands are degenerate at $k = 0$. In the quantum well structure studied in this thesis, there is symmetry breaking between the z-axis and the x- and y-axes; this symmetry breaking splits the energies of the heavy-hole and light-hole bands at $k = 0$ by ≈ 15meV.

B.2 Optical properties of GaAs

Due to its abundance and the ease of high-purity fabrication, silicon is the most common semiconductor used in computation. However, as a semiconductor material for optoelectronics it is rather poorly behaved. This is due to the fact that its fundamental band gap is *indirect*, meaning that the bottom of the conduction band is offset in momentum space from the top of the valence band by a wavenumber on the order of the Brillouin zone. This means that an optical excitation would not only need to impart the necessary energy (due to Fermi's Golden Rule), but also impart the necessary momentum due to conservation. Photons with energy on the order of the bandgap in a semiconductor

lattices typically have a large wavelength compared to the lattice constant and hence have a very small wavenumber compared to the size of the Brillouin zone. Therefore a purely optical transition cannot significantly change the wavenumber of the electron due to momentum conservation. In Silicon this means that in order to absorb or emit a photon at the band gap, momentum conservation requires simultaneous absorption or emission of a phonon. This is a second order process, and hence the process is inefficient.

GaAs, on the other hand, has a band gap that is *direct* in momentum space, meaning that the top of the valence band occurs at the same momentum as the bottom of the valence band. Therefore, absorption or emission is a first order process. This is critical for its applications in optoelectronics. Furthermore, its band gap corresponds to light of wavelength $\lambda \approx 790$nm, a wavelength highly compatible with conventional optics, such as TiSaph lasers and near-infrared cameras. Excitons are optically active quasiparticles; therefore, it useful to study and utilize excitons in materials that have readily accessible and convenient optical transitions, materials such as GaAs.

B.3 Excitons in GaAs

Now, consider the absorption of an above-band gap photon by an electron in the heavy-hole valence band. The electron will be promoted by a vertical transition to the conduction band, and hence will leave behind a hole in the valence band. The negatively charged electron and the positively charged hole will be attracted to each other. Just as a proton and an electron can bind to form hydrogen, the electron and hole can form a bound state called an *exciton*. The combined motion of the electron and hole can be decomposed into the center-of-mass motion of the electron-hole pair and the relative motion of the electron with respect to the hole. The relative motion takes on quantized energy levels and wave functions, similar to the energy levels and wave functions in hydrogen, and can range from tightly bound states to continuum states in which the electron and hole are essentially free. In [Sivalertporn *et al.*, 2012], it is shown that the

energy difference between the $n = 1$ and $n = 2$ indirect exciton energy levels is approximately 3meV. In this dissertation we mainly consider indirect excitons with exciton temperature $T_{ex} < 10$K. Then, the thermal energy $k_B T < 1$meV. Therefore, the thermalized excitons in this paper will reside in the $n = 1$ internal ground state and the higher internal energy levels can be neglected.

Eventually, the electron will recombine with the hole and release a photon with energy equal to the exciton energy. In photon emission, energy and momentum must be conserved. For bulk excitons, this condition is met only at the spherical surface in k-space where the exciton and photon dispersion intersect. As explained in [Hopfield, 1958], no real excitonic transitions can take place in such a system; rather, the eigenstates of the system will be exciton-polariton states, in which the energy is shared between an exciton and a photon state. In a two dimensional quantum well, however, momentum conservation is relaxed along the z-axis; this allows all excitons within the energy of the light cone to emit photons and hence become optically active. Calculating this energy is relatively straightforward. At the photon cone

$$k_{photon} = k_{exciton}, \tag{B.1}$$

$$\epsilon_{photon} = \epsilon_{exciton} \tag{B.2}$$

For exciton emission at ≈ 800nm, $\epsilon_{photon} = 1.55$eV. Then

$$k_{exciton} = k_{photon} = \frac{n\epsilon_{photon}}{\hbar \mathrm{c}} \tag{B.3}$$

where n is the dielectric constant of the material. For GaAs, $n = 3.3$. Assuming a parabolic band for low energies the exciton kinetic energy at the photon cone can be described by

$$\epsilon_{exciton} = \frac{\hbar^2 k^2}{2m_{ex}} = \frac{n^2 \epsilon_{photon}^2}{2m_{ex}c^2}, \tag{B.4}$$

where $m_{ex} = 0.22m_0$ and m_0 is the electron mass in a vacuum. Then, within this approximation $\epsilon_{exciton} = 0.1$meV. Therefore, from first principles only low kinetic-energy exciton states with $\epsilon < 0.1$meV should be optically active. This is a simplification; exciton-photon and exciton-exciton scattering processes can

allow higher energy excitons to become optically active, see chapter 3. Statistical processes such as Bose-Einstein condensation and physical properties such as the exciton coherence length (which can be related to Bose-Einstein condensation) can significantly effect the exciton emission rate, see [Butov & Filin, 1998]. However, the fact that the exciton emission rate is k-dependent implies that even in a classical Boltzmann framework the emission rate of a thermal cloud of excitons will be temperature dependent.

As mentioned previously, electrons in the conduction band have spin $s = \pm 1/2$, while the heavy-hole band has spin $s = \pm 3/2$. Therefore, as a combination of two fermions the exciton must be bosonic with integer total spin that can take on four possible values, $S = \pm 2, \pm 1$. Due to optical selection rules, the emission of photons from $S = \pm 2$ states is forbidden to first-order, and hence they are referred to as *dark states*, whereas emission of a photon from an $s = \pm 1$ state is not forbidden and hence these are referred to as *bright states*.

Appendix C

Derivation of momentum distribution from A_{interf}

C.1 The first order coherence function

Coherence of excitons at two separate points $\mathbf{r}_1$ and $\mathbf{r}_2$ of space can be quantified by the density matrix, which is defined by the expectation value

$$\rho_{jk}(\mathbf{r}_1, \mathbf{r}_2) = \langle \psi_j^\dagger(\mathbf{r}_1)\psi_k(\mathbf{r}_2)\rangle\,, \tag{C.1}$$

where $\psi_j^\dagger$ and ψ_k are the equal-time creation and annihilation operators of excitons in the four possible J_z-states labeled by j and k. Coherence of the excitons is imprinted on their emission:

$$\langle E_j^*(\mathbf{r}_1)E_k(\mathbf{r}_2)\rangle \;= M_{jk}\rho_{jk}(\mathbf{r}_1, \mathbf{r}_2)\,, \tag{C.2}$$

where j and k are now restricted to the $J_z = \pm 1$ components and E_j is the electric field amplitude of the corresponding circular polarization of light. If most of occupied exciton momenta q are much smaller than $2\pi/\lambda$, we can treat M_{jk} as constants. Hence, optical measurements can give direct access to determining $\rho_{jk}(\mathbf{r}_1, \mathbf{r}_2)$.

Instead of the left-hand side of Eq. (C.2), one traditionally considers the

optical first-order coherence function

$$g_1(\mathbf{r}_1, \mathbf{r}_2) = \sum_{j,k=\pm 1} c_{jk} \langle E_j^*(\mathbf{r}_1) E_k(\mathbf{r}_2) \rangle \,, \tag{C.3}$$

where the coefficients c_{jk} describe the transformation from the circular-polarization basis to the measured polarization state, e.g., all $c_{jk} = 1/4$ for the x-polarization. To elaborate further on the relation between functions g_1 and ρ_{jk}, we make several simplifying assumptions. First, we assume that the system is uniform, so that all observables depend only on the distance $r = |\mathbf{r}_1 - \mathbf{r}_2|$ between the observation points. Second, we neglect spin-orbit coupling and crystal anisotropies, so that we end up with a four-fold degenerate parabolic $\varepsilon_q = \hbar^2 q^2/(2m)$ exciton spectrum. Third, we assume that all the four components are equally occupied and completely independent (have no mutual coherence). These assumptions are made primarily because there is no full theoretical understanding of coherence in a gas with spin-orbit coupling, interaction, and spatial inhomogeneity.

It is also convenient to consider relations between quantities in the momentum space. The Fourier transform of $\rho(r)$ is the momentum distribution n_q. The proportionality between g_1 and ρ implies

$$g_1(r) = C_1 \int d^2q \, e^{i\mathbf{qr}} n_q \,, \tag{C.4}$$

where constant C_1 provides the normalization $g_1(0) = 1$. Conversely, Eq. (C.4) indicates that n_q is proportional to the Fourier transform $\tilde{g}_1(q)$ of $g_1(r)$. This conclusion is very important because function n_q gives information about interactions, coherence, and phase transitions in the system. Its calculation for interacting particles remains a challenging many-body problem [Kagan *et al.*, 2000]. In particular, no theoretical results for n_q have been reported for the system under study, where the interaction are dipolar and the spin-orbit coupling is important. For illustrative purposes, we will discuss n_q and $g_1(r)$ in a *noninteracting* model. In this model n_q is given by the Bose-Einstein distribution

$$n_q = \frac{1}{e^{(\varepsilon_q - \mu)/T} - 1} \,, \tag{C.5}$$

where the chemical potential μ is related to exciton density n, temperature T expressed in energy units, and spectral degeneracy $N = 4$ by

$$\mu = T \ln\left(1 - e^{-n/n_*}\right), \quad n_* = \frac{N}{\lambda_{dB}^2}. \tag{C.6}$$

Here

$$\lambda_{dB} = \sqrt{\frac{2\pi\hbar^2}{mT}} \tag{C.7}$$

is the thermal de Broglie wavelength. In turn, the occupation of the $q = 0$ state is given by

$$n_0 = e^{n/n_*} - 1. \tag{C.8}$$

As T decreases at fixed n, the occupation n_0 of the ground state increases, leading in finite-size systems to condensation of all particles to the ground state.

Let us discuss the consequences of this formula in two limiting cases. First, at high T or low n, we deal with a classical gas where $n_q \simeq e^{(\mu-\varepsilon_q)/T} \ll 1$ and Eq. (C.4) yields

$$g_1(r) \simeq e^{-\pi r^2/\lambda_{dB}^2}. \tag{C.9}$$

Following the definition of the coherence length $g_1(\xi) = e^{-1}$ from chapter 4, we conclude that for the classical gas $\xi = \lambda_{dB}/\sqrt{\pi}$. In our system this corresponds to $\xi \approx 0.3\,\mu$m at $T = 0.1$ K.

In the quantum limit of low T (or high n) and $r \gg \lambda_{dB}$, we can replace Eq. (C.5) by

$$n_q \simeq \frac{T}{\varepsilon_q + |\mu|} \gg 1, \tag{C.10}$$

which leads to

$$g_1(r) \propto K_0\left(\frac{r}{\xi_0}\right), \quad \xi_0 = \sqrt{\frac{n_0}{4\pi}}\,\lambda_{dB}, \tag{C.11}$$

where $K_0(z)$ is the modified Bessel (MacDonald) function. Hence, function $g_1(r)$ decays logarithmically at $\lambda_{dB} \ll r \ll \xi_0$ and then exponentially at larger r. The coherence length ξ is somewhat smaller than ξ_0 and much larger than λ_{dB}. As T decreases at fixed n, occupation factor n_0 and therefore ξ_0 grow exponentially with T.

The plots of $g_1(r)$ for two representative densities are shown in Fig. 4.5b by the broken lines. The blue line corresponds to the classical gas where $n_0 \ll 1$

and the black line depicts the quantum gas with $n_0 \approx 5000$. In agreement with the above discussion, crossover from the classical to quantum exciton gas is accompanied by a sharp increase of the coherence length.

C.2 Optical resolution effects

Experimentally, exciton emission is imaged by an optical system with a finite spatial resolution. Let us denote by $g_1^*(r)$ the coherence function obtained if the resolution is perfect (as assumed in the previous section) and let $g_1(r)$ stand for the observable one. The optical resolution effect can be understood by examining how plane waves with different transverse momenta q pass through the imaging system. The corresponding complex transmission coefficient $f(q)$ is sometimes termed the pupil function. We adopt the following common model [Hopkins, 1955]

$$f(q) = \Theta(Q - q) \exp\left(\frac{i}{2} D q^2\right), \quad Q = k\,\mathrm{NA}\,, \tag{C.12}$$

where $k = 2\pi/\lambda$ is the optical wavenumber and NA is numerical aperture. In our experiments NA = 0.27, which implies $Q = 2.08\,\mu\mathrm{m}^{-1}$. Parameter $D \sim \delta z/k$ accounts for defocussing, with δz being the defocussing length. The observed $g_1(r)$ can be expressed as the integral

$$g_1(r) = C_2\,\mathrm{Re} \int d^2q\, e^{i\mathbf{qr}} f^2(q) \tilde{g}_1^*(q)\,, \tag{C.13}$$

where C_2 is another normalization constant. The implications of this model for $g_1(r)$ are as follows.

At high T, where the momentum distribution is very broad, $\tilde{g}_1^*(q)$ can be replaced by a constant (see the blue solid line in Fig. 4.5c of the chapter 4), and so $g_1(r)$ is determined solely by the optical resolution parameters Q and D:

$$g_1(r) = C_3 \int_0^Q J_0(qr) \cos Dq\, q dq\,. \tag{C.14}$$

The resultant first-order coherence function $g_1(r)$ is characterized by rapidly decaying oscillations, similar to the familiar Airy pattern. In the chapter 4, this

structure was referred to as the point-spread function (PSF). A good fit to the experimentally observed high-temperature $g_1(r)$ is obtained for $D = 0.5\,\mu\text{m}^2$, see Fig. 4.5a. This corresponds to defocussing length $\delta z \sim Dk \approx 4\,\mu$m, which is reasonable. The width of the main maximum of the PSF sets the scale of our optical resolution.

At low temperatures and at distances $r \gg 1/Q$ the optical resolution effects play no role for the shape of the $g_1(r)$ curve. However, the difference in the short-range behavior imposes a different normalization. Hence, we get $g_1(r) = C_4 g_1^*(r)$, where C_4 is another constant. The results are illustrated by the solid lines in Fig. 4.5b. In Fig. 4.5a and 4.5c we also show that experimental data for g_1 and its Fourier transform $\tilde{g}_1$ can be adequately fitted to classical (quantum) gas models at high (low) T. However, this fitting should not be overemphasized because of the limited range of the data and approximations made in the presented theory.

C.3 Acknowledgements

The text of appendix C, in part, is a reprint of the material as it appears in A.A. High, J.R. Leonard, A.T. Hammack, M.M. Fogler, L.V. Butov, A.V. Kavokin, K.L. Campman & A.C. Gossard, *Spontaneous coherence in a cold exciton gas*, Nature 483, 584 (2012), ©Nature Publishing Group, where the dissertation author was the first author. The co-authors in this publication directed, supervised, and co-worked on the research which forms the basis of this appendix.

Appendix D

Modeling of Spin Texture

The model considers excitons around an LBS ring, which is close to a radially symmetric source of excitons, for details on LBS rings see [Butov *et al.*, 2002; Butov, 2004; Yang *et al.*, 2010]. An LBS ring has a hot core region [Butov, 2004], which is not described by the model. The initial exciton state considered by this model is a ring around the LBS center where the exciton temperature reaches the limit below which excitons propagate ballistically and keep coherence within the limits of the observed spin texture. The model assumes a thermal distribution of excitons on this ring and their coherent (ballistic) radial propagation away from the center with velocity $v = \hbar k_{ex}/m$, where $\mathbf{k}_{ex} = \mathbf{k}_e + \mathbf{k}_h$ is the exciton wave vector and m is the exciton effective mass in the plane of the structure, $\mathbf{k}_e = \frac{m_e}{m}\mathbf{k}_{ex}$, $\mathbf{k}_h = \frac{m_h}{m}\mathbf{k}_{ex}$, m_e and m_h are electron and hole in-plane effective masses, respectively. In the basis of four exciton states with spins $\{+1, -1, +2, -2\}$, the coherent spin dynamics in the system is governed by a model matrix Hamiltonian:

$$H_{exc} = \begin{pmatrix} E_{bright} & -\delta_b & k_e\beta_e e^{-i\varphi} & k_h\beta_h e^{-i\varphi} \\ -\delta_b & E_{bright} & k_h\beta_h e^{i\varphi} & k_e\beta_e e^{i\varphi} \\ k_e\beta_e e^{i\varphi} & k_h\beta_h e^{-i\varphi} & E_{dark} & -\delta_d \\ k_h\beta_h e^{i\varphi} & k_e\beta_e e^{-i\varphi} & -\delta_d & E_{dark} \end{pmatrix}, \tag{D.1}$$

where E_{bright} and E_{dark} are energies of bright and dark excitons in an ideal isotropic QW, δ_b and δ_d describe the effect of in-plane anisotropy induced by the crystallographic axis orientation and strain and resulting in the splitting of

exciton states linearly polarized along [110] and [0 − 10] axes of symmetry. The angle φ is defined relative to the $x \equiv$ [110] axis. This Hamiltonian has been constructed from the spin–orbit Hamiltonians for electrons and holes [Luo *et al.*, 2010], including an exciton spin anisotropy:

$$H_{exc} = H_{anis} + \mathbf{1}_e \otimes H_h + H_e \otimes \mathbf{1}_h \,, \tag{D.2}$$

where the operators $\mathbf{1}_{e,h}$ are 2×2 identity matrices, $H_e = \beta_e \left(k_x^e \sigma_x - k_y^e \sigma_y\right)$ and $H_h = \beta_h \left(k_x^h \sigma_x + k_y^h \sigma_y\right)$,

$$H_{anis} = \begin{pmatrix} E_{bright} & -\delta_b & 0 & 0 \\ -\delta_b & E_{bright} & 0 & 0 \\ 0 & 0 & E_{dark} & -\delta_d \\ 0 & 0 & -\delta_d & E_{dark} \end{pmatrix}. \tag{D.3}$$

The evolution of the density matrix is then described in terms of the quantum Liouville equation:

$$i\hbar \, d\rho/dt = \left[H_{exc}, \rho\right] \tag{D.4}$$

The initial condition in the simulations is the thermal density matrix on the low–temperature ring around the LBS core:

$$\rho(R = R_0) = \begin{pmatrix} (n_1 + n_2)/2 & (n_1 - n_2)/2 & 0 & 0 \\ (n_1 - n_2)/2 & (n_1 + n_2)/2 & 0 & 0 \\ 0 & 0 & (n_3 + n_4)/2 & (n_3 - n_4)/2 \\ 0 & 0 & (n_3 - n_4)/2 & (n_3 + n_4)/2 \end{pmatrix}, \tag{D.5}$$

where the populations of the linearly polarized bright states are $n_{1,2} = \exp\Big[-\Big(E_{bright} \mp \delta_b\Big)/k_B T\Big]$ and populations of the dark states are $n_{3,4} = \exp\Big[-\Big(E_{dark} \mp \delta_d\Big)/k_B T\Big]$. Symbol k_B stands for the Boltzmann constant. The patterns of circular and linear polarizations are extracted from the density matrix using the formulas $P_\sigma(R) = \Big[\rho_{11}(R) - \rho_{22}(R)\Big]/\Big[\rho_{11}(R) + \rho_{22}(R)\Big]$ and $P_{lin}(R) = 2\mathrm{Re}\Big[\rho_{12}(R)\Big]/\Big[\rho_{11}(R) + \rho_{22}(R)\Big]$, respectively.

Figures 4.15a,b show the results of our calculations, considering the following parameters. The energies of exciton states were defined by the parameters $E_{dark} = 0$ μeV, $E_{bright} = 5$ μeV, $\delta_b = +1$ μeV, $\delta_d = -8$ μeV. The Dresselhaus coefficients were taken to be $\beta_e = 25$ meVÅ and $\beta_h = 23.5$ meVÅ, the first

value has been experimentally measured in our earlier work [Leonard *et al.*, 2009], the value for β_h is in qualitative agreement with the calculations in [Luo *et al.*, 2010]. The exciton temperature is $T = 0.2$ K, exciton propagation velocity $v = 3.4 \cdot 10^5$ cm/s, effective masses $m = 0.23\ m_0$, $m_e = 0.07\ m_0$, $m_h = 0.16\ m_0$ with m_0 being free electron mass, and $R_0 = 4.8\ \mu$m.

For a detailed fit of the experiment the spin dependent exciton-exciton interactions may need to be taken into account. Nevertheless, the present (linear) theory reproduces all main features of the spin texture observed in the experiment, namely, a ring of linear polarization (Fig. 4.15a), a vortex of linear polarization with the polarization perpendicular to the radial direction (Fig. 4.15a), and a four-leaf pattern of circular polarization (Fig. 4.15b).

The model is based on the assumption of ballistic radial transport of excitons. In this regime, the main mechanism of hole spin relaxation (Elliott-Yafet mechanism linked with the scattering of holes by impurities) is suppressed. The spin dynamics of electrons and holes is governed by the spin-orbit interaction described by the Dresselhaus Hamiltonian, which we use in the model. The splitting of linearly polarized states of bright and dark excitons is an essential element of the model, which allows to describe the central linear polarization ring and the build-up of circular polarization. Such splittings typically appear in MBE grown samples due to monolayer fluctuations of the heteroboundaries. The values of these two splittings in our sample are fitting parameters of the model. A good qualitative agreement between the model and experiment indicates that the observed spin texture is a characteristic feature of a new exciton transport regime where coherence is kept over large distances.

D.1 Acknowledgements

The text of appendix D, in part, is a reprint of the material as it appears in A.A. High, A.T. Hammack, J.R. Leonard, Sen Yang, L.V. Butov, T. Ostatnicky, A.V. Kavokin & A.C. Gossard, *Spin texture in a cold exciton gas*, arXiv:1103.0321, where the dissertation author was the first author. The co-authors in this publication

directed, supervised, and co-worked on the research which forms the basis of this appendix.

Bibliography

Alloing, M., Lemaître, A., Galopin, E., & Dubin, F. (2012). On-demand confinement of semiconductor excitons by all-optical control. *arXiv:1202.3301v1*.

Anderson, M. H., Ensher, J. R., Matthews, M. R., Wieman, C. E., & Cornell, E. A. (1995). Observation of Bose-Einstein condensation in a dilute atomic vapor. *Science*, *269*, 198–201.

Aull, B. F., Nichols, K. B., Maki, P. A., Palmateer, S. C., Brown, E. R., & Lind, T. A. (1993). Monolithic optoelectronic transistor - a new smart-pixel device. *Applied Physics Letters*, *63*(11), 1555–1557.

Baldo, M. & Stojanovic, V. (2009). Excitonic interconnects. *Nature Photonics*, *3*(10), 558–560.

Bloch, F. (1929). Über die quantenmechanik der elektronen in kristallgittern. *Zeitschrift für Physik a Hadrons and Nuclei*, *52*, 555–600.

Bose, S. N. (1924). Plancks gesetz und lichtquantenhypothese. *Zeitschrift für Physik*, *26*, 178–181.

Bradley, C. C., Sackett, C. A., Tollett, J. J., & Hulet, R. G. (1995). Evidence of Bose-Einstein condensation in an atomic gas with attractive interaction. *Phys. Rev. Lett.*, *75*, 1687–1690.

Brunner, K., Bockelmann, U., Abstreiter, G., Walther, M., Bohm, G., Trankle, G., & Weimann, G. (1992). Photoluminescence from a single GaAs/AlGaAs quantum dot. *Physical Review Letters*, *69*(22), 3216–3219.

Buchanan, J. (1996). *Signal and Power Integrity in Digital Systems: TTL, CMOS, & BiCMOS*. New York: Mcgraw-Hill.

Butov, L. V. (2004). Condensation and pattern formation in cold exciton gases in coupled quantum wells. *Journal of Physics-condensed Matter*, *16*(50), PII S0953–8984(04)58973–7.

Butov, L. V. & Filin, A. I. (1998). Anomalous transport and luminescence of indirect excitons in AlAs/GaAs coupled quantum wells as evidence for exciton condensation. *Physical Review B*, *58*(4), 1980–2000.

Butov, L. V., Gossard, A. C., & Chemla, D. S. (2002). Macroscopically ordered state in an exciton system. *Nature*, *418*(6899), 751–754.

Butov, L. V., Ivanov, A. L., Imamoglu, A., Littlewood, P. B., Shashkin, A. A., Dolgopolov, V. T., Campman, K. L., & Gossard, A. C. (2001). Stimulated scattering of indirect excitons in coupled quantum wells: Signature of a degenerate Bose-gas of excitons. *Physical Review Letters*, *86*(24), 5608–5611.

Butov, L. V., Mintsev, A. V., Lozovik, Y. E., Campman, K. L., & A.C., G. (2000). From spatially indirect excitons to momentum-space indirect excitons by an in-plane magnetic field. *Physical Review B*, *62*, 1548.

Butov, L. V., Zrenner, A., Abstreiter, G., Bohm, G., & Weimann, G. (1994). Condensation of indirect excitons in coupled AlAs/GaAs quantum-wells. *Physical Review Letters*, *73*(2), 304–307.

Chang, L. L., Esaki, L., & Tsu, R. (1974). Resonant tunneling in semiconductor double barriers. *Applied Physics Letters*, *24*, 593.

Chemla, D. S., Miller, D. A. B., Smith, P. W., Gossard, A. C., & Wiegmann, W. (1984). Room-temperature excitonic nonlinear absorption and refraction in GaAs/AlGaAs multiple quantum well structures. *IEEE Journal of Quantum Electronics*, *20*(3), 265–275.

Chen, G., Rapaport, R., Pffeifer, L. N., West, K., Platzman, P. M., Simon, S., Voros, Z., & Snoke, D. (2006). Artificial trapping of a stable high-density dipolar exciton fluid. *Physical Review B*, *74*(4), 045309.

Chen, H.-W., Kuo, Y.-H., & Bowers, J. E. (2008). High speed hybrid silicon evanescent Mach-Zehnder modulator and switch. *Optics Express*, *16*(25), 20571–20576.

Chen, X. M. & Quinn, J. J. (1991). Excitonic charge-density-wave instability of spatially separated electron-hole layers in strong magnetic-fields. *Physical Review Letters*, *67*(7), 895–898.

Christianen, P. C. M., Piazza, F., Lok, J. G. S., Maan, J. C., & van der VLeuten, W. (1998). Magnetic trap for excitons. *Physica B*, *251*, 624–627.

Cornell, E. A. & Wieman, C. E. (2002). Nobel lecture: Bose-Einstein condensation in a dilute gas, the first 70 years and some recent experiments. *Reviews of Modern Physics*, *74*(3), 875–893.

Dalfovo, F., Giorgini, S., Pitaevskii, L. P., & Stringari, S. (1999). Theory of Bose-Einstein condensation in trapped gases. *Reviews of Modern Physics*, *71*, 463.

Davis, K. B., Mewes, M., Andrews, M. R., van Druten, N. J., Durfee, D. S., Kurn, D. M., & Ketterle, W. (1995). Bose-Einstein condensation in a gas of sodium atoms. *Physical Review Letters*, *75*, 3969–3973.

de Andrada e Silva, G. C., E. A. & La Rocca (1997). Exciton-bound electron-spin relaxation. *Physical Review B 56*, *56*, 92599262.

Dingle, R., Wiegmann, W., & Henry, C. H. (1974). Quantum states of confined carriers in very thin $Al_xGa_{1-x}As-GaAs-Al_xGa_{1-x}As$ heterostructures. *Physical Review Letters*, *33*, 827.

Einstein, A. (1924). Quantentheorie des einatomigen idealen gases. *Sitzungsberichte der Preußischen Akademie der Wissenschaften, Physikalisch-mathematische Klasse*, 261–267.

Einstein, A. (1925). Quantentheorie des einatomigen idealen gases ii. *Sitzungsberichte der Preußischen Akademie der Wissenschaften, Physikalisch-mathematische Klasse*, 3–14.

Eisenstein, J. P. & MacDonald, A. H. (2004). Bose-Einstein condensation of excitons in bilayer electron systems. *Nature*, *432*(7018), 691–694.

Fertig, H. A. & Brey, L. (2007). Edge physics of graphene in the quantum hall regime. *European Physical Journal Special Topics*, *148*, 143 – 150.

Filinov, A., Prokofév, N. V., & Bonitz, M. (2010). Berezinskii-kosterlitz-thouless transition in two-dimensional dipole systems. *Physical Review Letters*, *105*, 070401.

Fogler, M. M., Yang, S., Hammack, A. T., Butov, L. V., & Gossard, A. C. (2008). Effect of spatial resolution on the estimates of the coherence length of excitons in quantum wells. *Physical Review B*, *78*(3), 035411.

Frenkel, J. (1931). On the transformation of light into heat in solids. i. *Physical Review*, *37*, 17–44.

Gammon, D., Snow, E. S., Shanabrook, B. V., Katzer, D. S., & Park, D. (1996). Fine structure splitting in the optical spectra of single GaAs quantum dots. *Physical Review Letters*, *76*(16), 3005–3008.

Gärtner, A., Holleitner, A. W., Kotthaus, J. P., & Schuh, D. (2006). Drift mobility of long-living excitons in coupled GaAs quantum wells. *Applied Physics Letters*, *89*(5), 052108.

Gibbs, H. M. (1985). *Optical bistability: Controlling Light with Light*. New York: Academic Press.

Girvin, S. M. (2000). Spin and isospin: Exotic order in quantum hall ferromagnets. *Physics Today*, *53*(6), 39–45.

Gorbunov, A. V. & Timofeev, V. B. (2006). Large-scale coherence of the Bose condensate of spatially indirect excitons. *JETP Letters*, *84*, 329–334.

Green, W. M. J., Rooks, M. J., Sekaric, L., & Vlasov, Y. A. (2007). Ultra-compact, low rf power, 10 gb/s silicon Mach-Zehnder modulators. *Optics Express*, *15*(25), 17106–17113.

Grosso, G., Graves, J., Hammack, A. T., High, A. A., Butov, L. V., Hanson, M., & Gossard, A. C. (2009). Excitonic switches operating at around 100 k. *Nature Photonics*, *3*(10), 577–580.

Grosso, G. & Parravicini, G. P. (2000). *Solid State Physics*. Academic Press.

Hadzibabic, Z., Kruger, P., Cheneau, M., Battelier, B., & Dalibard, J. (2006). Berezinskii-Kosterlitz-Thouless crossover in a trapped atomic gas. *Nature*, *441*(7097), 1118–1121.

Hagn, M., Zrenner, A., Bohm, G., & Weimann, G. (1995). Electric-field-induced exciton transport in coupled-quantum-well structures. *Applied Physics Letters*, *67*(2), 232–234.

Hammack, A. T., Butov, L. V., Wilkes, J., Mouchliadis, L., Muljarov, E. A., Ivanov, A. L., & Gossard, A. C. (2009). Kinetics of the inner ring in the exciton emission pattern in coupled GaAs quantum wells. *Physical Review B*, *80*(15), 155331.

Hammack, A. T., Gippius, N. A., Yang, S., Andreev, G. O., Butov, L. V., Hanson, M., & Gossard, A. C. (2006a). Excitons in electrostatic traps. *Journal of Applied Physics*, *99*(6), 066104.

Hammack, A. T., Griswold, M., Butov, L. V., Smallwood, L. E., Ivanov, A. L., & Gossard, A. C. (2006b). Trapping of cold excitons in quantum well structures with laser light. *Physical Review Letters*, *96*(22), 227402.

Hegarty, J., Goldner, L., & Sturge, M. D. (1984). Localized and delocalized two-dimensional excitons in GaAs-AlGaAs multiple-quantum-well structures. *Physical Review B*, *30*(12), 7346–7348.

Hess, H. F., Betzig, E., Harris, T. D., Pfeiffer, L. N., & West, K. W. (1994). Near-field spectroscopy of the quantum constituents of a luminescent system. *Science*, *264*(5166), 1740–1745.

High, A. A., Hammack, A. T., Butov, L. V., Mouchliadis, L., Ivanov, A. L., Hanson, M., & Gossard, A. C. (2009a). Indirect excitons in elevated traps. *Nano Letters*, *9*(5), 2094–2098.

High, A. A., Leonard, J. R., Hammack, A. T., Fogler, M. M., Butov, L. V., Kavokin, A. V., Campman, K. L., & Gossard, A. C. (2012). Spontaneous coherence in a cold exciton gas. *Nature*, *483*, 584–588.

High, A. A., Thomas, A. K., Grosso, G., Remeika, M., Hammack, A. T., Meyertholen, A. D., Fogler, M. M., Butov, L. V., Hanson, M., & Gossard, A. C. (2009b). Trapping indirect excitons in a GaAs quantum-well structure with a diamond-shaped electrostatic trap. *Physical Review Letters*, *103*(8), 087403.

Hopfield, J. J. (1958). Theory of the contribution of excitons to the complex dielectric constant of crystals. *Physical Review*, *112*, 5.

Hopkins, H. (1955). The frequency response of a defocused optical system. *Proc. Roy. Soc. London Ser. A*, *231*, 91.

Huber, T., Zrenner, A., & Wegscheider, W. (1998). Electrostatic exciton traps. *Physica Status Solidi A-applied Research*, *166*(1), R5–R6.

Ivanov, A. L. (2002). Quantum diffusion of dipole-oriented indirect excitons in coupled quantum wells. *Europhysics Letters*, *59*(4), 586–591.

Ivanov, A. L., Littlewood, P. B., & Haug, H. (1999). Bose-Einstein statistics in thermalization and photoluminescence of quantum-well excitons. *Physical Review B*, *59*(7), 5032–5048.

Ivanov, A. L., Muljarov, E. A., Mouchliadis, L., & Zimmermann, R. (2010). Comment on "Photoluminescence ring formation in coupled quantum wells: Excitonic versus ambipolar diffusion". *Physical Review Letters*, *104*(17), 179701.

Ivanov, A. L., Smallwood, L. E., Hammack, A. T., Yang, S., Butov, L. V., & Gossard, A. C. (2006). Origin of the inner ring in photoluminescence patterns of quantum well excitons. *Europhysics Letters*, *73*(6), 920–926.

Jang, J. I. & Wolfe, J. P. (2006). Auger recombination and biexcitons in Cu_2O: A case for dark excitonic matter. *Physical Review B*, *74*(4), 045211.

Jiang, Y. Q., Jiang, W., Gu, L. L., Chen, X. N., & Chen, R. T. (2005). 80-micron interaction length silicon photonic crystal waveguide modulator. *Applied Physics Letters*, *87*(22), 221105.

Kagan, Y., Kashurnikov, V., Krasavin, A., Prokofév, N., & Svistunov, B. (2000). Quasicondensation in a two-dimensional interacting Bose gas. *Physical Review A*, *61*, 043608.

Karmakar, B., Pellegrini, V., Pinczuk, A., Pfeiffer, L. N., & West, K. W. (2009). First-order quantum phase transition of excitons in quantum Hall bilayers. *Physical Review Letters*, *102*(3), 036802.

Kash, K., Worlock, J. M., Sturge, M. D., Grabbe, P., Harbison, J. P., Scherer, A., & Lin, P. S. D. (1988). Strain-induced lateral confinement of excitons in GaAs-AlGaAs quantum well microstructures. *Applied Physics Letters*, *53*(9), 782–784.

Keldysh, L. V. (1986). The electron-hole liquid in semiconductors. *Contemporary Physics*, *27*(5), 395–428.

Keldysh, L. V. & Kopaev, Y. V. (1965). Possible instability of the semimetallic state toward Coulomb interaction. *Phys. Solid State*, *6*, 2219–2224.

Keldysh, L. V. & Kozlov, A. N. (1968). Collective properties of excitons in semiconductors. *Soviet Physics Jetp*, *27*(3), 521–528.

Ketterle, W. (2002). Nobel lecture: When atoms behave as waves: Bose-Einstein condensation and the atom laser. *Reviews of Modern Physics*, *74*(4), 1131–1151.

Ketterle, W. & van Druten, N. J. (1996). Bose-Einstein condensation of a finite number of particles trapped in one or three dimensions. *Physical Review A*, *54*, 656.

Kowalik-Seidl, K., Voegele, X. P., Rimpfl, B. N., Manus, S., Kotthaus, J. P., Schuh, D., Wegscheider, W., & Holleitner, A. W. (2010). Long exciton spin relaxation in coupled quantum wells. *Applied Physics Letters*, *97*(1), 011104.

Krenner, H. J., Pryor, C. E., He, J., & Petroff, P. M. (2008). A semiconductor exciton memory cell based on a single quantum nanostructure. *Nano Letters*, *8*(6), 1750–1755.

Krenner, H. J., Sabathil, M., Clark, E. C., Kress, A., Schuh, D., Bichler, M., Abstreiter, G., & Finley, J. J. (2005). Direct observation of controlled coupling in an individual quantum dot molecule. *Physical Review Letters*, *94*(5), 057402.

Kuznetsova, Y. Y., Remeika, M., High, A. A., Hammack, A. T., Butov, L. V., Hanson, M., & Gossard, A. C. (2010). All-optical excitonic transistor. *Optics Letters*, *35*(10), 1587–1589.

Lagoudakis, K. G., Ostatnicky, T., Kavokin, A. V., Rubo, Y. G., Andre, R., & Deveaud-Pledran, B. (2009). Observation of half-quantum vortices in an exciton-polariton condensate. *Science*, *326*(5955), 974–976.

Lagoudakis, K. G., Wouters, M., Richard, M., Baas, A., Carusotto, I., Andre, R., Dang, L. E. S. I., & Deveaud-Pledran, B. (2008). Quantized vortices in an exciton-polariton condensate. *Nature Physics*, *4*(9), 706–710.

Larionov, A. V. & Golub, L. E. (2008). Electric-field control of spin-orbit splittings in GaAs/Al_xGa_{1-x}As coupled quantum wells. *Physical Review B*, *78*(3), 033302.

Larionov, A. V., Timofeev, V. B., Hvam, J., & Soerensen, K. (2000). Interwell excitons in GaAs/AlGaAs double quantum wells and their collective properties. *Journal of Experimental and Theoretical Physics*, *90*(6), 1093–1104.

Lee, P. A. & Ramakrishnan, T. V. (1985). Disordered electronic systems. *Reviews of Modern Physics*, *57*(2), 287–337.

Leonard, J. R., Kuznetsova, Y. Y., Yang, S., Butov, L. V., Ostatnicky, T., Kavokin, A., & Gossard, A. C. (2009). Spin transport of excitons. *Nano Letters*, *9*(12), 4204–4208.

Leonard, J. R., Remeika, M., Kuznetsova, Y., High, A., Butov, L., Wilkes, J., Hanson, M., & Gossard, A. (2012). Transport of indirect excitons in a potential energy gradient. *Applied Physics Letters*, *100*, 231106.

Levitov, L. S., Simons, B. D., & Butov, L. V. (2005). Pattern formation as a signature of quantum degeneracy in a cold exciton systems. *Physical Review Letters*, *94*, 176404.

Leyder, C., Romanelli, M., Karr, J. P., Giacobino, E., Liew, T. C. H., Glazov, M. M., Kavokin, A. V., Malpuech, G., & Bramati, A. (2007). Observation of the optical spin Hall effect. *Nature Physics*, *3*(9), 628–631.

Liu, A. S., Jones, R., Liao, L., Samara-Rubio, D., Rubin, D., Cohen, O., Nicolaescu, R., & Paniccia, M. (2004). A high-speed silicon optical modulator based on a metal-oxide-semiconductor capacitor. *Nature*, *427*(6975), 615–618.

Liu, J., Beals, M., Pomerene, A., Bernardis, S., Sun, R., Cheng, J., Kimerling, L. C., & Michel, J. (2008). Waveguide-integrated, ultralow-energy GeSi electro-absorption modulators. *Nature Photonics*, *2*(7), 433–437.

Lozovik, Y. E. & Berman, O. K. (1996). Phase transitions in a system of two coupled quantum wells. *Jetp Letters*, *64*(8), 573–579.

Lozovik, Y. E. & Yudson, V. I. (1976). A new mechanism for superconductivity: pairing between spatially separated electrons and holes. *Sov. Phys. JETP*, *44*, 389–397.

Lundstrom, T., Schoenfeld, W., Lee, H., & Petroff, P. M. (1999). Exciton storage in semiconductor self-assembled quantum dots. *Science*, *286*(5448), 2312–2314.

Luo, J.-W., Chantis, A. N., van Schilfgaarde, M., Bester, G., & Zunger, A. (2010). Discovery of a novel linear-in-k spin splitting for holes in the 2d GaAs/AlAs systems. *Physical Review Letters*, *104*(6), 066405.

Maialle, M. Z., Silva, E. A. D. E., & Sham, L. J. (1993). Exciton spin dynamics in quantum-wells. *Physical Review B*, *47*(23), 15776–15788.

Miller, D. A. B. (2000). Rationale and challenges for optical interconnects to electronic chips. *Proceedings of the IEEE*, *88*(6), 728–749.

Miller, D. A. B., Chemla, D. S., Damen, T. C., Gossard, A. C., Wiegmann, W., Wood, T. H., & Burrus, C. A. (1984). Band-edge electroabsorption in quantum well structures: The quantum-confined Stark effect. *Physical Review Letters*, *53*, 2173–2176.

Miller, D. A. B., Chemla, D. S., Damen, T. C., Gossard, A. C., Wiegmann, W., Wood, T. H., & Burrus, C. A. (1985). Electric-field dependence of optical-absorption near the band-gap of quantum-well structures. *Physical Review B*, *32*(2), 1043–1060.

Milonni, P. & Eberly, J. (1988). *Lasers*. New York: Wiley.

Muehlbauer, S., Binz, B., Jonietz, F., Pfleiderer, C., Rosch, A., Neubauer, A., Georgii, R., & Boeni, P. (2009). Skyrmion lattice in a chiral magnet. *Science*, *323*(5916), 915–919.

Mullin, W. J. (1997). Bose-Einstein condensation in a harmonic potential. *Journal of Low Temperature Physics*, *106*, 615.

Naka, N. & Nagasawa, N. (2005). Bosonic stimulation of cold excitons in a harmonic potential trap in Cu_2O. *J. Lumin.*, *112*, 11–16.

Negoita, V., Snoke, D. W., & Eberl, K. (1999). Harmonic-potential traps for indirect excitons in coupled quantum wells. *Physical Review B*, *60*(4), 2661–2669.

Pathria, R. K. (1996). *Statistical Mechanics, Second Edition*. Elsevier Butterworth-Heinemann.

Penrose, O. & Onsager, L. (1956). Bose-Einstein condensation and liquid helium. *Physical Review*, *104*(3), 576–584.

Popov, V. N. (1972). On the theory of the superfluidity of two- and one- dimensional Bose systems. *Theoretical and mathematical physics*, *3*, 565–573.

Qi, X. L. & Zhang, S. C. (2010). The quantum spin Hall effect and topological insulators. *Physics Today*, *63*(1), 33–38.

Rapaport, R., Chen, G., Snoke, D., Simon, S. H., Pfeiffer, L., West, K., Liu, Y., & Denev, S. (2004). Charge separation of dense two-dimensional electron-hole gases: Mechanism for exciton ring pattern formation. *Physical Review Letters*, *92*(11), 117405.

Read, D., Liew, T. C. H., Rubo, Y. G., & Kavokin, A. V. (2009). Stochastic polarization formation in exciton-polariton Bose-Einstein condensates. *Physical Review B*, *80*(19), 195309.

Remeika, M., Graves, J. C., Hammack, A. T., Meyertholen, A. D., Fogler, M. M., Butov, L. V., Hanson, M., & Gossard, A. C. (2009). Localization-delocalization transition of indirect excitons in lateral electrostatic lattices. *Physical Review Letters*, *102*(18), 186803.

Sadler, L. E., Higbie, J. M., Leslie, S. R., Vengalattore, M., & Stamper-Kurn, D. M. (2006). Spontaneous symmetry breaking in a quenched ferromagnetic spinor Bose-Einstein condensates. *Nature*, *443*(7109), 312–315.

Salomaa, M. M. & Volovik, G. E. (1987). Quantized vortices in superfluid He-3. *Reviews of Modern Physics*, *59*(3), 533–613.

Scheibner, M., Ponomarev, I. V., Stinaff, E. A., Doty, M. F., Bracker, A. S., Hellberg, C. S., Reinecke, T. L., & Gammon, D. (2007). Photoluminescence spectroscopy of the molecular biexciton in vertically stacked InAs-GaAs quantum dot pairs. *Physical Review Letters*, *99*(19), 197402.

Scheuer, J. & Orenstein, M. (1999). Optical vortices crystals: Spontaneous generation in nonlinear semiconductor microcavities. *Science*, *285*(5425), 230–233.

Schindler, C. & R., Z. (2008). Analysis of the exciton-exciton interaction in semiconductor quantum wells. *Physical Review B*, *78*, 045313.

Schinner, G. J., Schubert, E., Stallhofer, M. P., Kotthaus, J. P., Schuh, D., Rai, A. K., Reuter, D., Wieck, A. D., & Govorov, A. O. (2011). Electrostatically trapping indirect excitons in coupled $In_xGa_{1-x}As$ quantum wells. *Physical Review B*, *83*, 165308.

Sivalertporn, K., Mouchliadis, L., Ivanov, A. L., Philp, R., & Muljarov, E. A. (2012). Direct and indirect excitons in semiconductor coupled quantum wells in an applied electric field. *Physical Review B*, *85*, 045207.

Spielman, I. B., Eisenstein, J. P., Pfeiffer, L. N., & West, K. W. (2000). Resonantly enhanced tunneling in a double layer quantum hall ferromagnet. *Physical Review Letters*, *84*(25), 5808–5811.

Stinaff, E., Scheibner, M., Bracker, A., Ponomarev, I., Korenev, V., Ware, M., Doty, M., Reinecke, T., & Gammon, D. (2006). Optical signatures of coupled quantum dots. *Science*, *311*(5761), 636–639.

Szymanska, M. H. & Littlewood, P. B. (2003). Excitonic binding in coupled quantum wells. *Physical Review B*, *67*(19), 193305.

Takagahara, T. (1985). Localization and energy-transfer of quasi-2-dimensional excitons in GaAs-AlAs quantum-well heterostructures. *Physical Review B*, *31*(10), 6552–6573.

Tiemann, L., Lok, J. G. S., Dietsche, W., von Klitzing, K., Muraki, K., Schuh, D., & Wegscheider, W. (2008). Exciton condensate at a total filling factor of one in Corbino two-dimensional electron bilayers. *Physical Review B*, *77*(3), 033306.

Tikhodeev, S. G., Kopelevich, G. A., & Gippius, N. A. (1998). Exciton transport in Cu_2O: Phonon wind versus superfluidity. *Physica Status Solidi B-basic Research*, *206*(1), 45–53.

Trauernicht, D. P., Mysyrowicz, A., & Wolfe, J. P. (1983). Strain confinement and thermodynamics of free-excitons in a direct-gap semiconductor. *Physical Review B*, *28*(6), 3590–3592.

Tutuc, E., Shayegan, M., & Huse, D. A. (2004). Counterflow measurements in strongly correlated GaAs hole bilayers: Evidence for electron-hole pairing. *Physical Review Letters*, *93*(3), 036802.

Vinattieri, A., Shah, J., Damen, T. C., Kim, D. S., Pfeiffer, L. N., Maialle, M. Z., & Sham, L. J. (1994). Exciton dynamics in GaAs quantum-wells under resonant excitation. *Physical Review B*, *50*(15), 10868–10879.

Vörös, Z., Balili, R., Snoke, D. W., Pfeiffer, L., & West, K. (2005). Long-distance diffusion of excitons in double quantum well structures. *Physical Review Letters*, *94*(22), 226401.

Wakita, K. (1998). *Semiconductor Optical Modulators*. Norwell, MA: Kluwer Academic Publishers.

Winbow, A. G., Butov, L. V., & Gossard, A. C. (2008). Photon storage with subnanosecond readout rise time in coupled quantum wells. *Journal of Applied Physics*, *104*, 063515.

Winbow, A. G., Hammack, A. T., Butov, L. V., & Gossard, A. C. (2007). Photon storage with nanosecond switching in coupled quantum well nanostructures. *Nano Letters*, *7*(5), 1349–1351.

Winbow, A. G., Leonard, J. R., Remeika, M., Kuznetsova, Y., High, A., Hammack, A. T., Butov, L. V., Wilkes, J., Guenther, A. A., Ivanov, A. L., Hanson, M., & Gossard, A. (2011). Electrostatic conveyer for excitons. *Physical Review Letters*, *106*, 196806.

Wood, T. H., Burrus, C. A., Miller, D. A. B., Chemla, D. S., Damen, T. C., Gossard, A. C., & Wiegmann, W. (1983). High-speed optical modulation with

GaAs/GaAIAs quantum wells in a p-i-n diode structure. *Applied Physics Letters*, *44*, 16–18.

Wu, C. & Shem, I. (2008). Exciton condensation with spontaneous time-reversal symmetry breaking. *arXiv:0809.3532v3*.

Xu, Q. F., Schmidt, B., Pradhan, S., & Lipson, M. (2005). Micrometre-scale silicon electro-optic modulator. *Nature*, *435*(7040), 325–327.

Yang, S., Butov, L. V., Levitov, L. S., Simons, B. D., & Gossard, A. C. (2010). Exciton front propagation in photoexcited GaAs quantum wells. *Physical Review B*, *81*(11), 115320.

Yang, S., Hammack, A. T., Fogler, M. M., Butov, L. V., & Gossard, A. C. (2006). Coherence length of cold exciton gases in coupled quantum wells. *Physical Review Letters*, *97*(18), 187402.

Yang, S., Mintsev, A., Hammack, A., Butov, L. V., & Gossard, A. C. (2007). Repulsive interaction in the macroscopically ordered exciton state in GaAs/$Al_xGa_{1-x}As$ coupled quantum well structures. *Physical Review B*, *75*, 033311.

Yoshioka, D. & Macdonald, A. H. (1990). Double quantum-well electron-hole systems in strong magnetic-fields. *Journal of the Physical Society of Japan*, *59*(12), 4211–4214.

Yoshioka, K., Chae, E., & Kuwata-Gonokami, M. (2011). Transition to a Bose-Einstein condensate and relaxation explosion of excitons at sub-kelvin temperatures. *Nature Communications*, *2*, 328.

Yu, X. Z., Onose, Y., Kanazawa, N., Park, J. H., Han, J. H., Matsui, Y., Nagaosa, N., & Tokura, Y. (2010). Real-space observation of a two-dimensional skyrmion crystal. *Nature*, *465*(7300), 901–904.

Zhu, X. J., Littlewood, P. B., Hybertson, M. S., & Rice, T. M. (1995). Exciton condensate in semiconductor quantum-well structures. *Physical Review Letters*, *74*(9), 1633–1636.

Zimmermann, S., Govorov, A. O., Hansen, W., Kotthaus, J. P., Bichler, M., & Wegscheider, W. (1997). Lateral superlattices as voltage-controlled traps for excitons. *Physical Review B*, *56*(20), 13414–13421.

Zrenner, A. (1992). *Festkörperprobleme/Advances in Solid State Physics.*, *32*, 61.

Zrenner, A., Butov, L. V., Hagn, M., Abstreiter, G., Bohm, G., & Weimann, G. (1994). Quantum dots formed by interface fluctuations in AlAs/GaAs coupled-quantum-well structures. *Physical Review Letters*, *72*(21), 3382–3385.